Wake Characterization of Small Horizontal-Axis Wind Turbines in Single and Double Rotor Systems

A Thesis
Submitted in Partial Fulfilment of the Requirements for
the Award of the Degree of

Doctor of Philosophy

by

Ravi Kumar
Registration No. 186103026

Department of Mechanical Engineering
Indian Institute of Technology Guwahati
Guwahati – 781039, Assam, India
December 2025

Declaration

I hereby certify that the work compiled in this thesis entitled 'Wake Characterization of Small Horizontal-Axis Wind Turbines in Single and Double Rotor Systems' is the outcome of my research work under the guidance of Professor Niranjan Sahoo and Professor Ujjwal K. Saha in the Department of Mechanical Engineering, Indian Institute of Technology Guwahati, India.

Any part of this work has not earlier been submitted for the award of any degree, diploma, associate-ship, fellowship or its equivalent to any University or Institution.

(Ravi Kumar)
Registration No. 186103026
Department of Mechanical Engineering
Indian Institute of Technology Guwahati

Date: December 19, 2025

Certificate

It is certified that the work contained in the thesis entitled 'Wake Characterization of Small Horizontal-Axis Wind Turbines in Single and Double Rotor Systems' submitted by Mr. Ravi Kumar to the Indian Institute of Technology Guwahati for the award of the degree of Doctor of Philosophy has been carried out under my supervision in the Department of Mechanical Engineering, Indian Institute of Technology Guwahati. This work has not been submitted elsewhere for the award of any other degree or diploma.

(Niranjan Sahoo)
Professor
Department of Mechanical Engineering
Indian Institute of Technology Guwahati

Date: December 19, 2025

(Ujjwal K. Saha)
Professor
Department of Mechanical Engineering
Indian Institute of Technology Guwahati

Date: December 19, 2025

Acknowledgement

First and foremost, I express my heartfelt gratitude and deepest respect to my supervisors, Professor Niranjan Sahoo and Professor Ujjwal K. Saha, Department of Mechanical Engineering, IIT Guwahati, for their unwavering guidance, continuous support, and sincere cooperation throughout the course of this research work. Their profound knowledge, research acumen, and inspiring vision have been a constant source of motivation and encouragement. This work would not have been possible without their expert supervision and consistent mentorship.

I extend my sincere thanks to the members of my Doctoral Committee – Professor Vinayak Kulkarni**,** Professor Sukhomay Pal**,** Professor Animes Kumar Golder**,** and Professor Dipankar Narayan Basu – for their valuable suggestions, constructive feedback, and ongoing encouragement that helped shape the direction of my research.

I am also thankful to Professor Santosh K. Diwedy**,** Professor S. Senthilvelan**,** Professor K. S. R. Krishna Murthy (former Heads of Department), and Professor S. M. Hazarika (present Head of Department, Mechanical Engineering) for providing the necessary facilities and academic environment essential for the completion of this work. My sincere appreciation goes to all faculty members, technical and non-technical staff, and fellow research scholars of the Department of Mechanical Engineering, IIT Guwahati, for their cooperation and assistance throughout my research journey.

I am deeply indebted to my family members for their constant support, unconditional love, and encouragement throughout the ups and downs of my PhD journey. Their emotional strength and patience made this endeavour possible. My backbone, Barbi Sarma—your love and faith in me have been my greatest strength through every challenge and victory. Your presence made this journey lighter and more meaningful.

I would like to express my special thanks to Dr. Ojing Siram for his continual motivation and generous support during various stages of the project. I am also grateful to my PhD colleagues Dr. Man Mohan**,** Mr. Subhash Pratap, and Mr. Ankan Hazara who supported, encouraged, and stood by me throughout my PhD journey.

My sincere thanks to my lab mates – Dr. Anand Verma**,** Ms. Kabita Naik**,** Dr. Bastav Borah**,** Dr. Umang Rathod**,** and Mr. Rishi Purohit – for their cooperation, insightful discussions, and the friendly environment they created in the laboratory.

Finally, I gratefully acknowledge the Ministry of Human Resource Development (MHRD), Government of India**,** for providing the financial support through their scholarship scheme, which enabled me to pursue my academic goals without constraint.

Ravi Kumar

December 19, 2025

Abstract

Wind energy is now a vital part of the renewable energy portfolio due to the growing need for sustainable energy on a global scale. Small wind turbines and multi-rotor systems are becoming competitive alternatives for dispersed generation and enhanced scalability, even though large wind turbines still account for the majority of utility-scale installations. Nevertheless, little is known about the aerodynamic interactions that occur in the wake of these arrangements, especially under the low Reynolds number operating conditions and closer rotor spacing, which are characteristics of small-scale and multi-rotor systems. This thesis uses theoretical, and experimental methods to investigate the wake behaviour of small horizontal-axis wind turbines in single- and double-rotor configurations, with particular emphasis on the role of local and global Reynolds number scaling in wake development and recovery.

Establishing the aerodynamic underpinnings of wind turbine operation and examining current wake modelling methods focusing on their shortcomings in forecasting intricate wake interactions are the first steps in the effort. In addition to highlighting critical research gaps in wake structure and recovery analysis, a thorough literature review places the performance characteristics of small wind turbines and multi-rotor systems in context, including limitations of existing models when applied to low Reynolds number and multi-rotor configurations.

Hot-wire anemometry with quantified measurement uncertainty was utilised to study wake behaviour in a low-speed open-circuit wind tunnel experimentally. To capture specific wake characteristics, scaled models of small horizontal axis wind turbines were tested in single- and double-rotor configurations with different rotors tip spacings ($T_S = 0.5R$ and $1.0R$). Reynolds numbers were defined locally along the blade span and globally based on rotor diameter to ensure aerodynamic relevance and consistency with prior wake studies. The study demonstrated the effects of tip spacing on recovery initiation, wake symmetry, and velocity deficit in both horizontal and vertical planes. Significantly, broader separation permitted better recovery and less turbulence, whereas closer spacing increased wake interaction and changed flow structure.

Low tip speed ratio conditions, common in small horizontal axis wind turbines, were used to examine the wake flow further. The results show how tip speed ratio and tip spacing combine to affect downstream velocity fields, revealing wake trends that are governed primarily by normalized flow quantities and persist beyond the near wake, despite low operating Reynolds numbers. These findings recommend design changes for better aerodynamic performance in small turbine arrays.

Significant contributions include comparing single- and double-rotor wake dynamics, experimental confirmation of wake recovery tendencies, and improved understanding of three-dimensional wake evolution. By linking local aerodynamic behaviour to integrated wake metrics and recovery trends, the findings provide physically grounded insights applicable to small-scale and multi-rotor wind energy systems. The thesis concludes with suggestions for enhanced numerical modelling and advanced experimental diagnostics to further resolve unsteady wake interactions and their implications for energy capture efficiency.

Contents

Nomenclature

Latin Symbols

a	Axial Induction Factor
a'	Tangential Induction Factor
c	Chord Length (m)
C_r	Sectional chord length (m)
C_L	Lift coefficient (-)
C_D	Drag coefficient (-)
C_P	Power coefficient (-)
$C_{P_{\max}}$	Maximum power coefficient (-)
C_T	Thrust coefficient (-)
D	Rotor diameter (m)
F_D	Drag force (N)
F_L	Lift force (N)
F_T	Tangential force (N)
F_N	Normal force (N)
g	Acceleration due to gravity (m/s^2)
h_r	Sectional tapper height (m)
H_b	Hub height (m)
N_B	Number of blades (-)
$P_{\max}$	Maximum power output (W)
r	Radial distance from rotor centre (m)
R	Rotor radius (m)
Re	Reynolds number (-)
T_a	Ambient turbulence intensity (-)
T_S	Tip spacing (m)
U_d	Velocity deficit (m/s)

U_w	Wind velocity in wake behind turbine (m/s)
U_∞	Inlet velocity (m/s)
U_{rel}	Relative velocity (m/s)
$\overline{U_\infty}$	Average of inlet velocity (m/s)
U_{cw}	Wind velocity at wake centre (m/s)
U^*	Normalised velocity deficit (-)

Greek Symbols

α	Angle of attack (°)
β	Pitch angle (°)
γ	Yaw angle (°)
η_{WF}	Wind farm efficiency (-)
θ_p	Section pitch angle (°)
θ_T	Section twist angle (°)
κ	Turbulence kinetic energy (J/kg)
λ	Tip speed ratio (-)
μ	Dynamic viscosity (N-s/m^2)
ν	Kinematic viscosity of fluid (m^2/s)
ρ	Fluid density (kg/m^3)
σ	Solidity of turbine blade (-)
σ_r	Sectional solidity (-)
ϕ	Angle of relative wind (°)
τ	Normalised time step (-)
ψ	Taper angle (°)
ω	Angular velocity (rad/s)

Abbreviations

ABL	Atmospheric Boundary Layer
AIVD	Area-Integrated Velocity Deficit
BEMT	Blade Element Momentum Theory
CAGR	Compound Annual Growth Rate

CTHWA	Constant Temp. Hot-Wire Anemometer
DAQ	Data Acquisition
FDM	Fused Deposition Modeling
HAWT	Horizontal-Axis Wind Turbine
HWA	Hot-Wire Anemometry
LWT	Large Wind Turbine
MGA	Micro-Genetic Algorithm
MRS	Multi-Rotor System
NBL	Neutral Boundary Layer
NITE	National Institute of Wind Energy
PIV	Particle Image Velocimetry
RANS	Reynolds-Averaged Navier-Stokes
RE	Renewable Energy
RSM	Reynolds Stress Model
RTS	Rotary Torque Sensor
SD	Standard Deviation
SLT	Straight and Linearly Tapered
SST	Shear Stress Transport
SWT	Small Wind Turbine
TI	Turbulence Intensity
TSR	Tip Speed Ratio
VAWT	Vertical-Axis Wind Turbine
WPD	Wind Power Density

Superscripts

*	Normalised form
–	Time average

Subscripts

∞	Free stream
rms	Root mean square

List of Figures

List of Tables

CHAPTER 1

INTRODUCTION

1.1 Motivation

Growing awareness of climate change and the need to cut carbon emissions have made expanding renewable energy sources essential. Specifically, wind energy provides a workable alternative, but only well-designed wind farms that reduce energy losses from wake effects can fully utilize wind energy's potential. Global primary energy output reached over 170,000 TWh by the end of 2023, which is roughly 14.6 gigatons of oil equivalent (GToe) (IEA, 2024; IRENA & ILO, 2024). Oil, coal, and natural gas account for over 81% of the overall supply, demonstrating how strongly this output still depends on fossil fuels (IEA, 2024; Ritchie et al. 2023). In 2024, approximately 115 GW of new wind capacity was added, showing a slight increase from 2023 and bringing the total installed capacity to around 1,150 GW with a compounded annual growth rate (CAGR) of about 10% (IEA, 2024). This marks a substantial increase from earlier levels and reflects the sustained momentum in the wind energy sector. From 2000 to 2023, the CAGR of global wind capacity has averaged around 13.6%, with particularly rapid growth in the past decade as shown in Fig 1.1.

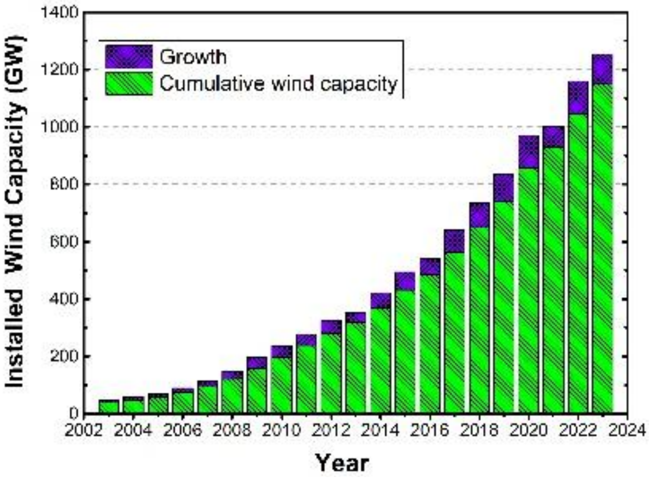

Fig. 1.1 Progress in global wind energy installation (IEA, 2024),(IRENA & ILO, 2024)

Wind power is primarily generated through onshore (inland) and offshore (sea/coastal regions) wind farms, which are collections of turbines designed for efficient energy production. While onshore wind farms face challenges such as land use, non-uniform wind patterns, noise pollution, complex terrain, and logistical issues, offshore wind farms can generate more energy due to steadier and more consistent wind conditions. Studies on various offshore projects indicate that they typically require higher initial investments than onshore wind generation projects. In other hand, decentralised energy generation is made possible by small wind turbines (SWTs), which makes them especially useful in rural or isolated locations with little to no grid access. They encourage rural development and energy fairness by supplying small companies, agricultural activities, and off-grid homes with dependable electricity. Regarding technology, SWT research has sparked advancements in low Reynolds number (*Re*) aerodynamics, small blade designs, noise reduction techniques, and sophisticated control systems (Malhotra et al, 2023; Hau 2013; Wood 2011).

India has made significant strides in embracing renewable energy in response to global climate goals and domestic energy security concerns. According to the Renewable Energy Statistics (RES, 2024) report, India's total installed power capacity surpassed 417 GW by 2023, of which ~125 GW (around 30%) now comes from renewable energy sources. India's total installed wind capacity increased steadily from approximately 26 GW in 2015–16 to 44.7 GW by 2021–22, reflecting a moderate but consistent expansion in the sector. Annual additions ranged between 1.5 GW to 3.3 GW, with the highest growth occurring in 2016–17. The cumulative growth trend indicates that while wind energy remains a key contributor to India's renewable mix accounting for nearly 25% of total renewable capacity the pace of new installations has slowed compared to the rapid rise in solar energy as shown in Fig. 1.2.

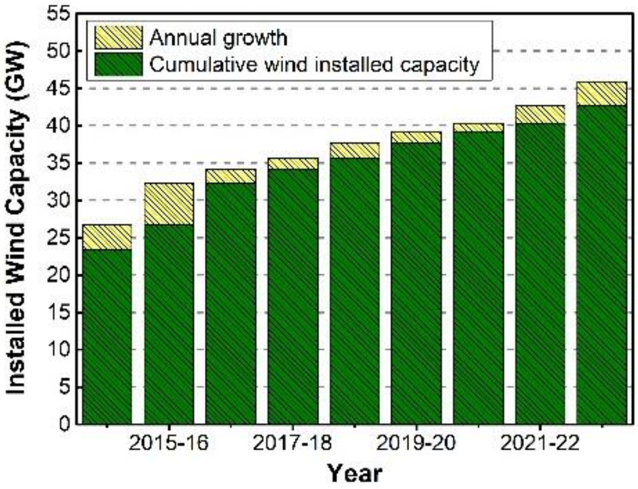

Fig. 1.2 Wind energy with annual growth in India (RES, 2024)

In light of above, national initiatives aim to enhance the assessment of wind resources. Over 850 meteorological masts have been installed by the National Institute of Wind Energy (NIWE) in several states, gathering wind data at heights of up to 120 meters, which is currently the norm for assessing contemporary utility-scale turbines (NIWE, 2024; MNRE, 2023). These initiatives offer a strong basis for further advancement.

1.2 Wind Energy Harvesters

Wind turbine is genuinely remarkable machines that effectively capture the power of the wind and transform it into electrical energy that can be utilized in various settings such as homes, businesses, and industries. Numerous essential variables, such as wind speed, air density, rotor diameter, blade design, and turbine orientation, affect how efficiently wind energy is harvested. Wind turbines are usually placed in areas with high average wind speeds and little turbulence to optimise energy extraction. Modern wind turbines include pitch control and yaw mechanisms to maximise the blade angle and alignment with the prevailing wind and improve energy extraction.

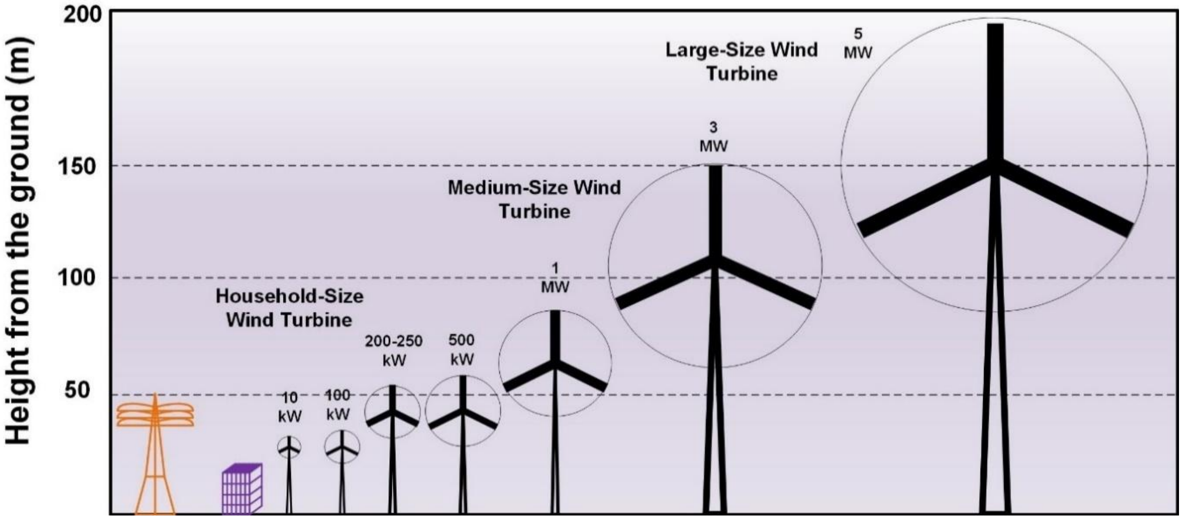

Fig. 1.3 Classification of horizontal wind turbines based on rotor diameter (Tummala et al., 2016)

Wind turbines are broadly categorized into two types based on the axis of rotation relative to the direction of the wind and such as horizontal-axis wind turbines (HAWT) and vertical-axis wind turbines (VAWT) (Burton et al., 2007). These types fall into the categories of lift-based and drag-based systems respectively. The scale and configuration of wind harvesting systems vary. Commonly seen in wind farms, large HAWTs are built for grid integration and high-power output. On the other hand, localised power generation is accomplished by SWTs. Rotor size, hub heights, capacity, reliability, efficiency, and location further differentiate these turbines. An example of how turbines are classified according to hub height, rotor diameter, and capacity is depicted in Fig. 1.3, with additional information provided in Table 1.1.

Table 1.1 Classification of wind turbines on the basis of size, capacity, and application

Turbine category	Typical Models	Rotor Dia. (m)	Power output (kW)	Typical wind condition	Primary Application
Micro Scale wind turbines	NE-100 S, NE-200S, NE-300S, μF500m, Superwind350, Rutland 913 etc.	0.50 – 1.25	0.004 – 0.25	Very Low	Low power application
Mini Scale wind turbines	Bornay 600, TAOS 600, AC 240, Air-x marine etc.	1.25 – 3	0.25 – 1.4	Low	Building Integrated rooftop
Domestic Scale wind turbines	Savonius Type, Darrieus Type, twisted Savonius, small HAWT, QR5 Gorlov type VAWT etc.	3 – 10	1.4 – 16	Moderate	Hybrid System
Small wind turbines	MG4520, Small HAWT, American wind energy association (AWEA), etc.	10 - 20	25 - 100	Good	Residential Power
Medium Commercial turbines	Nibe A and Nibe BDK, Mod-OA US, Tvind DK 54 etc.	20 - 50	100 - 1000	High	Mini wind farm
Large commercial turbines	Vestas V164-8 MW, Siemen SWT-8.0-154, Siemens SWT-2.3-101 Nordex N80, N90, N100, V120-2.0 MW, etc.	≥ 50	1000 – 8000	Very high	Large scale production, Offshore Wind farm, Onshore windfarm

1.3 Small Wind Turbines

Small wind turbines are crucial for decentralized energy production with rotor diameters less than 10 m and capacities typically below 100 kW, SWTs provide an economically viable solution for rural electrification, off-grid applications, and augmenting existing power supplies. SWTs are subdivided into small HAWTs and small VAWTs. Unlike large wind turbines, SWTs function in the low-*Re* order of (10^4-10^5) regime (Chamorro et al., 2011; Xiong et al., 2022). These SWTs are also assembled on a single tower to make multi-rotor system (MRS) which is new innovative idea in wind energy technology as a promising strategy to enhance power density within a given land footprint. The investigation primarily concentrates on small HAWTs because they generally perform better than VAWTs (Tummala et al., 2016). Within the small HAWT category, turbines are classified into micro-scale, mini-scale, and small-scale. Conversely, small VAWTs are categorized into designs featuring Savonius, Darrieus, or hybrid rotors. Despite VAWTs typically having a lower power coefficient (C_p) (Jain and Saha, 2019; Treuren, 2015), their efficiency can be increased through the introduction of specific pitch control mechanisms, multi-rotor systems, and various augmentation techniques (Neagoe et al., 2020; Zhao et al., 2019; Sun et al., 2012). Further exploration of SWTs is available in the section literature review on small wind turbines.

China and the United States emerged as the predominant markets (Sheridan et al., 2024), highlighting the vast potential SWTs hold for the future. Economically, SWTs present a more cost-effective solution than large wind turbines (LWT) in terms of installation, operation, maintenance, and repair costs. This affordability makes them viable for standalone and off-grid renewable energy setups. Operating typically at low *Re* and low tip speed ratios (λ), SWTs face design, development, and testing challenges, primarily due to inadequate detailed aerodynamic insights. An integrated SWT setup might involve a configuration of multiple turbines akin to a small wind farm or a singular system equipped with several rotors (Liu et al., 2019). The study on large multi-rotor system (MRS) by van der Laan et al. (2019) demonstrated that despite the complex structure, the system produces favourable output compared to single turbines with similar configuration depicted in Fig. 1.4.

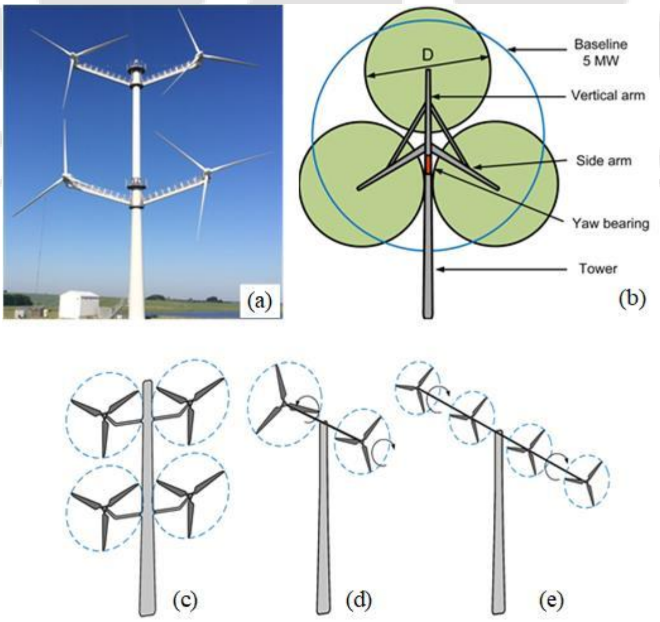

Fig. 1.4. Illustration of MRS (a) Large MRS Vestas turbine (van der Laan et al., 2019) under a Creative Commons Attribution (CC BY) license, (b) MRS's geometry with respect to baseline rotor, and (c-e) the arrangement of MRS in different configuration

Potential array-level energy increases under favourable wake-interaction conditions have been reported in earlier experimental and numerical studies, ranging from roughly 10% to 25%, depending on rotor spacing, alignment, and operational λ (Feltes et al., 2011). Nevertheless, these improvements are accompanied by intricate wake-interaction processes that may also result in localised wake deficiencies, increased turbulence, and unstable loading (Houck, 2021). However, the laminar-to-turbulent transition, early flow separation, improved tip-vortex coherence, and low ambient turbulence levels have a significant impact on wake formation in the low *Re* SWT domain (Lignarolo et al., 2015: Li et al., 2022: Villeneuve and Dumas). Wake recovery rates, deficit magnitudes, and lateral spreading rates thus frequently differ considerably from traditional expectations.

Scaling limitations between large and small turbines present another significant difficulty. At low *Re*, decreased air turbulence and limited wind-tunnel blockage collectively modify wake diffusion, vortex breakup, and momentum entrainment mechanisms at small scales (Lee and Lee, 2020). More profound near-wake deficits, wake recovery that is either expedited or delayed depending on operating conditions, and essentially distinct turbulence-producing paths result from this (Wei et al., 2024). As a result, direct application of large-turbine wake information to SWT systems may lead to considerable forecast errors in fatigue evaluation and performance estimation.

Improving their efficiency and integrating them into the current energy framework requires understanding their wake behaviour. MRS offers a viable alternative to conventional designs, but their wake interactions are not yet fully understood. Investigating these relationships is necessary to optimize turbine array design and extract more energy. Analytical models provide theoretical insights into underlying phenomena, while wind tunnel studies offer critical empirical data on wind turbine wake behaviour. Wind farm designers, developers, and operators can apply the research's conclusions, which advance understanding of wind turbine wake characterization. This knowledge can help create more affordable and effective wind energy systems, accelerating the shift to renewable energy sources.

1.4 Present Objective and Road Map

This study is centred around analysing the wake effects produced by a small HAWT alongside single- and double-rotor configurations under conditions of low *Re* and low λ. A series of steps involving the design, development, and testing were proposed to pursue this objective. The primary aims of this research are outlined below, with a detailed research path depicted in Fig. 1.5.

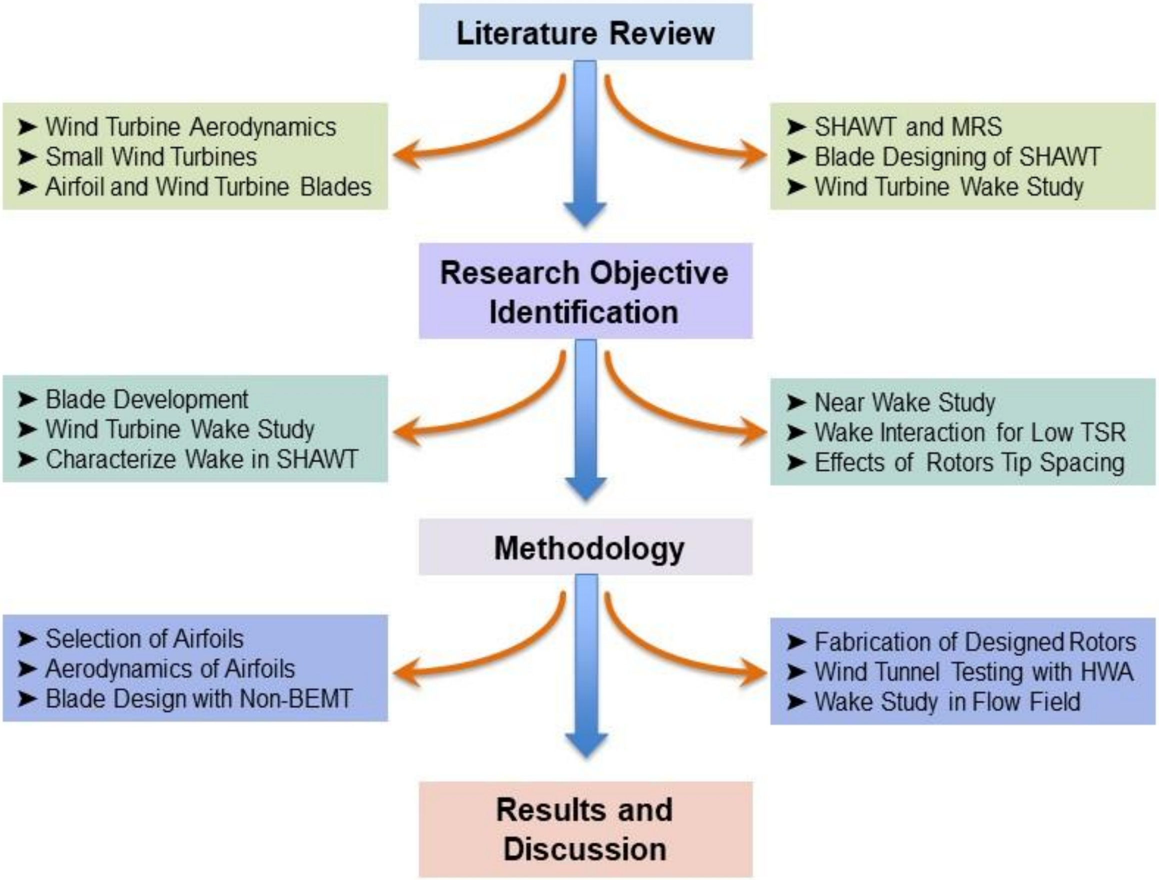

Fig. 1.5 Illustration of research objectives and road map

The study starts with a thorough literature analysis covering fundamental ideas, including wind turbine aerodynamics, blade profiles, and SWTs operating characteristics. Additionally, it examines the theoretical and computational facets of wind turbine wake modelling and the design issues for small HAWTs. Following this review, identify research objectives corresponding to the knowledge gaps in wake behaviour and aerodynamic efficiency in configurations with one or more rotors. As a result, several airfoils are assessed for aerodynamic performance in the following stage of airfoil selection and blade design. The research then proceeds to experimental modelling, which entails using fused deposition modelling (FDM) 3D printing technology to fabricate scaled turbine rotors after the designs are complete. Wake investigations, velocity field visualisation, and flow diagnostics are used to evaluate the performance of these physical models in a wind tunnel setting with help of hot-wire anemometry (HWA). A comprehensive examination of wake interactions, λ effects, and rotor tip spacing implications is made possible by the data obtained from experimental research.

1.5 Organisation of Thesis

This thesis covers the aerodynamic characterisation of small HAWTs in single and multi-rotor configurations in seven chapters. Chapter 1 presents the national and international renewable energy background, highlights the potential of MRS and small HAWTs for decentralised applications, and lists the study's primary goals. Following a thorough literature analysis identifying current research needs, Chapter 2 provides the theoretical background by going over wind turbine aerodynamics, blade profiles, and literature review for SWTs and MRS. The design and construction of SG6043-based small HAWT models using SolidWorks and FDM 3D printing, as well as the wind tunnel setup with HWA for wake analysis, are all covered in detail in Chapter 3. Chapter 4 examines near-wake behaviour for single and double-rotor systems, emphasising how rotor interaction affects wake formation and flow asymmetry. Chapter 5 discusses how wake interaction, turbulence development, and velocity deficits in both horizontal and vertical planes are affected by low tip-speed ratios and rotor spacing (T_S = $0.5R$ and $1.0R$). In-depth wake recovery analysis is presented in Chapter 6, which also compares the aerodynamic performance of MRS with conventional topologies and shows how rotor geometry, spacing, and input velocity impact the downstream flow field. Chapter 7 highlights the study's key conclusions, contributions, consequences, and potential future research areas.

CHAPTER 2

BACKGROUND THEORY AND LITERATURES

2.1 Wind Turbine Aerodynamics

Wind turbines generate power from the kinetic energy of the wind. The most popular kind of wind turbine, HAWTs, rotates a generator by lift produced by airflow across their blades and can pivot for maximum effectiveness. VAWTs use drag forces to capture wind from any direction with a vertical rotor shaft. They are appropriate for residential or urban settings with erratic winds due to their straightforward design, eliminating the need for an orientation mechanism. In wind turbine aerodynamics, there is a principle called the Betz Limit. It is measured by the power coefficient (C_P), which is capped at 0.593. This threshold is generally referred to as the Betz limit, and it is caused by the inherent losses in the system (Okulov and van Kuik, 2012). Turbine inefficiencies could arise from several areas, including the tip and hub regions, as well as the transmission system, among others (Zhong et al., 2020). It is essential for wind turbine blade developers to consider these parameters.

The analysis of aerodynamic loads mainly relies on the blade element momentum theory (BEMT) by Ledoux et al. (2020). This theory considers the free stream wind velocity (U_∞) and the geometry of the aerodynamic profiles used in the blade. These profiles are defined on the basis of unique aerodynamic lift (C_L)and drag (C_D) coefficients. The relationship between lift and drag is a crucial component in the design of wind turbines. Achieving the necessary torque to initiate turbine rotation and generate electricity requires a careful equilibrium between these two forces (Jaszczur et al., 2024; McTavish et al., 2013). The efficiency and functionality of wind turbines are significantly affected by the profiles and shapes of their blades. The key to design turbine blades lies in their cross-sectional shapes, known as airfoils. These airfoils are pivotal in creating lift, drag, and torque as they navigate through air, enhancing the aerodynamics and structural integrity of the turbine blades. Blades may be designed with curves, twists, or variable camber surfaces to increase energy capture. This study focuses on the HAWT design. Therefore, the aerodynamic discussions in this chapter are primarily centred around HAWT.

2.1.1 Lift and Drag Forces on Wind Turbine Blades

The force component that impacts the surface perpendicularly to the direction of the relative wind velocity is termed lift force (F_L), and the force component that aligns parallel to the direction of the relative wind velocity is known as drag force (F_D), as illustrated in the provided Fig. 2.1. The magnitude of lift and drag forces is affected by various factors, including the size and shape of the lifting surface, its orientation about the flow. In contrast to static airfoils that depend on the angle of attack (α) at a specific *Re* to determine their aerodynamic performance, rotating rotor blades like those found in wind turbines obtain their aerodynamic and performance characters from the relative angle of attack (Albi et al., 2017). This angle forms between the relative velocity (U_{rel}) experienced by a rotating blade section and its chord line (Manwell et al., 2009). The wind turbine blade section encounters fundamental aerodynamic forces in a typical scenario with uniform inflow, as illustrated in Fig. 2.1.

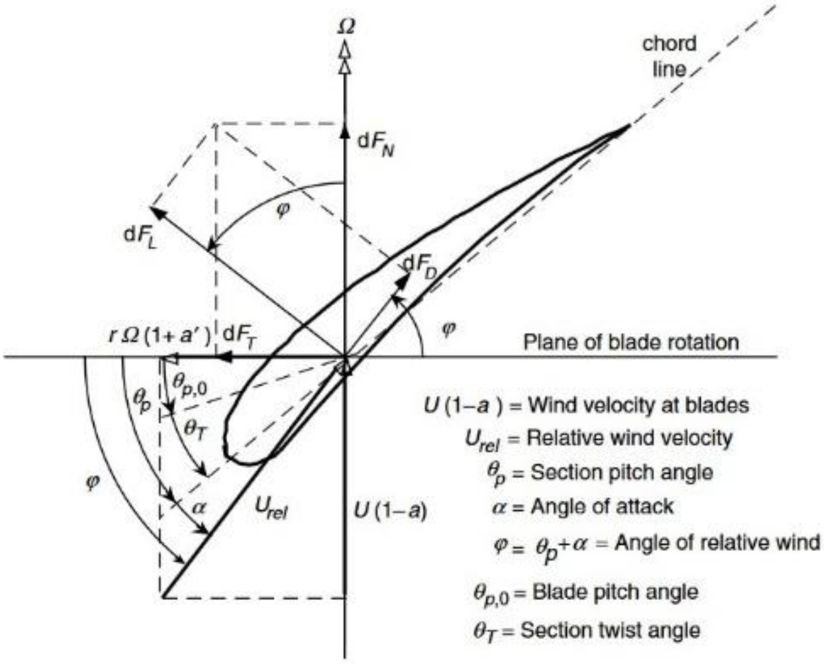

Fig. 2.1 Schematic diagram of blade aerodynamics analysis (Manwell et al., 2009)

Wind turbine performance is commonly characterized by the λ and *Re*, as indicated in Eq. (2.1). The aerodynamic forces influencing the airfoil are detailed in Eqs. (2.2) to (2.7), while the velocity triangle illustrates the local velocity distribution along the blade section (Manwell et al., 2009). These force components and the velocity diagram are critical in designing HAWT blades using BEMT. This method enables designers to determine the axial (*a*) and tangential ($a^{'}$) induction factors, which are crucial for defining significant design parameters like blade twist, pitch, and various aerodynamic enhancements throughout the blade span (Manwell et al., 2009). The angle of attack greatly relies on the pitch angle which is the angle between the axial wind velocity and the tangential wind velocity expressed by Jureczko et al., (2005).

$$\lambda = \frac{R\omega}{U_\infty} = \frac{2\pi NR/60}{U_\infty}\ ;\ \text{and,}\ \ \mathrm{Re} = \frac{\rho U c}{\mu} \tag{2.1}$$

$$U_{rel} = \frac{\lambda(1+a^{'})}{U_\infty \cos\phi} = \sqrt{U^2 + (r\omega)^2}\ ;\ \text{and,}\ \ \tan\phi = \frac{(1-a)}{(1-a^{'})\lambda} \tag{2.2}$$

$$C_L = \frac{F_L}{\frac{1}{2}\rho U_{rel}^2 A_p}\ ;\ \text{and,}\ \ C_D = \frac{F_D}{\frac{1}{2}\rho U_{rel}^2 A_p} \tag{2.3}$$

$$F_L = \frac{1}{2}\rho U_{rel}^2 c C_L \tag{2.4}$$

$$F_D = \frac{1}{2}\rho U_{rel}^2 c C_D \tag{2.5}$$

$$F_N = F_L \cos\phi + F_D \sin\phi \tag{2.6}$$

$$F_T = F_L \sin\phi - F_D \cos\phi \tag{2.7}$$

Lift force (F_L), drag force (F_D), thrust force (F_N), and tangential force (F_T) are the aerodynamic forces operating on a revolving blade in relation to U_{rel} (Fig. 2.1). Streamwise velocity (U_∞) and angular velocity (ω) combine to form the U_{rel}.

Recognizing that the airflow over any wing with a finite span is fundamentally three-dimensional. This complexity is increased by trailing vortices behind the wing, as depicted in the Fig. 2.2. These vortices generate a downwash over the wing, which alters the local angle of attack across its span, affecting its lift and overall aerodynamic performance. The flow may be considered approximately two-dimensional at sections far from the wingtip vortices.

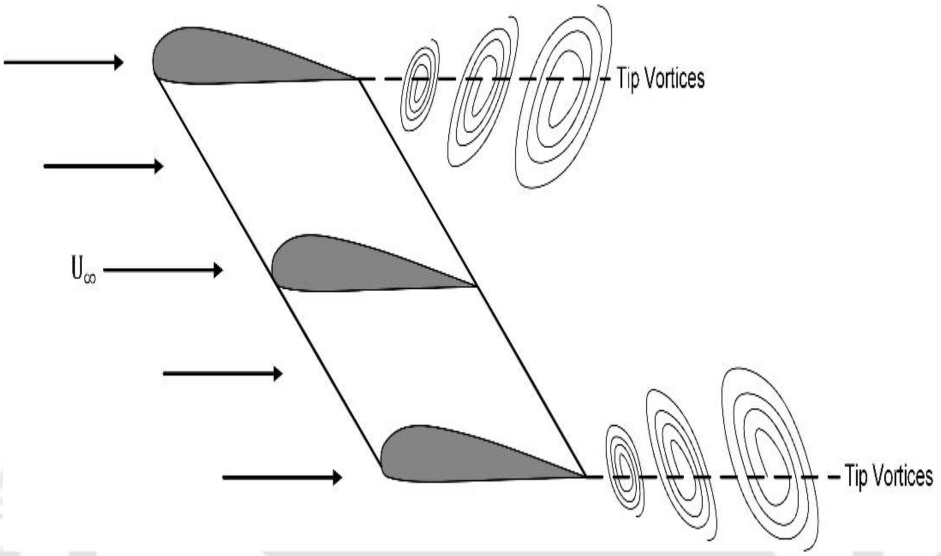

Fig. 2.2 Generation trailing vortices behind the wing

2.1.2 Principal Observations on Blade Profiles

The concept of "blade profile" pertains to the unique cross-section of a blade, which is essential in defining its efficiency. Various crucial elements affect the design of blade profiles, such as the angle of attack, contour (either cambered or flat), and aspect ratios, each contributing distinctively to a blade's ability to transform. Tapered profiles narrow from base to tip, improving efficiency by lowering resistance. The angle at which the blade meets the oncoming flow, known as the angle of attack, is pivotal for its performance. This angle, measured between the blade's chord line and the fluid's direction, dramatically affects the lift and drag forces, influencing the blade's efficiency and stability. Engineers meticulously modify this angle to align with design goals and performance objectives.

Designing a rotor begins by carefully selecting the airfoil and rotor characteristics. This involves assuming wake rotation to determine the ideal blade shape, considering axial and tangential induction factors. These conditions include aligning the angle of attack with the peak C_l / C_d ratio, as demonstrated in studies by Dehouck et al., (2018) and Song and Luitz, (2014).

2.2 Literature Review on Small Wind Turbines

The market has increasingly recognized the value of SWTs, including both horizontal and vertical-axis models, as off-grid, standalone, and decentralized sources of supplemental energy. These turbines mainly function at low *Re* and low λ scenarios. In these situations, designing, developing, and testing of SWTs have turned into a challenging endeavour, primarily because of the insufficient aerodynamic understanding of SWTs. This section of the research focuses on examining the essential elements of SWTs, including the criteria for choosing airfoils, the process of designing blades, and the enhancement of aerodynamics through the use of passive flow control. Additionally, the article identifies various categories of airfoils that are suitable for use in SWTs design. The article discusses airfoils that primarily function within a range *Re* = 30,000 to 300,000 and λ from 0.5 to 6.

Previous research (Jain and Saha, 2019; Nguyen and Metzger, 2017; Tummala et al., 2016; McTavish et al., 2013), the SWTs are accessible in two primary configurations: HAWTs and VAWTs, as illustrated in Fig. 2.3. It's noted that small HAWTs can be categorized into three distinct sizes: small-scale, mini-scale, and micro-scale HAWTs. Alternatively, small VAWTs are classified into three types: Savonius, Darrieus, or hybrid designs. These turbines are characterized by having a rotor diameter (*D*) that does not exceed 5 meters. Compared to HAWTs, VAWTs exhibit a lower C_P (Jain and Saha, 2019; Treuren, 2015). However, their performance can be improved by using targeted pitch control mechanisms, multi-rotor systems, and other augmentation techniques (Neagoe et al., 2020; Zhao et al., 2019; Sun et al., 2012). The augmentation method adjusts the model's structure without changing the fundamental rotor/airfoil design, aiming to improve the performance of the rotor. Literature sources (Jain and Saha, 2019; Tummala et al., 2016; McTavish et al., 2013), the wind turbines range in size from large to micro (refer to Table 1.1). Wind turbines can be classified into three main categories: large wind turbines (LWTs), medium wind turbines (MWTs), and small wind turbines (SWTs), as shown in Figure 2.3.

Figure 2.4 illustrates different models of vertical-axis and horizontal-axis small wind turbines (SWTs), including the H-type Darrieus, Darrieus Turby, Gorlov, and Twisted Savonius, among others (Dilimulati et al., 2018; Casini, 2016). Additionally, these SWTs can be combined into a unified system, as depicted in Fig. 2.5, which demonstrates their potential as an effective standalone power generation solution. The commendable and impressive impact of LWTs is evident, particularly during times of increased demand for renewable energy. However, their larger size often requires significant land occupation (Tchakoua et al., 2014; Fiedler and Bukovsky, 2011; Wang and Prinn, 2010). In these situations, the potential of SWTs is highly promising.

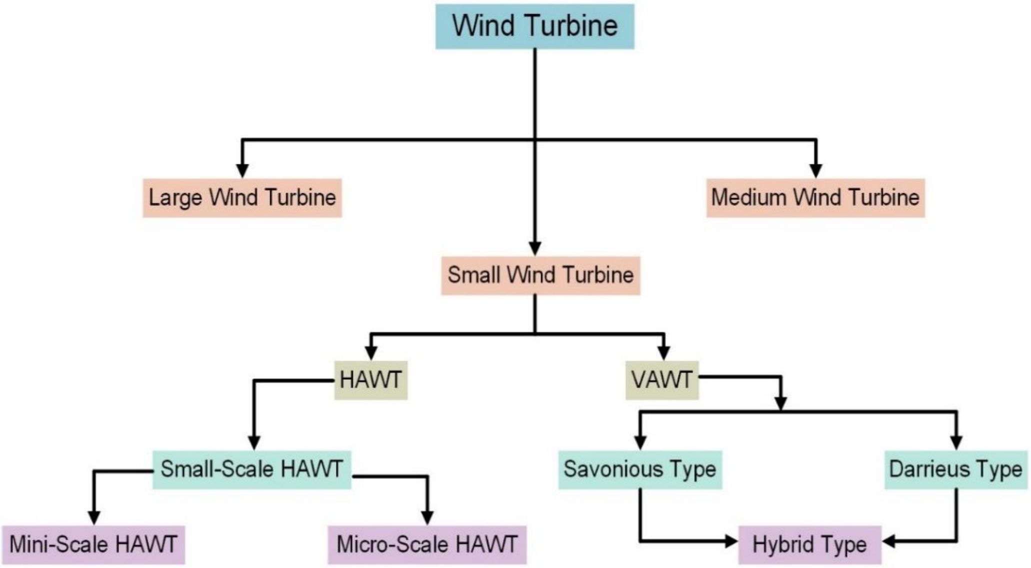

Fig. 2.3 Categories of wind turbines

Fig. 2.4 Typical vertical-axis and horizontal-axis wind turbines (Dilimulati et al., 2018; Casini, 2016)

Fig. 2.5 Cluster arrangement of small wind turbine (Liu et al. 2019; Dilimulati et al., 2018; Casini, 2016)

2.2.1 Historical Research on SWTs

The process of choosing and crafting SWTs presents significant challenges due to their requirement to function under conditions of low *Re* and λ. Preliminary research involving various airfoil types for wind turbine applications has been conducted by the National Renewable Energy Laboratory and Delft University (Karthikeyan et al., 2015; Tangler and Rooij, 2003). They have demonstrated that specific profiles may have significant implications for SWTs. Research has indicated that airfoils functioning at $Re = 5\times10^5$ are notable (Karthikeyan et al., 2015; Tangler and Rooij, 2003; Giguere and Selig, 1997), however, the investigations into turbines operating at $Re < 10^5$ remain limited. So far, numerous airfoils for wind turbine blades have been investigated, yet the research on SWT airfoils functioning at low λ remains limited.

Wind turbine blades' aerodynamic efficiency and design are primarily assessed using the BEMT. However, blades for SWT can also be designed using non-BEMT (NBEMT), which is a more straightforward approach. Additionally, optimizing the performance of these blades can be achieved through the use of genetic algorithms, Xfoil, or computational fluid dynamics (CFD) techniques. (Shen et al., 2016; Selig and McGranahan, 2004) have conducted a study on optimizing the aerodynamic shape of twisted blades in SWTs. A summary of earlier research on SWTs, considering various operational and geometric conditions, is presented in Table 2.1.

Table 2.1 Summary of literature on SWTs performance and design

Study	Method	Airfoil	N_B	R (m)	$C_{P_{max}}$	λ_{opt}	U_∞ (m/s)	BR	Notes
Freere et al. (2010)	Experimental	MG4520	3	1.05	0.22	6	13	3%	Non-BEMT. *Cp* ↓ with yaw.
Matsumiya et al., (2010)	Experimental (Field)	SD7037	3	0.9	0.36	—	9.7	—	Rated: 1 kW @12.5 m/s, 3.2 kW @20 m/s.
Lanzafame and Messina, (2010)	Experimental	NACA4415	3	0.225	0.49	4.71	7–15	—	Blade twist ↓ stall. High α ↑ resistive torque → ↓ *Cp*.
Krogstad and Lund, (2012)	Experimental + CFD	S826	3	0.45	0.448	6	—	11.8%	CFD overpredicts *Cp* by ~2%.
Wu et al., (2012)	Exp. + Simulation	NACA63415	3	0.3–0.6	0.33	—	1	—	Larger R → higher Cp. Blade count effect minor.
Refan et al., (2012)	Experimental	FX63-137 / NACA6515	3	1.1	0.277	—	1–11	21.7%, 41.8%	P_{max} = 470 W @ 9 m/s. Slight λ mismatch with BEMT.
Rocha et al., (2014)	Comp. + Field	NACA0012	3	1.5	0.14	7.25	—	—	k-ω SST model used.
Kishore and Priya; (2013)	Experimental	NACA0012	3	0.197	0.14	—	1.8–5	<10%	Ducted turbine ↑ power 1.4–1.6×.
Song and Lubitz, (2014)	Field Tests	SD7062	3	1.25	0.282	—	< 3	30%	Tested pitch +5º and +9º; *Cp* = 0.282 and 0.263 respectively.
Huang et al., (2015)	Experimental	SD80000	3	0.15	—	—	6, 8, 10	—	LEP improves *Cp* at low λ; not suitable for high wind speeds.
Shen et al., (2016)	Numerical	S809	3	0.9	~0.5	—	8	—	3D blades outperform 2D; MGA used; lift surface + free wake model.
Jackson et al., (2017)	Exp. + Numerical	NACA4424	3	0.1015	—	—	—	2.25%	Near/far wake examined in turbine arrays (2D/4D spacing); RANS w/ RST model.
Akour et al., (2018)	Exp. + Numerical	BW3, A18, SG6043	3	0.5	0.38	4.4	2.7–5.9	—	BW3 best; QBlade used; *Cp* = 0.34 (exp), 0.38 (sim).
Rocha et al., (2018)	Field Tests	NREL S809	3	1.5	0.45	8	—	—	β = 25.63° yields C_{pmax}; pitch angle impact studied.
Macphee and Beyene, (2019)	Experimental	NACA0015	3	0.571	0.256	—	2.05, 2.60, 3.15	BF: 56.15%	*Cp* ~0.256 (flexible blade) at 2.05 m/s, β = 3°; flexible has broader range.
Li et al., (2020)	Numerical	DU96W180, NACA4412	3	0.32	~0.35	6.5	—	—	Scaled 2.5 MW to 0.32 m HAWT; NACA4412 better at low *Re*.
Abdelsalam et al., (2021)	Exp. + Numerical	E216	3	0.50	0.426	5.1	5, 6, 8, 10	—	*Cp* = 0.426 @ 10 m/s; linear model *Cp* = 0.401; pitch angle effect studied.
Liu et al., (2020)	Numerical	NACA4415	3	3.5	+2%	—	—	—	Surface grooves delay laminar separation bubble → *Cp* ↑ ~2%.
Singh et al., (2012), (2013)	Experimental	AF300	2	0.63	0.30	—	4–6	—	Pitch 18º–20º improves *Cp*. Average *Cp* ↑ with speed.
Evans et al., (2018)	Experimental	SD7062	2	2.5	0.08	—	8–22	—	Aeroelastic modeling study. Power ≈ 4.7 kW @ 17 m/s.
Hirahara et al., (2005)	Experimental	NACA2404	4	0.25	0.41	2.7	4–23	3.4%	Best performance at 8–12 m/s.
Wang et al., (2008)	Experimental + CFD	Rutland 913	6	0.285	0.308	2.58	9.1, 11.25, 13.9	13.5%	Scoop tested. P_{max} = 132 W. Cutting blades ↓ *Cp* to 0.19.
Chen et al., (2012)	Experimental	NACA4415	6	0.15	0.67	—	12	4%, 10%	Flange boosts *Cp* past Betz limit.
Duquette et al., (2003)	Numerical	SG6043	—	—	—	—	—	—	*Cp* ↑ 15–25% with 5–7% ↑ in solidity (σ) at low λ.
Zhang et al., (2009)	—	S822–S823	—	—	0.43	—	5	—	Tested at 50 rpm.
Lipian et al., (2016)	Experimental	SG6040, SG6041	—	0.16	0.554	—	8–18	16%	*Cp* = 0.23 (open), 0.554 (ducted); rotor separation 0.1D–0.62D; efficiency ↑ 11–13%.

Table 2.2 Summary of literature on airfoils for SWT blade design

Airfoil	**Max. *Cl/Cd***	***Re* (x 10^5)**	***α* (°)**	**Investigators**	**Airfoil**	**Max. *Cl/Cd***	***Re* (x 10^5)**	***α* (°)**	**Investigators**
A18	43.99 64.96 86.33 79.60	0.5 1.0 2.0 3.0	5.25 4.50 3.25 --	Akour et al., (2018); Karthikeyan et al., (2015)	SG6043	39.71 66.47 98.00	0.5 1.0 2.0	8.75 7.00 5.50	Rahgozr et al., (2020); Shin and Keonhoon,(2020): Akour et al., (2018); Pourrajjabian et al., (2014); Ahmed et al., (2011); Wata et al., (2011); Migliore et al., (2004); Duquette et al., (2003);
AF300	54.00	1.0	8.20	Singh et al., (2013), (2012)	SG6040	26.06 50.51 72.93	0.5 1.0 2.0	11.50 9.00 7.75	Giguere et al., (2021); Lipian et al. (2016); Karthikeyan et al., (2015)
BW-3	46.72 67.60 74.66 69.60	0.5 1.0 2.0 3.0	5.50 4.50 4.00 --	Suresh and Rajkumar, (2020); Akour et al., (2018); Karthikeyan et al., (2015)	SG6041	35.45 53.46 72.82	0.5 1.0 2.0	5.75 5.00 4.00	Lipian, et al., (2016); Karthikeyan et al., (2015); Giguere and Selig, (1998)
E387	38.09 50.98 60.66 84.35 81.70	0.5 0.8 1.0 2.0 3.0	8.50 8.00 7.50 6.75 --	Suresh and Rajkumar, (2020); Karthikeyan et al., (2015); MacTavish et al., (2013); Selig and MacGranahan, (2004), (2004a); Guglielmo and Selig, (1997)	SD7062	12.09 47.63 70.04 77.50	0.5 1.0 2.0 3.0	4.00 7.00 6.25 --	Evans et al., (2018); Karthikeyan et al., (2015); Song and Lubitz, (2014)
E216	40.73 68.50 99.17	0.5 1.0 2.0	8.00 6.00 4.00	Abdelsalam et al., (2021); Gupta et al., (2017)	SD7037	34.48 55.22 74.75 76.30	0.5 1.0 2.0 3.0	6.50 5.25 4.75	Zhang et al., (2020); Karthikeyan et al., (2015); Matsumiya et al., (2010);
E422	5.27 29.50 60.01	0.5 1.0 2.0	7.75 2.25 9.50	Wata et al., (2011)	SD7032	31.95 56.30 77.87 83.40	0.5 1.0 2.0 3.0	7.50 5.50 4.75 --	Karthikeyan et al., (2015); Giguere and Selig, (1998)
E555	27.83 51.15 69.11	0.5 1.0 2.0	10.50 8.50 7.50	Gupta et al., (2017)	S833	27.54 39.40 54.83	0.5 1.0 2.0	9.50 8.50 6.50	Hasan et al., (2017); Prasad et al., (2014)
NACA 2414	29.23 47.77 65.07 66.60	0.5 1.0 2.0 3.0	8.75 7.50 6.75	Karthikeyan et al., (2015)	S822	27.66 42.69 68.55 69.40	0.5 1.0 2.0 3.0	9.50 8.50 7.00 --	Zhang et al., (2020); Hasan et al., (2017); Karthikeyan et al., (2015); Prasad et al., (2014); Selig and MacGranahan, (1998)
NACA 2408	37.42 52.56 66.55	0.5 1.0 2.0	5.50 5.00 4.00	Tummala et al., (2016); Hirahara et al., (2005);	NREL S826	34.60 60.86 82.99	0.5 1.0 2.0	9.50 8.25 7.25	Krogstad and Lund, (2012)

2.2.2 Airfoil Selection for SWTs

Properly selecting airfoils is critical for design and manufacturing turbine blades, absorbed by BEMT. When choosing an airfoil for rotor blades, it is crucial to consider both its aerodynamic properties, its size and shape. Traditionally, the selection process has focused on achieving the optimal C_l / C_d for the target *Re*. However, it is essential to carefully assess these metrics when dealing with SWTs, which often operate under low *Re* conditions. According to research conducted by Bianchini et al., (2022), Tummala et al., (2016), Treuren, (2015) and McTavish et al., (2013), the low *Re* range is defined as $30{,}000 \leq Re \leq 300{,}000$. Based on this criterion, various airfoils have been investigated for their suitability in the design of SWT blades. Table 2.2 displays a selection of these airfoils and their corresponding aerodynamic attributes at $\mathrm{Re} = 0.5\times10^5$, 1.0×10^5, and 2.0×10^5. Within the realm of aerodynamics, a broad range of airfoils exist, each differing in type, size, and configuration. Although numerous designs have been crafted for traditional aviation purposes or to serve in sizable wind turbines, merely a handful are acknowledged in the wind power industry, specifically for SWTs. These selected airfoils are often the subject of repeated studies or applications to assess their suitability for different uses. Table 2.2 lists several airfoils, including SG6043, E216, E387, SD7062, NACA0012, S822, and NACA4418, that have been investigated for use in SWTs. However, despite showing potential in SWT applications (Abdelsalam et al., 2021; Akour et al., 2018; Rocha et al., 2018; Singh et al., 2012), airfoils such as AF300, E216, A18, E387, NACA63415, and others have received less attention from researchers.

Research has shown that the NACA series airfoils, initially designed for the aviation industry, have been applied SWTs since the mid-1980s (Tummala et al., 2016; Treuren, 2015; Giguere and Selig, 1997). These studies revealed that specific NACA airfoils, particularly the NACA44XX, NACA00XX, and NACA24XX series, have demonstrated effective aerodynamic performance in both VAWT and HAWT (Sheldahl and Klimas, 1981). The SG60XX series, crafted by Giguere and Selig, (1997) presents various airfoil segments known for their promising attributes, especially their ability to achieve high lift and low drag at low *Re*. Giguere and Selig, (1997) have also recommended employing the SG60XX airfoils in the development of SHAWTs. Based on the literature review and the information provided in Tables 2.1 and 2.2, the airfoils suitable for use in SWT are illustrated in Fig. 2.6. This information is likely to be highly valuable for researchers and developers interested in investigating these airfoils further.

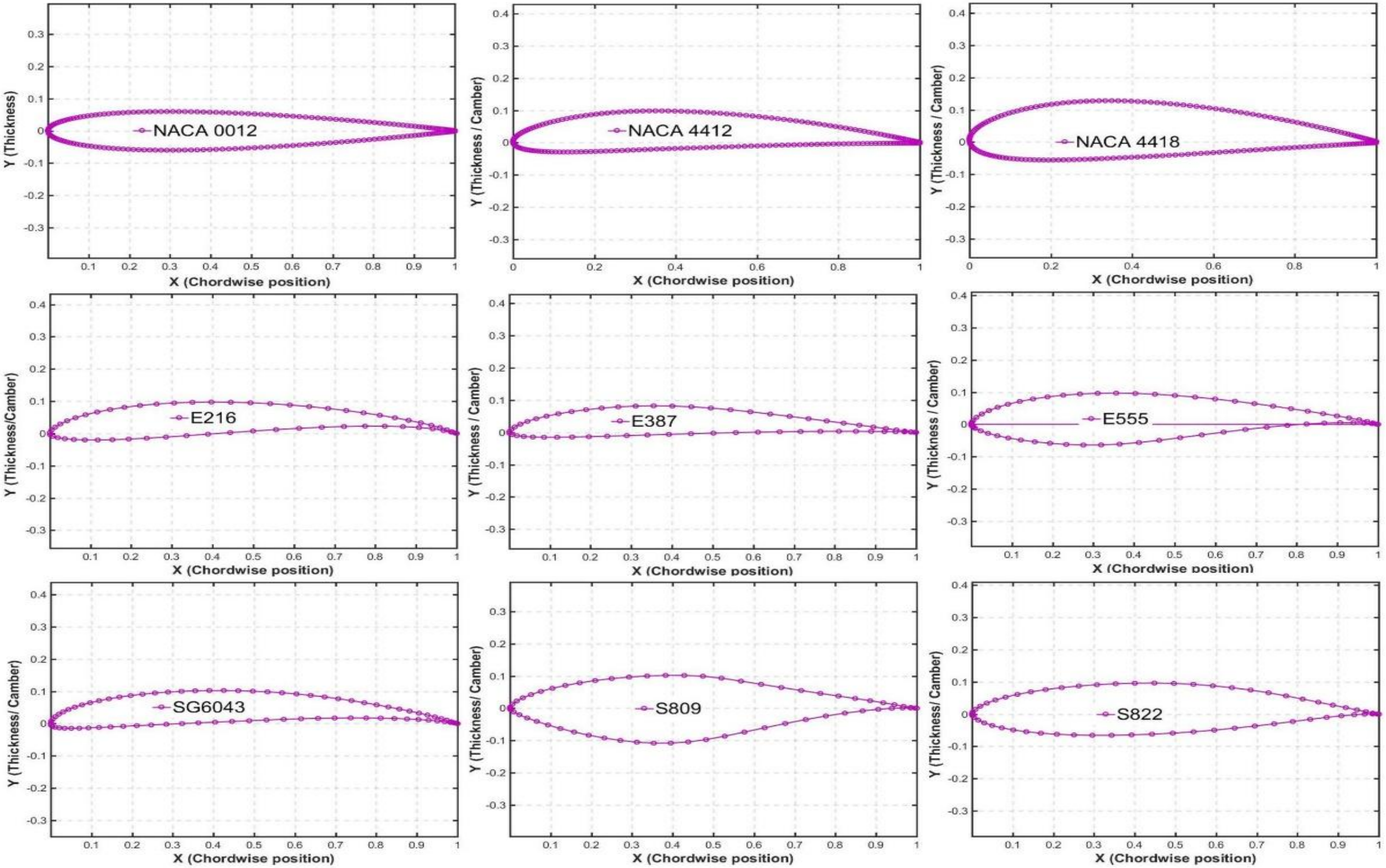

Fig. 2.6 Some potential airfoils for SWTs (Kassa et al., 2024; Siram et al., 2022)

There are various flow control mechanisms and attachments that can further enhance airfoil performance. These flow control techniques are commonly used in the aerospace industry for wings, fans, rudders, turbines, and other applications (Gad-el-Hak, 2007). According to Green, (2008), when high angle of attack (α) attached flow is achieved over an airfoil surface, it results in improved operational capability, performance, range, and endurance. Gad-el-Hak, (2007) recognized the potential of controlling flow through active, passive, and hybrid methods. The distinction between the first two lies in the use of actuators for active techniques, unlike passive ones. Conversely, the technique of active flow control encompasses the utilization of devices that energize the flow, such as actuators, synthetic jets, among others. The inclusion of these attachments and provisions initiates the process of flow separation, commonly referred to as separation bubbles. This results in significant changes to various aerodynamic properties, including lift, drag, and the transition and reattachment processes as shown in Figure 2.7 (Aftab et al., 2016; Gad-el-Hak, 2007). This segment highlights previous research focused on the impact of flow control techniques and airfoils on wind turbines.

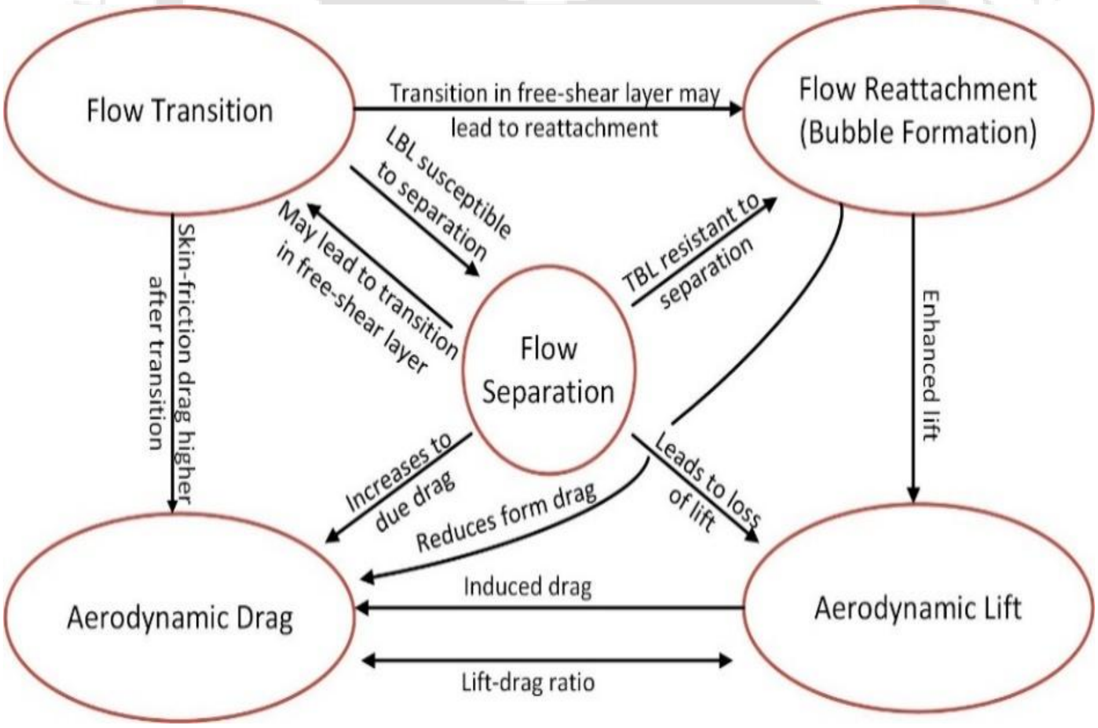

Fig. 2.7 Interrelation between flow separation and aerodynamic features (Aftab et al., 2016; Gad-el-Hak, 2007)

2.2.3 Effect of Rotor Geometry Configuration

The impact of rotor geometric variability on the performance of a given SWT is often analysed through various configurations such as the number of blades (N_B), solidity (σ), yaw angle (

γ), and pitch angle (β) (Zhao et al., 2019; Tummala et al., 2016). While some of the earliest discussions on these parameters were reported by Guo et al., (2021), Jain and Saha, (2019), Tummala et al., (2016), Costello et al., (2015), and Karthikeyan et al., (2015), the majority of the reported work has been focused on LWTs. Xisto et al., (2016) reported the impact of N_B on wind turbine performance. Their study considered the effect of solidity and evaluated the performance of rotors using various symmetric NACA00XX airfoils (NACA0006, NACA0010, NACA0015, and NACA0018) with differing airfoil thickness. The wind turbines were operated within a range of $0.5 < \lambda < 1.5$ and $N_B \leq 6$.

During the initial analysis, it was discovered that many wind turbine models do not consider the impact of yaw angle (γ) or wake deflection. The significance of γ arises from the fact that precise yawing can help maintain rotor performance during omnidirectional wind gusts. Recent studies have explored the impact of γ on wind farm performance (Medici and Alfredsson, 2008; Grant and Parkin., 2000), but it has been found that SWTs are minimally affected. Bahaj et al., (2007) presented research on the significance of γ and β on HAWT rotor performance, examining both factors simultaneously in a water tunnel at a hub pitch angle of 20° and 25°. The detrimental impact of γ effect is apparent, although there are promising reports (Medici and Alfredsson, 2008; Grant and Parkin., 2000) when multiple rotors are clustered together. Additionally, it's important to examine the impact of yawing on a cluster of SWTs experiencing omnidirectional wind gusts. To fully understand the flow dynamics of wind turbine wake in a clustered formation, a comprehensive review is provided in the following section.

The literature reveals a glaring lack of thorough turbulence characterisation under low-*Re* conditions, coupled with vertical–horizon wake mapping, and high-resolution near-wake measurements for small HAWTs. There are also a few systematic studies of essential factors, including input turbulence, yaw misalignment, and tip spacing. There are substantial gaps in our knowledge of small-scale wake physics since the available datasets are mostly restricted to moderate-*Re* PIV investigations, global power or torque measurements without corresponding wake information, or CFD results that frequently lack strong experimental validation. Further, no unified design framework currently links Low-Re blade aerodynamics, wake evolution behaviour, turbine spacing requirements for SWT layouts, and ideal operating tip-speed ratios for efficient wake control. Consequently, design strategies for small HAWTs remain fragmented and poorly integrated.

2.2.4 Summary of SWT Literature

SWTs face several design limitations, including sensitivity to wind variability, reduced aerodynamic efficiency at small scales, and the complexity of optimizing multiple interacting components, following are some of the important observations in references.

- SWTs have compact size, typically with rotor diameters less than 5 m and power capacities in a few kilowatts, makes them suitable for residential, rural, and space-limited installations. SWTs operate under specific aerodynamic conditions characterized by low $Re = 0.3\times10^5 - 3\times10^5$ and low $\lambda = 0.5 - 6$.
- One of the key factors that determines SWTs performance is airfoil selection. Therefore, airfoils with high lift-to-drag ratios, delayed stall behaviour, and stable performance at low *Re* are preferred. SG6043, E216, E387, SD7062, NACA0012, S822, and NACA4418 have shown improved C_P under these conditions.
- The N_B significantly influences torque generation, particularly at very low tip-speed ratios ($\lambda < 1.5$), where more blades can enhance performance. Other geometric parameters such as β, σ, and γ also affect aerodynamic loading and overall energy capture.

2.3 Literature Review on Multi-Rotor System

Having as much rated capacity on one support structure as possible is ideal, especially offshore, the wind industry works to keep energy costs as low as possible. Since a wind turbine's substructure usually accounts for a significant capital cost, expanding the turbines' size and power rating is a straightforward method to lower energy costs (Manwell et al., 2009). However, the maximum size of single-rotor wind turbines is limited by economic and physical constraints. According to Sieros et al., (2012), the loads created by self-weight in the tower and blades of a wind turbine grow more quickly as the rotor's radius increases.

MRS is becoming increasingly well-known as an effective and scalable substitute for traditional single-rotor designs. Multiple rotors are positioned on a standard support structure in these systems, enabling a modular approach to power output expansion without the drawbacks of giant rotor blades. Using many small turbines on a single support structure rather than a single, enormous rotor avoids the square-cube law, and material costs for blades and drivetrain components are significantly reduced. Jameson and Branney, (2012) demonstrate that the blades and major drivetrain components of an MRS have a mass that is ‘n’ times that of a comparable single-rotor system so that MRS can save substantial money on material expenditures.

Numerous studies conducted at Kyushu University in Japan (Göltenbott et al., 2017; Ohya et al., 2017) have demonstrated that grouping turbines can raise the C_P, which can raise the amount of energy captured annually. These studies indicate that while clustering wind lens turbines can significantly improve C_P, clustering conventional turbines yields small gains. C_P was also shown through simulations in the Innwind project, where an MRS consisting of 45 turbines is expected to increase power by 8 %. Operation, maintenance, and installation costs are also expected to be reduced using the MRWT concept, as components would be small enough to use small vessels without the required specialist equipment. If one small rotor fails, only a small portion of the total power is lost and can be replaced at the next regular service interval without significant loss of revenue. The Innwind project also compares the levelized cost of energy (LCOE) of the conceptual 20 MW 45-rotor MRS with two 10 MW reference wind turbines and estimates that the MRS would have a reduction in LCOE of 15 %.

2.3.1 Evolution and Research Trends

MRS have been around in wind energy for a few decades. Engineers and researchers studied MRSs in the 1970s and 1980s to boost power production without appreciably enlarging the size of each rotor. To investigate aerodynamic interactions and structural load-sharing, NASA and other government agencies conducted experimental work using several rotors installed on a single tower, one of the first implementations. However, the concept of MRS was mostly shelved because of technological constraints, a dearth of sophisticated control systems, and the prevalence of single-rotor commercial versions.

The 21st century saw a resurgence of interest in MRS due to developments in materials science, control algorithms, and offshore installation methods. An important turning point was the 2016 debut of the Vestas multi-rotor demonstration. With four 225 kW rotors affixed to a single structure, the prototype showed great promise for improving performance and distributing structural load. According to Jameson and Branney, (2012), it also demonstrated less strain on individual parts and made transportation and installation procedures easier to handle.

Another notable contribution is research from the European Innwind project, which examined the application of multiple rotors in offshore conditions. The main topics of these investigations were the viability of large-scale MRS and its impacts on cost, electricity output, and the environment. According to numerical simulations and optimisation models, MRS should perform better than single-rotor systems if properly built, particularly regarding energy.

2.3.2 Blockage Effect in MRS

In MRS, the term "blockage effects" describes the aerodynamic interference brought on by several rotors working nearby. A large rotor area about the available airflow can block and reroute wind, changing the pressure distribution and creating local turbulence. On the one hand, the larger pressure differential can improve energy capture by accelerating the flow around the rotor edges. Conversely, rotors near one another may interfere, decreasing rotor efficiency and resulting in performance penalties.

According to studies, rotor spacing, configuration geometry, and operating conditions significantly impact the degree of blockage effects. According to parametric simulations by Bortolotti et al., (2020), lateral spacing larger than two rotor diameters can efficiently mitigate most blockage-related losses. The careful positioning of rotors could take advantage of localised flow augmentation without experiencing severe aerodynamic degradation, as further evidenced by Computational Fluid Dynamics (CFD) simulations. Staggered configurations, vertical stacking, and using veiled or diffuser-augmented rotors are emerging design techniques that enhance performance while controlling obstruction. For instance, Kosasih and Tondelli, (2016) showed that adding diffusers to each rotor could aid in better air funnelling, reducing wake overlap and loss.

2.3.3 Wake Flow Behind MRS

The main emphasis of MRS research is wakes interactions. Multiple overlapping or diverging wake patterns, which are controlled by the rotor configuration and the surrounding wind conditions, make the wakes behind MRS more complex than those behind single-rotor systems. A schematic diagram as shown in Fig. 2.8 represents the wake behind the pair of rotors in MRSs in which tip spacing, rotor- axis, central-axis, as well as wake overlap area are mentioned.

Wakes can be redirected by yaw control of individual rotors to lower downstream losses. Active yaw steering in MRS setups improves wake deflection, lowers turbulence intensity, and increases downstream power gains, according to studies by Munters and Meyers, (2018). Maximising wake recovery and reducing inter-rotor interference is possible by optimising the vertical and horizontal space between rotors. According to research by Hezaveh and Bou-Zeid, (2018), have conducted the studies in which the wake overlap is greatly decreased when separation is increased beyond *3D–4D*.

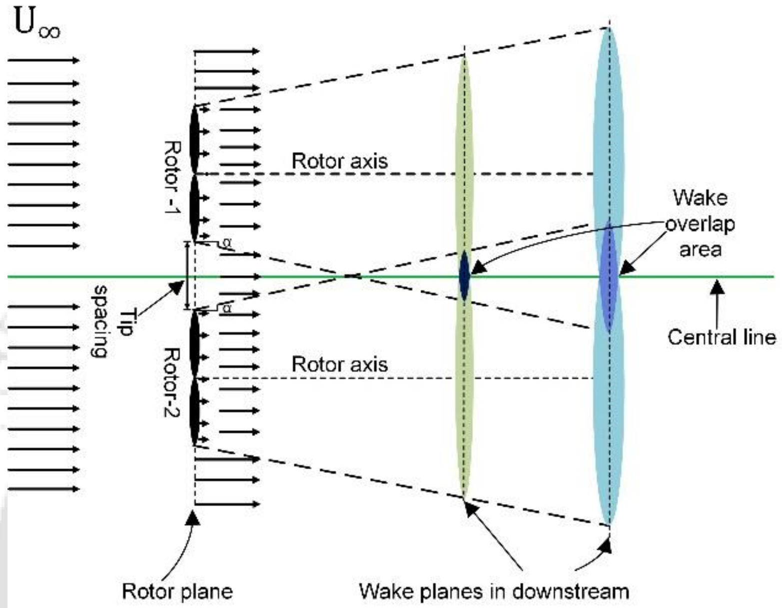

Fig 2.8 Schematic diagram for wake interaction in between pair of rotors in MRSs

According to CFD and wind tunnel research (Hezaveh and Bou-Zeid, 2018; Bastankhah and Porté-Agel, 2016), the MRS can enhance wake mixing by superposing wakes, which results in improved entrainment and a quicker recovery of velocity in the wake region. MRS can outperform comparable single-rotor farms in closely spaced arrays, as demonstrated by wake steering and farm-level control (Speakman et al., 2021). Distributed rotor control in MRS allows for precise control of local flow fields to optimise net energy capture. MRS can prevent coherent wake deficits from forming, enabling downstream turbines to receive more consistent and faster intake, according to experimental and LES investigations (Churchfield et al., 2013).

Additionally, new MRS configurations, including hexagonal, staggered, or circular layouts, are being investigated for their potential to increase aerodynamic performance and wake dispersion at the wind farm level (Ghaisas et al., 2020).

The majority of the current understanding of MRS aerodynamics stems from full-scale farm setups, or high-*Re* wind-tunnel research. On the other hand, little is known about the interaction mechanics that regulate small, low-*Re* multi-rotor configurations. The nature of mutual induction between adjacent wakes, the decay behaviour of coherent tip vortices, the mechanisms underlying constructive or destructive interference, and the relationship between tip spacing and wake recovery are some of the significant gaps. These outstanding problems hamper the creation of trustworthy design guidelines for low-*Re* MRS layouts.

2.3.4 Summary of MRS Literature

The literature confirms the expanding potential of MRS in contemporary wind energy systems. Previous research has progressed from conceptual inquiry to full-scale prototypes and sophisticated computational modelling. MRS is appealing for offshore and distributed generation applications due to its benefits, which include modularity, reduced structural stresses, operational redundancy, and control flexibility. Several key factors continue to drive research interest in MRS:

- MRS offers a flexible and modular solution in response to the growing demand for sustainable and scalable renewable energy sources.
- MRS are becoming increasingly crucial for floating platforms, since distributed loading can provide improved stability and less complicated mooring systems.
- Advanced flow and power optimisation are made possible by the possibility of individual rotor yaw and pitch control.
- MRS may be feasible in populous or sensitive areas due to smaller rotors that cause less visual and aural disruption.
- Distributed rotors allow for more flexible management of power electronics, which improves grid compatibility and lowers transient loads.

2.4 Literature Review on Wake Dynamics in Wind Turbines

When considered an isolated unit, a wind turbine can act as an independent energy source. Nonetheless, when transitioning to a collective framework, such as wind farms, staggered arrangements of wind turbines incorporating multiple rotors, it becomes crucial to delve into the dynamics of wake interference, as the interaction among turbines can significantly influence the overall performance of the system. This necessity forms a core part of the research goals concerning the design of turbines with multiple rotors. It prompts a thorough examination of how the aerodynamic wake generated by a turbine.

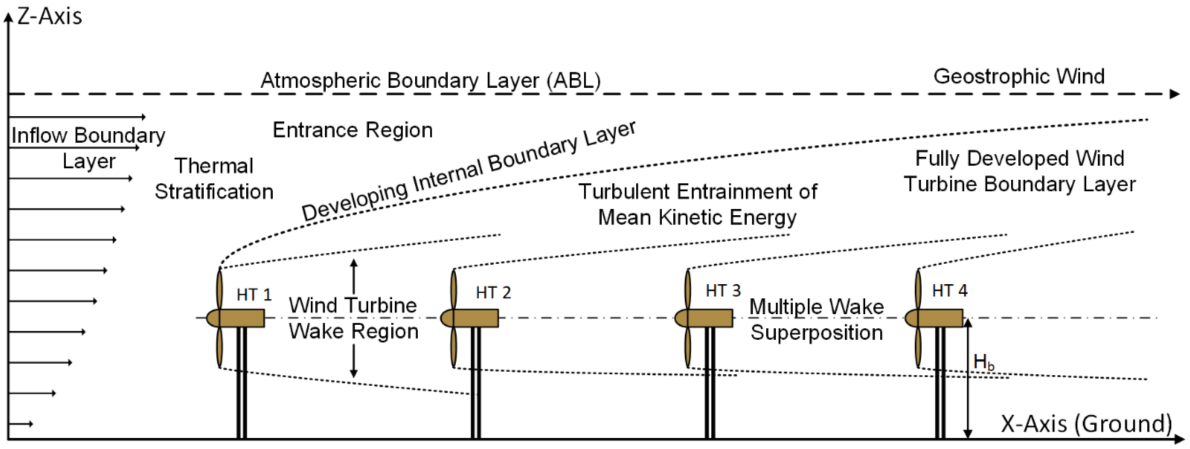

Fig. 2.9 Depiction of wind turbine array boundary layer (Steven and Meneveau, 2017)

Ensuring optimal efficiency in wind farms is a pivotal concern for developers and has attracted considerable attention from researchers worldwide. The primary difficulties in wind farm modelling involve expanding and predicting wind turbine wakes. Over time, various analytical models have been developed to understand the wake propagation process better. These models are crucial because they reveal how turbines within an array or cluster are affected by various aerodynamic loads. Such loads are broken down into categories like the wind turbine wake itself, the atmospheric boundary layer (ABL), and inflow turbulence, among others. A diagram illustrating these flow fields is shown in Fig. 2.9. The intersection of these flow field structures, as depicted in Fig. 2.9, leads to the formation of a unique wind farm boundary layer (WFBL). Reducing the extent of this WFBL presents a significant challenge for those designing the layout of wind farms. The size of the WFBL and its impact on wind farm development depends on several key factors, which are detailed in Fig. 2.10, highlighting their critical role in effective wind farm modelling.

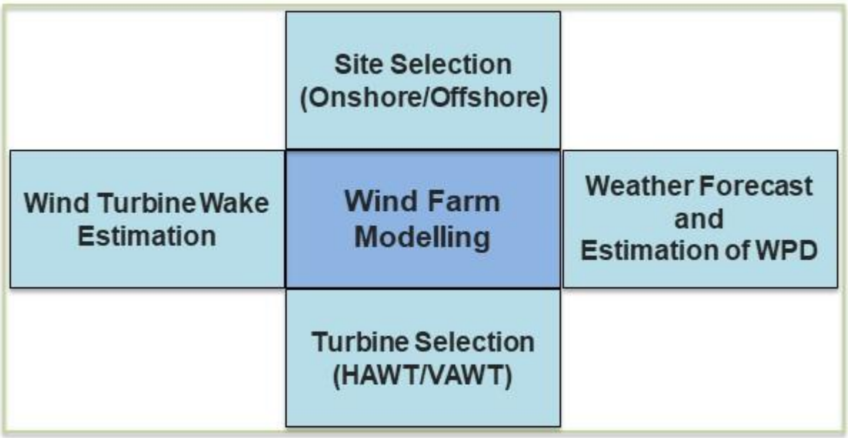

Fig. 2.10 Importance factors of wind farm modelling

2.4.1 Importance of Wake Studies in Wind Energy Applications

According to the aerodynamic principles governing wind turbines, the maximum theoretical efficiency of this energy conversion is limited to approximately 59% (Manwell et al., 2009). This limitation arises because, for air to continue flowing through the rotor, some kinetic energy must remain in the airflow after it passes through the turbine. As a result, the wind slows downstream, leading to a loss of momentum. This slowdown has essential implications for turbines located downstream. These downstream turbines often operate under suboptimal conditions due to the wake generated by upstream turbines. Studies have shown that downstream turbines may produce only 20–46% of the power they could achieve in undisturbed wind flow (Adaramola and Krogstad, 2011). For instance, McKay et al., (2013) reported a 35% reduction in energy output for the downstream first turbine during a six-month observational study using supervisory control and data acquisition systems. The extent of this wake-induced energy loss is highly dependent on the spacing between turbines. Barthelmie et al., (2007), in a field study conducted at the Middelgrunden offshore wind farm in Denmark, observed a 10% reduction in output at a spacing of *4D*. Similarly, Sørensen and Shen (2002), while studying the Horns Rev wind farm, reported a 12.4% performance drop at a larger spacing of *8D*. These findings illustrate that increased spacing can reduce but not eliminate wake losses. Moreover, the influence of wake effects can vary significantly between offshore and onshore wind farms, mainly due to differences in ambient turbulence intensity (T_a). Offshore environments typically exhibit lower turbulence levels, generally 6–8%, while onshore turbulence levels tend to be higher due to land surface roughness and obstructions (Barthelmie et al., 2003). These insights emphasise the critical importance of accurate wake modelling in wind farm design and operation. Proper assessment of wake interactions is essential for reliable predictions of annual energy production (AEP), particularly as wind farms become larger and more densely arranged.

2.4.2 Structure and Evolution of Wind Turbine Wakes

Wind turbine wakes are categorized into two main types: the near wake and the far wake. The near wake refers to the area immediately behind the rotor plane, as depicted in Fig. 2.11, where the characteristics of the flow field are typically analysed up to a distance of *4R* or *6R*. In Fig. 2.11, *R* denotes the rotor radius, while the non-dimensional distances *x/R*, *y/R*, and *z/R* correspond to the streamwise, lateral, and vertical directions, respectively. This region's wake characteristics are often linked with the geometry and aerodynamics of the rotor blades, as noted by Vermeer et al., (2003). Studies of the near wake primarily concentrate on vortex behaviour without considering the topography. Although many wake models treat the near wake as having uniform, steady, and parallel flow conditions, the reality is considerably more complex due to factors like wind shear, interactions with the rotor tower, effects of the nacelle, yaw, dynamic stall, and aero-elastic phenomena, all of which are crucial for accurately predicting the long-term power output of both individual wind turbines and entire wind farms (Steven and Meneveau, 2017; Sørensen and Shen, 2002).

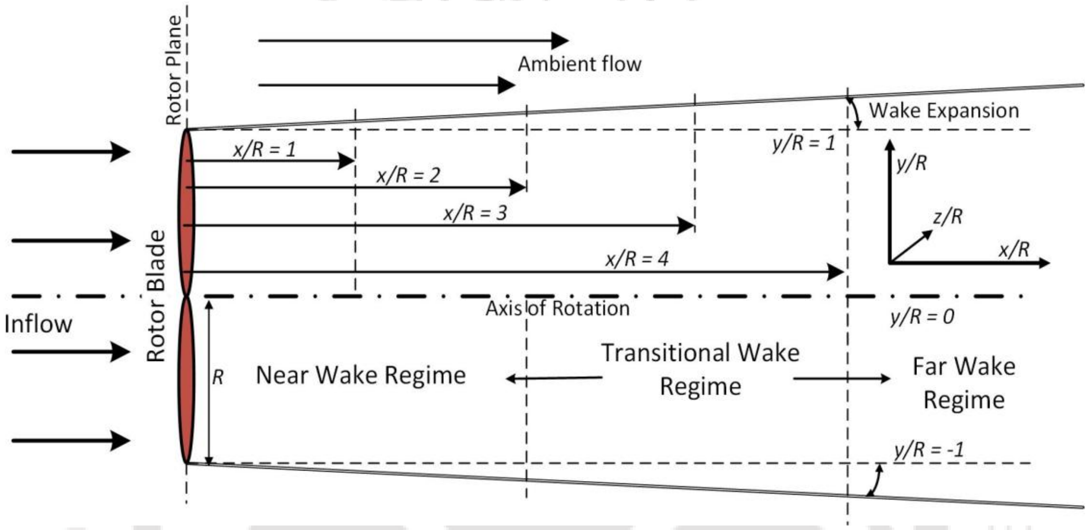

Fig. 2.11 Wind turbine downstream wake regimes distribution

Conversely, the far wake extends beyond the point where the continuous helical vortex structure vanishes, and it is primarily relevant for wind farm (Steven and Meneveau, 2017; McKay et al., 2013; Vermeer et al., 2003). The termination of the far wake is typically identified when the flow fully develops or when the normalized velocity equals one. While many models indicate a 70-90% recovery of flow within 16R-24R from the rotor plane, a minimum spacing of 10R between turbines is often recommended to mitigate wake effects while considering operational costs, land usage, and transmission losses (Chen and MacDonald, 2012; Manwell et al., 2009). The strategic placement of wind turbines becomes increasingly complex, with limited land available for wind farm development.

2.4.2.1 Near Wake Regime

The flow field immediately downstream of the rotor, where the impacts of rotor-induced flow and the breakdown are most noticeable, is referred to as the "near wake region," as the name implies. While the near wake is essential for wind turbine aerodynamics, there aren't many empirical models that properly represent it, and there aren't many confirmed relationships in the literature. Vermeulen, (1980) made one of the initial and most significant contributions when he developed an empirical relation to estimate the near wake length based on the wake growth rate (represented as *dr/dx*), as shown in Eq. (2.8).

$$x_n = \frac{nr_0}{\left(\frac{dr}{dx}\right)} \tag{2.8}$$

$$\text{where,}\ \ r_0 = R\sqrt{\frac{m+1}{2}}$$

$$m = \frac{1}{\sqrt{1-C_T}};\quad n = \frac{\sqrt{0.214+0.144}\left(1-\sqrt{0.134+0.124m}\right)}{\left(1-\sqrt{0.214+0.144m}\right)\sqrt{0.134+0.124m}}$$

The wake growth rate $\left(\frac{dr}{dx}\right)$ is expressed by Eq. (2.9)

$$\frac{dr}{dx} = \sqrt{\left(\frac{dr}{dx}\right)_a^2 + \left(\frac{dr}{dx}\right)_m^2 + \left(\frac{dr}{dx}\right)_\lambda^2} = \sqrt{G_a^2 + G_m^2 + G_\lambda^2} \tag{2.9}$$

where, $\left(\frac{dr}{dx}\right)_a = G_a = 2.5I_a + 0.005;\ \left(\frac{dr}{dx}\right)_m = G_m = \frac{(1-m)\sqrt{1.49+m}}{(1+m)9.76}$

and, $\left(\frac{dr}{dx}\right)_\lambda = G_\lambda = 0.012B\lambda$

where G_α, G_m, and G_λ represent the contributions to wake growth rate from ambient turbulence, shear-generated turbulence within the wake, and mechanically induced turbulence, respectively. The parameter C_T and λ are the thrust coefficient and tip speed ratio, respectively, while I_a and N_B correspond to the ambient turbulence intensity and the number of blades.

Another early empirical formulation describing the near wake region was introduced by Lissaman, (1979). His model conceptualises wake growth as a result of turbulent entrainment at the wake's outer boundary, wherein momentum and mass from the free stream are incorporated into the wake. The model assumes a simplified flow structure characterised by a constant pressure field. According to Lissaman's approach, the initial radius of the near wake can be defined by Eq. (2.10).

$$r_o = R\sqrt{\frac{(m_w + 1)}{2}} \qquad (2.10)$$

The radius of wake at the end of near wake regime is expressed by Eq. (2.11)

$$r_c = \frac{r_o}{(0.214 + 0.144 m_w)^{0.5}} \qquad (2.11)$$

Here, m_w is the ratio of freestream velocity to the velocity of wake (U_{CW}) at the core of turbine wake as given by Eq. (2.12).

$$m_w = \frac{U_\infty}{U_{CW}} \qquad (2.12)$$

Lissaman suggests that the development of wake characteristics in the near wake region is primarily shaped by three main turbulent components. In contrast, the far wake's evolution is largely driven by the T_a. The transverse profile of the wake is characterized by a shear layer that surrounds the wake core. The near wake region is considered to end where this outer shear layer meets the centerline of the wake. Beyond this point, the velocity deficit gradually decreases as the distance from the rotor plane increases.

2.4.2.2 Far Wake Regime

The far wake regime refers to the portion of the wind turbine's flow field that typically extends beyond 3*D* –5*D* downstream from the rotor (Fig. 2.10). This region is generally analysed until the normalised velocity approaches unity, which is commonly observed between *8D* and *12D* downstream (Steven and Meneveau, 2017; Vermeer et al., 2003). The far wake is exciting in wind farm modelling, as understanding its behaviour is critical for optimising turbine placement and overall farm performance. Although the termination of the far wake can be approximated by monitoring the normalized velocity recovery, identifying its onset remains ambiguous. Some definitions suggest it begins immediately after the near wake, while others place its origin toward the latter part of the transitional region. Schepers, (2003), for example, proposed that the far wake begins at approximately *2.25D*, characterized by a hat-shaped velocity deficit; however, this threshold remains debatable. Despite this uncertainty, many studies report that the wake recovers 70–90% of the free-stream velocity between *8D* and *12D*. Nevertheless, practical constraints such as installation costs, land availability, and transmission losses often lead to a recommended turbine spacing of at least *5D* to mitigate wake interference (Chen and MacDonald, 2012; Manwell et al., 2009).

A key complexity in modeling the far wake arises from additional turbulence contributions, including shear generated by the turbine nacelle, supporting tower, and the ABL. Sam et al., 2017 observed that the ABL can significantly influence far wake behavior. Their findings indicate that under uniform inflow conditions, the initial rotor-induced shear in the near wake transforms into a turbulent structure, progressively dissipating downstream due to turbulent mixing, energy dissipation, and vorticity annihilation. Several modeling approaches, including kinematic and field-based methods, are specifically designed to capture far wake dynamics. These models are further discussed in subsequent sections.

2.4.2.3 Transitional Near-to-far Wake Regime

In addition to the well-studied near and far wake regions, the transitional wake regime has also emerged as an area of interest in wind turbine wake modelling. Although limited research has been conducted on this regime, it is generally considered to span the region between approximately 2*D*-4*D* downstream of the rotor. Within this range, the coherent helical vortex structures formed in the near wake begin to lose their integrity and transition into more turbulent, disorganized flow. Accurate characterisation of the transitional regime is essential for improving predictions of wake behaviour and its expansion. Advanced diagnostic tools such as Particle Image Velocimetry (PIV) and Light Detection and Ranging (LiDAR) offer promising avenues for capturing the complex flow dynamics present in this region. One of the few models addressing the transitional regime is one proposed by Lissaman, (1979). In his formulation, the velocity deficit within the transition zone is represented as a linear combination of flow profiles. The wake radii at the start (r_c) and end (r_F) of the transitional region are defined by Eqs. (2.13) and (2.14), respectively.

$$r_c = \left(\frac{dR_w}{dx}\right)x_c + r_o \tag{2.13}$$

$$r_F = \frac{r_o}{(0.134 + 0.124m_w)^{0.5}} \tag{2.14}$$

And the extent of transition regime (x_t) is expressed by Eq 2.15

$$x_t = \frac{x_c(0.214 + 0.144)^{0.5}\left(1-(0.134+0.124m_w)^{0.5}\right)}{\left((0.134+0.124m_w)^{0.5}\right)\left(1-(0.214+0.144)^{0.5}\right)} \tag{2.15}$$

where R_w is radius of wake, x_c is the extent of near wake downstream of the rotor, dR_w/dx is the wake growth rate, and r_o is the near wake radius close to the rotor plane.

2.4.3 Analytical and Empirical Wake Models

Analytical and empirical wake models execute a crucial role in analysing velocity deficit, wake recovery, and power losses in wind turbine arrays. The wind turbine wake models are categorized into the Kinematic, Field, and Wake added turbulence models, as depicted in Fig. 2.12. These models could be for single or for multiple turbines and typically express the streamwise velocity deficit as a function of downstream position using assumptions of self-similar wake growth, steady induction, and momentum conservation. Although these formulas have been thoroughly proven for large HAWTs operating at high *Re* under highly turbulent air intake, their direct applicability to SWTs operating at low *Re* remains essentially limited. Laminar separation bubbles, early stall, and lower lift-to-drag ratios have a significant impact on blade boundary layers in low *Re* regimes, altering thrust generation and induction behaviour.

The kinematic wake model employs the momentum equation to estimate the velocity deficit in the wake of a wind turbine. However, it does not account for variations in turbulence intensity (TI) and, as such, must be supplemented with a separate turbulence model. Additionally, ambient turbulence effects are not incorporated, resulting in the assumption of negligible perturbations in the velocity deficit. The TI is typically assumed to be axisymmetric, leading to a self-similar wak e distribution. This self-similarity observed in velocity, velocity deficit, and TI profiles is a defining characteristic of kinematic wake models used in wind turbine wake analysis (Vermeer et al., 2003). Researchers such as Larsen, Jensen, and Frandsen have developed several foundational kinematic models, among others, as illustrated in Fig. 2.12. These models are discussed in the following sections.

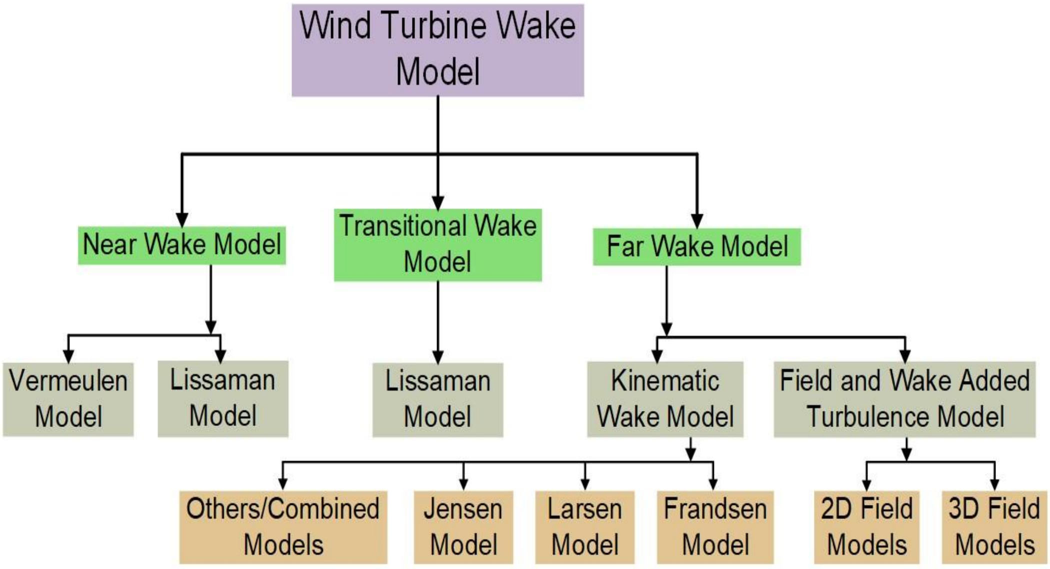

Fig. 2.12 Wind turbine wake model's hierarchy

Gaussian wake models provide a better approximation of the wake distribution for small rotors because they incorporate turbulence intensity, thrust coefficient, and wake expansion rates. However, their calibration is based on high-Re conditions where, tip vortices break down more rapidly, wake transitions to a fully turbulent state earlier, and wake width follows classical Gaussian growth. For small-scale rotors, the parameters σ_y and σ_z evolve differently due to low-Re vortex stability and slower merging. The analytical model is expressed as equation 2.16:

$$\frac{\Delta U}{U_\infty} = \left(1 - \sqrt{1 - \frac{C_T}{2\sigma_y\sigma_z/R^2}}\right) exp\left[-\frac{1}{2}\left(\frac{y^2}{{\sigma_y}^2} + \frac{z^2}{{\sigma_z}^2}\right)\right] \tag{2.16}$$

where, σ_y and σ_z are lateral and vertical wake width at downstream distance.

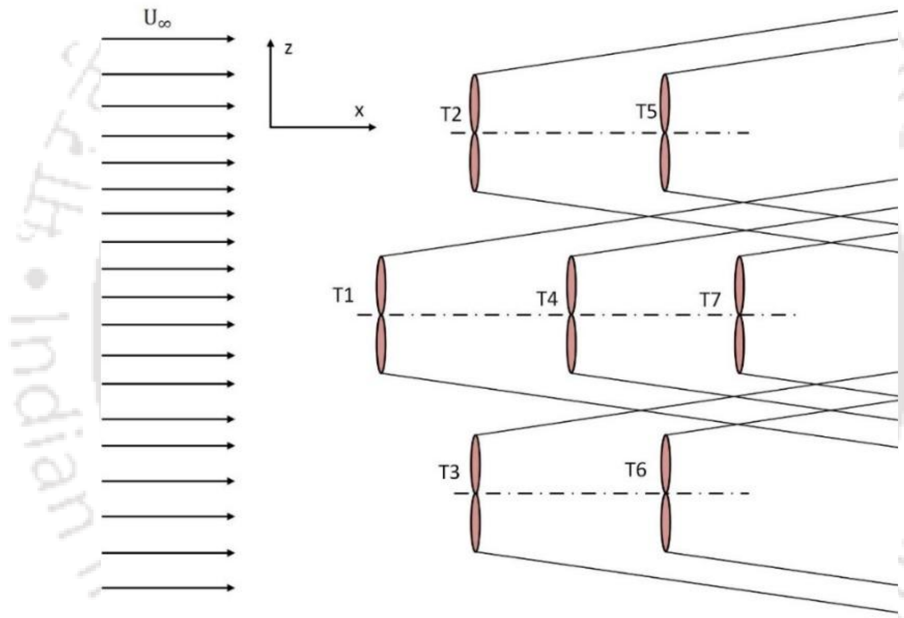

Fig. 2.13 Multiple wake effect in windfarm (Kuo et al., 2015; González-Longatt et al., 2012)

The wake models discussed so far are primarily suited for analysing single-turbine wakes. However, in a wind farm environment where multiple turbines are positioned in close proximity, individual turbines can be affected by the wakes of upstream turbines, such as the influence observed on rotor T7 in Fig. 2.13. Analysing the interaction of multiple wakes is challenging due to the difficulty in visual detection and the complexity of the turbulent flow behaviour (Steven and Meneveau, 2017; Manwell et al., 2009; Vermeer et al., 2003). Several methodologies have been proposed to model wake interactions, and as outlined by Kuo et al., (2015), four principal techniques are commonly applied for multiple wake superposition, summarised in Table 2.3. The following subsection elaborates on these multiple wake models, focusing on the frameworks presented in Table 2.3.

Table 2.3: List of some wake interaction models (Kuo et al., 2015; González-Longatt et al., 2012)

Sl. No.	Description	Expression
1.	Geometric superposition	$\frac{u_i}{U_\infty} = \prod_{j=1}^{n}\left(\frac{u_{ij}}{u_j}\right)$
2.	Linear superposition of velocity deficit	$\left(1-\frac{u_i}{U_\infty}\right) = \sum_{j=1}^{n}\left(1-\frac{u_{ij}}{u_j}\right)$
3.	Sum of squares	$\left(1-\frac{u_i}{U_\infty}\right)^2 = \sum_{j=1}^{n}\left(1-\frac{u_{ij}}{u_j}\right)^2$
4.	Sum of energy deficits	$\left(U_\infty^2-u_i^2\right)^2 = \sum_{j=1}^{n}\left(u_j^2-u_{ij}^2\right)$

where u_i represents the wind speed upstream (close to rotor plane) of turbine i, u_{ij} is the wind speed at turbine i under the wake influence of turbine j and 'n' is number of turbines.

Furthermore, in the near- and intermediate-wake regions of small rotors, the fundamental concepts of classical wake theory, wake self-similarity and axisymmetric expansion, are frequently not fully established. Compared to traditional Gaussian diffusion-based formulations, the enhanced coherence of tip vortices at low Reynolds numbers delays vortex breakup, resulting in more pronounced and spatially non-uniform wake deficits. These differences become much more noticeable in MRS, where reciprocal vortex interaction and overlapping induction zones result in asymmetric wake patterns that are unrepresentable using conventional single-rotor wake superposition methods.

2.4.4 Experimental and CFD Approaches in Wake Analysis

In a rotor array or cluster, accurately characterising the wake is crucial. Researchers typically rely on experimental or numerical analyses to overcome these limitations, which provide more reliable insights. Based on such data, they can revise and refine analytical formulations accordingly. Grant and Parkin, (2000) investigated wake behaviour using a NBEMT rotor. Their findings revealed that trailing vortex circulation depends on the rotor phase and the yaw angle (γ). They recorded higher tangential velocity within 15–30% of the rotor's radial distance. Adaramola and Krogstad, (2011) also highlighted the influence of yaw angle on performance. They observed that placing the upstream turbine under yaw ($\gamma \neq 0°$) enhanced the overall power coefficient C_p, increasing the downstream rotor's $C_{p_{\max}}$ by approximately 12%. They also noted further improvement in $C_{p_{\max}}$ when increasing the rotor separation distance (x/R).

Jackson and Amano, (2017) conducted wind tunnel tests and found that the near wake regime extended to $x/R < 6$. Within $x/R \leq 4$, they observed an asymmetric velocity deficit concentrated in the lower half of the turbine. This irregular and intensified deficit resulted from turbulence generated by the tower and its interaction with the blade-induced wake. They detected high turbulence intensity (TI) near the rotor root section, with values exceeding 0.3. For dual rotors spaced *4R* apart, they reported a relatively large velocity deficit behind the second rotor ($x/R < 4$). The maximum deficit occurred after the third rotor in setups with three rotors, also spaced *4R* apart. The TI between the first two rotors ranged between 0.8% and 29% relative to the centreline. They noted significant discrepancies between experimental results and simulations, particularly near the hub region. Medici and Alfredsson (2006), (2008) observed pronounced velocity peaks at each vortex passage near the tip vortex's outer region. They also found that tip vortices propagated in the streamwise direction at about 0.75 U_∞ up to around *3D*. Beyond this point, the streamwise velocity (*U*) diminished.

Wiklak et al., (2022) conducted experimental investigations on two scaled-down wind turbine models arranged in an array with a *5D* spacing. They designed both rotors ($D = 0.2\ m$) using the S826 airfoil and applied fixed blade pitch control. The upstream rotor achieved a maximum power coefficient $C_{P_{\max}}$ = 0.23, while the downstream rotor's $C_{P_{\max}}$ varied with the λ. Their wake analysis revealed the highest velocity deficit when the rotor operated at the optimal λ. They observed a power loss ranging from 70% at *5D* spacing to 40% at *7D* for the downstream turbine. The upstream wake reduced the downstream turbine's optimal λ. Additionally, they found that spanwise offset separation between turbines offered better power extraction than streamwise spacing. Taylor et al., (2013) evaluated the use of micro turbines by assessing their effects on communities of up to 10,000 people. Their tests included various turbine models, some with capacities as high as 5 kW. Although they primarily focused on noise emissions, their study highlighted challenges related to deploying micro turbines in array configurations.

Geometric parameters influence wake characteristics, but the surface or atmospheric boundary layer (ABL) also plays a crucial role, especially for small wind turbines. While large turbines with hub heights above 50 m show minimal ABL influence, small turbines experience noticeable effects. Hancock and Pascheke, (2014) studied ABL influence under three conditions: (a) baseline neutral, (b) stable, and (c) unstable. They found larger velocity deficits under stable ABL and smaller ones under unstable conditions. In stable ABL, the velocity deficit decayed more slowly, while in unstable ABL, the decay occurred more rapidly. Field data remains essential for modelling and validating turbine wakes, particularly in small wind farms, where measurements typically occur $2D$–$4D$ above ground. Becerra et al., (2017) measured wake flow at a 15 m height in a Chilean wind site. Tools like HOMER effectively support demand and supply curve characterisation Hancock and Pascheke, (2014).

Yuan et al., (2014) explored the interaction of counter-rotating down-scaled wind turbines. Their results showed a 20% performance improvement in counter-rotating configurations over co-rotating ones. They used mixed airfoil profiles (S819, S820, S822) with a rotor radius (R) of 127 mm and hub height (H_b) of 225 mm in wind tunnel tests. Beyond $13R$, the counter-rotating influence diminished. Annoni et al., (2016) analysed wake expansion using particle image velocimetry in a three-rotor array at $5D$ spacing. At $3D$ downstream, they measured wake expansion from $0.5D$ to $0.82D$ under de-rated conditions and $0.5D$ to $0.74D$ under rated conditions, noting less expansion during rated operation. Tian et al., (2017) tested turbine models ($D = 0.25$ m, $H_b = 0.225$ m) across three wind farm layouts. Their findings identified developing, developed, and equilibrium wake states. Table 2.4 summarizes additional key observations from experimental and numerical wind turbine wake analyses.

Blockage effects, probe interference, and decreased atmospheric turbulence intensity present additional limitations for SWT research carried out in wind tunnels. The wake development becomes extremely sensitive to minute changes in inflow turbulence, surface roughness, and blade stiffness at low Re, which makes repeatability and uncertainty quantification crucial. Shear-layer instabilities, tip-vortex mutual interaction, and unstable vortex dynamics are all challenging for Reynolds-Averaged Navier-Stokes (RANS) simulations to accurately represent numerically at low Reynolds numbers. Large Eddy Simulation (LES), particularly for multi-rotor systems, provides greater fidelity but at a significantly higher computational cost. These real-world constraints underscore the ongoing importance of meticulously regulated experimental datasets that can provide a physically based understanding of SWT wake behaviour.

Table 2.4 Summary of key experimental and numerical studies on the wind turbine wake characteristics

Observation	Reference(s)
1. **Near Wake Regime**	
Near wake region defined between $1D$ and $3D$ downstream.	Grant and Parkin, (2000)
Shear layer reaches the wake axis at ~$2D$–$5D$, marking end of near wake.	Crespo et al., (1999)
Induced axial velocity is high; individual blade effects vanish after $1D$, but tip vortices persist.	Adjiri et al., (2023)
Strong rotational flow and asymmetric turbulence observed.	Kocer et al., (2011)
Phase-averaged shedding response fades beyond $x/D > 5$.	Eriksen and Krogstad, (2017)
80% and 50% streamwise velocity drop at $x/D = 2.4$ and 4, respectively.	Hyvärinen and Segalini, (2017)
Vortex rings persist up to $x/R < 8$.	Sedaghatizadeh et al., (2019)
W-shaped normalized time-averaged velocity deficit profile is evident.	--
2. **Far Wake Regime**	
Maximum velocity deficit occurs near hub height.	Barthelmie et al., (2002)
Meandering not observed in single-bladed rotors; notable in 2- and 3-bladed rotors.	Medici and Alfredsson, (2008), (2006)
Wake propagation is strongly influenced by inlet turbulence intensity (TI).	Li et al., (2017); Talvera and Shu, (2017)
Large-scale diffusion observed by $x/D = 5$; edges of wake become indistinct.	Eriksen and Krogstad, (2017)
Full flow recovery at $x/D = 14.5$ for $\lambda = 2.5$ (experimental); ~80% recovery at $7D$ (numerical).	Hasan et al., (2019)
60–70% flow recovery beyond $x/R > 12$ at low λ.	--
3. **Wake Deficit**	
Tip vortex roll-up influenced by inboard trailing edge vortex shedding.	Grant and Parkin, (2000)
Asymmetric vertical velocity deficit within $x/R \leq 2$; TI high near root ($r/R < 0.3$).	Jackson and Amano, (2017)
Maximum deficit found near 0.5R, not at centerline.	Magnusson (1999)
Centerline deficit ~65% at $0.5D$–$1.75D$, decreasing to ~25% at $x/D = 2.5$.	Kocer et al., (2011)
Lateral and vertical velocities increase near rotor and decay downstream.	Zhang et al., (2013)
Axisymmetric lateral profile; peak at y/R = 0.2.	Eriksen and Krogstad, (2017)

TI increases to $x/R \leq 6$; slightly drops from $6 < x/R < 8$, then rises again at $x/R \geq 10$.	Mo et al., (2013)
Wake instability begins at $x/R \geq 8$ and expands with increasing U_∞.	Mo et al., (2013)
Accuracy of wake instability modeling depends on mesh quality.	Carrión et al., (2015)
Maximum velocity deficit at $z/R = 0.50$ (lateral) and $y/R = -0.25$ (vertical); increases with λ.	Li et al., (2017)
4. Helical and Tip Vortex	
Trailing vortex circulation influenced by phase and yaw angles; highest at $\gamma = 0°$ and high azimuth.	Grant and Parkin, (2000)
Towards the outer part of the tip vortex, a higher velocity peak is obtained at every vortex passage. The tip vortex moves radially with a low frequency	Medici, D., and Alfredsson, (2008), (2006)
Tangential velocity direction same as the rotor rotation	Adjiri et al., (2023)
Influence of tip vortices is higher on axial velocity than on tangential velocity. The velocity induced by bounded circulation stay in same azimuth position. The tip vortices remained intact with the helical vortex till 1D	Adjiri et al., (2023)
Persistent vortices are observed till *2D–3D*, however, beyond $x/D \geq 5$, the wake rotation starts diminishing	Zhang et al., (2013)
The helical vortex structure interacts and pair-up, merge and breakup within $x/D = 3$	Eriksen and Krogstad, (2017)
There is consistent vortex ring within $x/R < 8$. The ring of tip vortices is visible up to $x/R = 16$ in uniform flow	Sedaghatizadeh et al., (2019)
5. Vortex Shading Frequency	
Shedding frequency near the tip region is about ~60-80 Hz compared to ~4-10 Hz close to hub at $x/D = 1$. This is considered as low frequency shedding (< 100 Hz) with $St \approx 0.35$. Frequency response is found to be consistent at $x/D = 0.5$, *1* and *2*	Zhang et al., (2013)
Streamwise velocity produces low frequency (~10 Hz). The shedding frequency depends on *x/D*, inlet TI and ABL	Aubrun et al., (2013)
When $4 < x/R < 5$, high frequency signatures are noted, indicating the onset of instabilities with vortex pairing	Carrión et al., (2015)
St is found to be decreasing with increase of λ, however, it increases with γ	Medici, D., and Alfredsson, (2008), (2006)
Shedding frequency and helical tip vortex frequency responses vary with change in blade pitch angle.	--
6. Yaw Effect	
In an array of rotors, the C_{Pmax} of downstream rotor increases by about 12% under yaw (γ)	McKay et al., (2013).

At $\gamma = 0°$, the vortex size increases due to continuous vorticity feeding from the entire blade span. Moreover, a constant vortex circulation is obtained, which is independent of azimuth angle. At $\gamma \neq 0°$, the overall vortex size is smaller compared to $\gamma = 0°$	Grant and Parkin, (2000)
The wake deflection under yaw condition produces wake skew that lasts till far-wake regime. At this condition, the progress of vortex dissipation is further enhanced resulting in an early velocity recovery	Uemura et al., (2017)
Yaw control in manoeuvring the wake meandering is found to be highly interactive with the η_{WF}	Castellani et al., (2018)
7. **Tip Speed Ratio Effect**	
Axisymmetric distribution is noted at high λ (= 10)	Eriksen and Krogstad, (2013)
Lateral and vertical deficits also increase with increase of λ	Li et al., (2017).
At high λ (>11), the rotor wake starts losing its helical stability from near to far wakes	Okulov et al., (2017); Troldborg et al., (2012)
Wake size increases with increase of λ	Talavera and Shu, (2017)
Upon increasing the λ from 2.5 to 7, the flow recovery distance drops to *6.5D* from *14.5D*	Hasan et al., (2019)
8. **Inlet Turbulence Intensity Effect**	
High inlet TI leads to relatively higher wind velocity distribution, causing an entrainment of inflow and wake	Li et al., (2017).
Performance and wake characteristics are found to be highly dependent on the inlet TI	Talavera and Shu, (2017).
There is not much significant change in the recovery distance upon increasing the U_∞	Hasan et al., (2019)
9. **Atmospheric Boundary Layer Effect**	
Wake growth is the largest for the stable ABL compared to unstable ABL. Streamwise velocity (U_x) recovers much faster (0.75 U_∞) in unstable compare to stable ABL (0.6 U_∞) at $x/R = 10$	Hancock et al., (2014).
There is an increase of inflow velocity by 13% at the hub height for hilly surface compared to plain surface	Hyvärinen and Segalini, (2017).
Consistent and stronger vortex ring is observed till $x/D < 4$ under stable boundary layer	Sedaghatizadeh et al., (2019)
10. **Others**	
Effects from turbine tower and nacelle are found diminishing beyond $x/D = 2.5$	Kocer et al., (2011)
The downstream rotor losses its power by about 50-60%, and an improper alignment could lead to 10-20% loss in the annual energy production	Barthelmie et al., (2010), (2007).
Downstream rotor shows C_p = 0.12, 0.13, and 0.15, when installed at x/R = *6*, *8*, and *10*, respectively.	--
A simple relationship can be obtained between the decay law of the velocity deficit and the *Cp* of the downstream rotor	Troldborg et al., (2010)

2.4.5 Summary of Wake Literature

Research has identified several essential factors influencing wake behavior, prompting the need to move beyond simplified models and incorporate more physically realistic dynamics. These factors include wake regions, vortex dynamics, tip-speed ratio, yaw effects, inlet turbulence intensity, atmospheric boundary layer characteristics, and turbine design parameters. Each plays a unique role in shaping the structure, strength, and recovery of turbine wakes.

- One of the fundamental insights from wake studies is the distinction between the near and far wake regions. The near wake of a rotor is marked by high shear, strong rotational flow, tip vortex formation, and asymmetric turbulence. Although individual blade effects diminish after *1D*, tip vortices can extend up to *5D* downstream.
- The far wake region beyond approximately *4D* downstream marks a transition toward flow recovery and greater mixing with the freestream. The velocity deficit in a turbine wake diminishes due to turbulent diffusion and environmental influences, but this recovery varies based on factors like the λ. Higher λ values increase the wake diameter and turbulence, leading to faster velocity recovery.
- Turbines operating under yawed conditions generate deflected or skewed wakes. These wakes can be strategically directed away from downstream turbines, thereby increasing the power output of those machines. Yaw-induced deflection enhances wake mixing and shortens recovery distances, leading to performance gains for downstream turbines.
- Higher turbulence at the inlet leads to more rapid entrainment of ambient air into the wake, enhancing diffusion and accelerating recovery. TI substantially influences wake shape, velocity deficit, and downstream turbine performance.
- A stable ABL suppresses turbulence, resulting in slower wake recovery and more pronounced velocity deficits downstream. In contrast, an unstable ABL promotes vigorous mixing and faster re-establishment of freestream conditions.
- Vortex dynamics particularly tip vortices' formation, evolution, and shedding frequency are also central to wake studies. The wake behind a rotating blade comprises helical tip vortices, which can persist for several rotor diameters before breaking down.

Finally, the importance of high-fidelity modelling methods has become increasingly clear. While traditional analytical models provide useful approximations, they often oversimplify physical phenomena by neglecting key effects like pressure gradients, rotational flow, and shear layer interactions. Modern approaches such as CFD, machine learning-based surrogate models, and experimental validation are essential for capturing the true nature of wake dynamics.

2.5 Research Gaps and Present Objective

Due to the majority of current wind turbine research being devoted to giant utility-scale turbines, there is a substantial knowledge gap regarding small HAWTs and MRSs with low *Re*. The laminar-turbulent transition, strong tip-vortex coherence, and unstable loading typical of low *Re* operation are not capture by the majority of wake models currently in use, which are based on high *Re* assumptions. Even though small HAWTs are becoming more and more relevant for distributed and off-grid applications, there is a dearth of experimental and field data on their wake behaviour when operating at low λ circumstances. Additionally, although MRSs have been investigated conceptually to improve land-use efficiency and power output, controlled experimental research has not yet adequately verified them. Insufficient empirical data for small HAWTs and MRS under practical operating conditions hinders the creation of precise models and efficient designs for these systems. Additionally, the combined effects of operating λ, rotor spacing, and Re on wake symmetry and recovery have not been determined within a cohesive experimental framework.

Through a series of experimental investigations, the present study attempts to improve the understanding of wake behaviour in small HAWTs and MRS. Tapered blades based on the SG6043 airfoil have been fabricated to form the turbine systems and then to evaluate their aerodynamic performances in a wind tunnel. In summary, the following objectives are attempted:

(a) Blade Development - Fabrication of tapered and un-tapered blades with airfoil **SG6043**
(b) Wind Turbine Wake Study - Velocity in stream-wise as well as span-wise have been measured using HWA
(c) Characterize Wake in Single and Double Rotor Systems - To Investigate and compare the wake behavior in these systems
(d) Near Wake Studies - To measure wake development at multiple downstream locations, specially $x/R = 1, 2, 3,$ and 4
(e) Wake Interaction under Low TSR - To analyze wake interactions under low λ conditions relevant to Small HAWTs and MRS
(f) Effects of Tip Spacing on Wake Strength and Recovery - To study the impact of rotor $T_S = 0.5R$ and $1.0R$ on wake strength and recovery

2.6 Overall Summary

This chapter established the theoretical foundation and contextual framework for this study. It outlined wind turbine aerodynamics, covering forces on blades, airfoil geometry, and performance principles, focusing on small HAWTs. Specific considerations for small HAWTs included blade design, airfoil selection, and performance challenges at low *Re*. The literature review examined the experimental and the numerical research on SWT, MRS, and wake dynamics, detailing the effects of rotor spacing, tip vortices, and wake interaction. Finally, the chapter defined the research objective by addressing gaps in existing studies, particularly concerning near-wake behaviour in single- and double-rotor HAWTs at low TSR conditions, which aims to provide new insight into wake interaction, recovery, and spacing effects in SWT and MRS.

CHAPTER 3

EXPERIMENTAL SETUP AND METHODOLOGY

3.1 Introductory Remark

In this chapter, the research investigations are focused on the experimental setup and working methodology to execute the aim with step-by-step processes. The primary aim of the experiment is required to make a setup, which has a model, measuring instrument, and ambient/ other conditions. The methodology is followed to measure the parameters of the experimental aim. For the wind turbine wake studies, some parameters like velocity deficit, frequency response, vortex shedding, and turbulence intensity are required to analyse the behaviour or characteristic of the wake. These parameters are calculated with help of velocity/ voltage. The experimental strategy employed to investigate the wake dynamics of small HAWTs, both in isolated (single-rotor) and coupled (multi-rotor) arrangements. The aerodynamic behaviour of small HAWTs, especially at low *Re* and λ, significantly differs from that of LWTs.

3.2 Experimental Facility

3.2.1 Wind Tunnel

An open-circuit subsonic wind tunnel at the Indian Institute of Technology Guwahati, India, was used for the experimental investigations. Figure 3.1 depicts the tunnel's schematic layout, while Table 3.1 (Siram and Sahoo, 2019; Siram et al., 2023) summarises the facility's main specifications. This wind tunnel is ideal for aerodynamic research including wake characterisation of SWTs since it is specifically made to create a consistent and uniform airflow in the test area. A 30-hp, three-phase induction motor powers an axial fan in the wind tunnel's test section, which runs on the open-circuit principle and can generate wind speeds of up to 50 m/s. The actual test section dimensions 2000 mm in length, 600 mm in width, and 600 mm in height. With a calibrated velocity range of 3–12 m/s and a free-stream velocity variation of less than ±1%, the flow inside the test section stays extremely uniform.

The wind tunnel has a well-designed flow conditioning system to provide a low-turbulence environment. The TI, measured using a constant-temperature HWA, is less than 0.3%, with consistent values across the test section and velocity range. The tunnel's suitability for sensitive aerodynamic measurements was confirmed by calculating TI using the RMS value of velocity fluctuations.

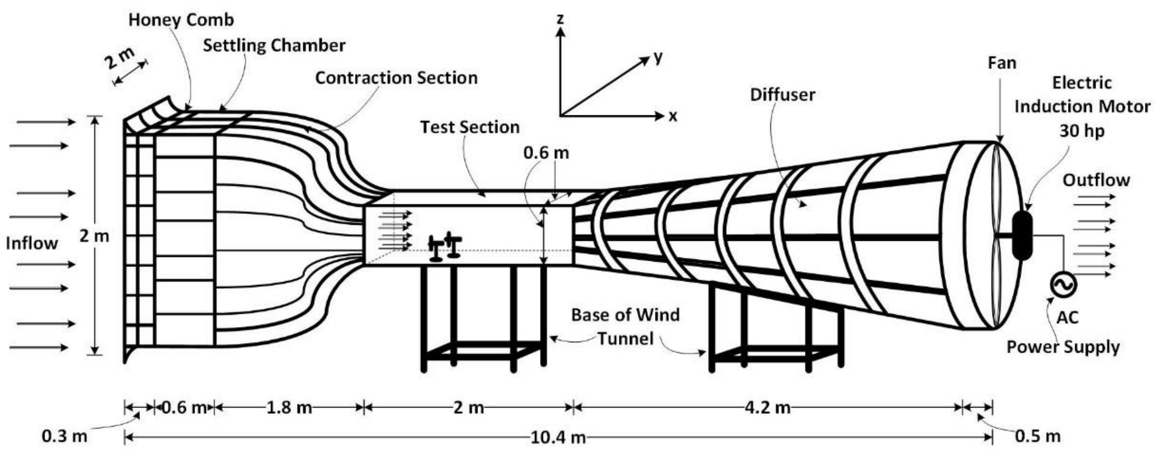

Fig. 3.1 Schematic diagram of wind tunnel facility

Table 3.1 Wind tunnel specifications

Parameters	***Description***
Type	Open Circuit
Test section	(2000 mm) x (600 mm) x (600 mm)
Contraction ratio	6:1
Maximum velocity	50 m/s
Motor power	30 hp
Turbulence intensity	0.3%

3.2.2 Electronic Manometer and Pitot Tube

The electronic manometer is a device which measures wind speeds, velocity on models, and low-pressure differences as shown in Fig. 3.2. The range of the pressure transducer used is 0 mm to 210 mm of water. This instrument is specially designed for accurate measurements of wind speeds inside a wind tunnel. Pitot-tube connected to pressure leads of electronic manometer through a pipe, has two pressure leads at the top attached to a Pitot-static tube's static and dynamic ports, as seen (Fig 3.2 (a)), which produces pressure difference. Real-time data of pressure, calculated velocity, and system status are shown on the centre LCD panel. Start/stop measurements and menu settings are navigated via a keyboard interface with four membrane buttons. Before each measurement session, the baseline pressure is calibrated and reset using a zero-adjustment potentiometer. During zero adjustment mode, the voltage should be in the range of 11 mV to 13 mV.

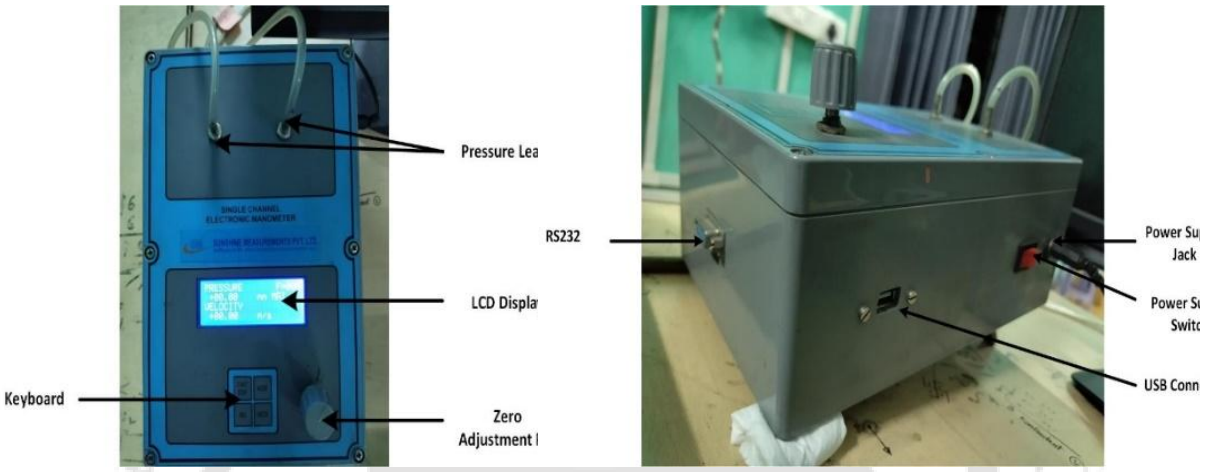

(a) (b)

Fig. 3.2 Electronic Manometer (a) Top view, (b) Side view

Figure 3.2 (b) shows that serial data transmission with external computers or data collecting devices is made possible by the RS232 port. One may update the firmware or add more logging support via a USB cable. This manometer is ideal for laboratory-scale aerodynamic investigations using small-scale wind turbines or flow configurations because of its tiny size, interface ports, and real-time display. The unit's high sampling precision (100 Hz) guarantees accurate velocity readings when paired with a calibrated Pitot-static tube.

3.2.3 Proxy Sensor

An n-p-n type proximity sensor with a sensing distance of 10 mm and an accuracy of ±0.1% is used to measure the turbine rotor’s rpm. These sensors operate based on the principle of electromagnetic induction, where an internal oscillator generates a high-frequency electromagnetic field at the sensor face as shown in Fig 3.3. When a metallic object, such as a rotor blade or attached marker, enters this field, eddy currents are induced in the metal, which in turn reduce the amplitude of the oscillations. When the flow is consistent, the proximity sensor displays an accuracy of ±0.1% and a divergence of about ±0.3% from the torque sensor RPM data (Siram and Sahoo, 2022).

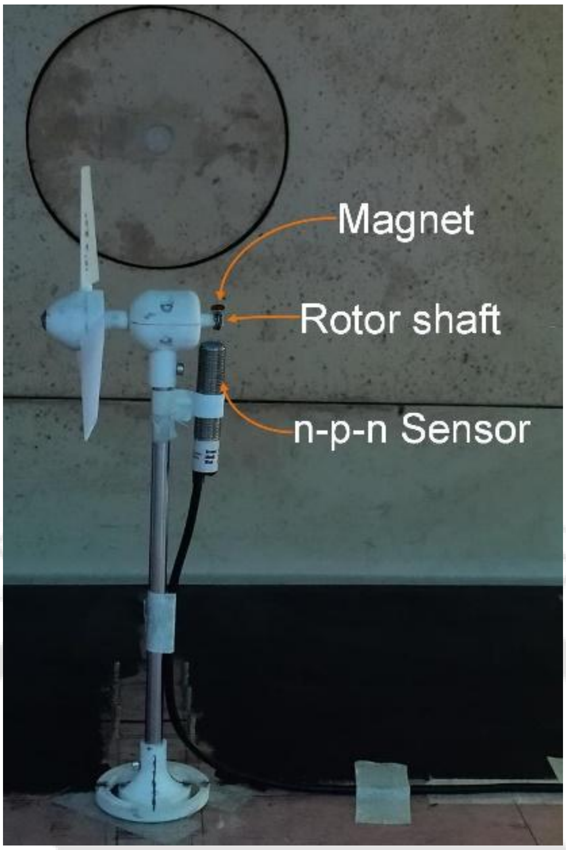

Fig 3.3 Arrangement of n-p-n type proximity sensor

However, several factors, including missed pulses at high rotational speeds, false triggers from ambient electromagnetic interference (EMI), vibrations, or uneven target alignment, can result in measurement errors. If the sensor’s response time is insufficient at higher RPMs, it may fail to register all pulses, resulting in undercounting. On the other hand, overcounting and consequently inflated RPM values can result from false triggering. The proximity sensor’s RPM measurement variation is predicted to be around ±0.5% depending on mounting precision and signal processing. The pitot-static tube setup’s typical standard deviation for wind flow velocity is roughly 1.2% (Siram et al., 2022).

3.2.4 Hot-Wire Anemometry

A constant-temperature HWA is used to investigate the turbulence level in the wind tunnel flow and the wake generated by wind turbine. It is informed from the fundamental ideas of the Whitestone bridge electric circuit and convective heat transfer mechanism. According to Ohm's law, the operating voltage adjusts continuously to maintain the probe wire at a constant temperature, while the voltage fluctuations provide a direct measure of the velocity fluctuations. The background turbulence intensity of the wind tunnel was measured using HWA and found to be less than 0.3% for all test conditions.

Fig. 3.4 Constant Temperature Hot-Wire Anemometry System

For measurement of fluctuating velocity and frequency response, a constant-temperature HWA is integrated (Fig. 3.4). The HWA probe is made of 10 μm diameter tungsten wire with platinum coating and an effective sensing length of 3 mm (Fig. 3.5). A traverse system is used to translate the hot-wire probe at multiple locations downstream and in a lateral direction to examine the velocity deficit, turbulence intensity, vortex shedding frequency and wake deflection, as illustrated in Fig. 3.6.

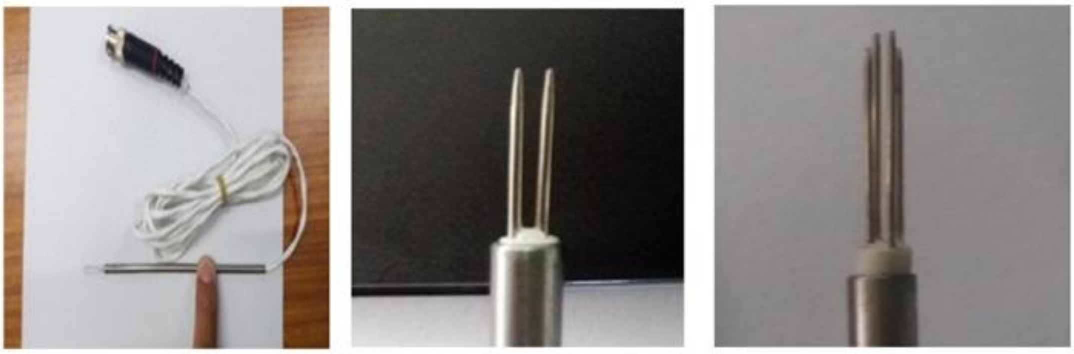

Fig. 3.5 Hot-Wire Probe

Based on findings from the literature, the velocity power index is set at 0.5 for air, the working fluid, and speeds between 3 and 20 m/s (low *Re*) (Bishop and Yarusevych, 2011; Siddal and Davies, 1972). A constant-temperature anemometer (CTA) probe was selected for this work because of its user-friendliness and comparatively better reaction at moderate wind flow rates (Simpson et al., 1979). Uniform heat transfer is ensured by positioning the hot wire such that its axis is perpendicular to the direction of the mean flow. Alignment is important because a single wire CTA probe that is aligned well responds to fluid flow with little deviation

(Yavuzkurt, 1984), which effectively governs the HWA operating principle. Usually, the cylindrical sensor is soldered or welded to stainless steel prongs, which are then connected to a Wheatstone bridge via which the resistance of the sensor serves as one of its variable resistance units (see Fig. 3.7). The Wheatstone bridge's varied resistance serves as a counterweight for the variation in heat transmission that results from the wire.

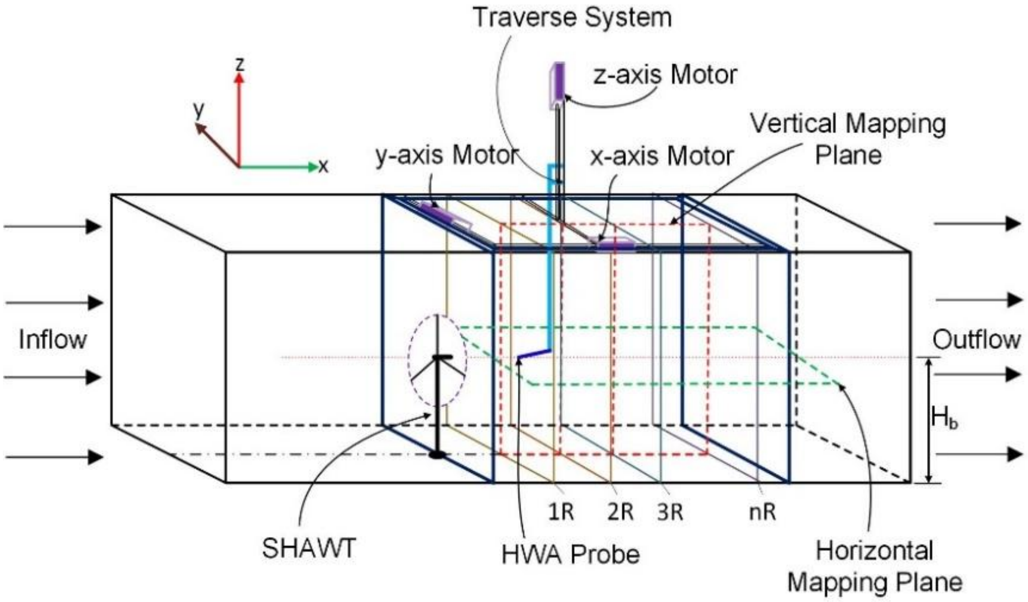

Fig. 3.6 Schematic representation of HWA measurement with traverse system

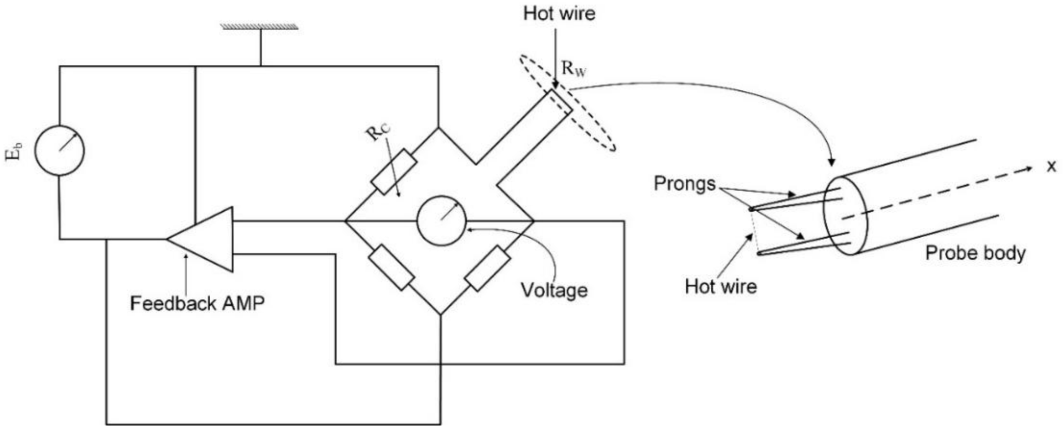

Fig. 3.7 Schematic diagram of hot-wire anemometer circuit

Single-wire HWA is known to have intrinsic limitations in complex three-dimensional wake flows, particularly in regions with high shear and vortex activity. Where there are substantial transverse velocity components, directional ambiguity occurs because the probe only measures the velocity component aligned with the wire. Additionally, the finite wire length causes steep velocity gradients to be spatially averaged, and the CTA system's finite frequency response may reduce high-frequency turbulence linked to small-scale vortices. Additional uncertainty may be introduced by the probe's local flow disruption and temperature sensitivity.

To mitigate these effects, the spatial traverse resolution was chosen to balance gradient resolution with signal stability, and probe alignment was carefully maintained with respect to the local mean flow whenever feasible. To confirm the linearity and frequency responsiveness of the CTA, regular static and dynamic calibrations were performed against a reference Pitot manometer system. Spectral interpretation was conducted cautiously, considering the confirmed bandwidth of the measuring system. To ensure the validity of the results, mean wake trends were further cross-validated whenever appropriate using integral wake measurements, such as the area-integrated velocity deficit.

The carefully calibrated single-wire HWA used in this study is sufficient to resolve normalised velocity deficits, turbulence intensity trends, and wake recovery behaviour with acceptable accuracy. However, multi-component velocity measurements using X-wire probes, and PIV would provide improved resolution of vortex cores and shear-layer dynamics. As a result, both data interpretation and reported results explicitly consider the method's limits and related uncertainties.

3.2.5 Data Acquisition System

Data collecting and analysis is a big task for researchers, which requires more time. A data acquisition system is required to minimize the time and smooth run of the experiment. The acquisition of various analogue signals is possible by NI DAQ-6363 and with a user-friendly virtual interface LabVIEW program. NI DAQ-6363 has 32 single-ended analogue input channels or 16 differential channels. Input sample rates are 2 M/s and 1 M/s for single and multiple channels respectively. LabVIEW is a graphical programming language, which is used to develop automated research, validation, and production test systems.

All the measurements were taken with respect to the rotor plane of the turbine and observation has been made within the near wake regime. Figure 3.4 represents the overall layout of experimental procedures adopted. The analogue voltage signal from the hot-wire component is taken through NI DAQ-6363 USB keeping the sampling rate at 10 kHz. The sampling time for data acquisition has been maintained sufficiently large compared to time scale of small eddy formation. This time scale defines the time required for eddy to pass a given point. In order to interpret the analog voltage signal into a useful parameter, the LabVIEW based program has been prepared and fourth-order Butterworth filter is assigned to remove unwanted noises from the signal. The Fourier transform based power spectral density (PSD) analysis is performed on the varying filtered signal from instantaneous corresponding velocity signal to interpret the frequency response of vortex shedding. The transformation has been performed on the evenly spaced acquired signal from acquisition system.

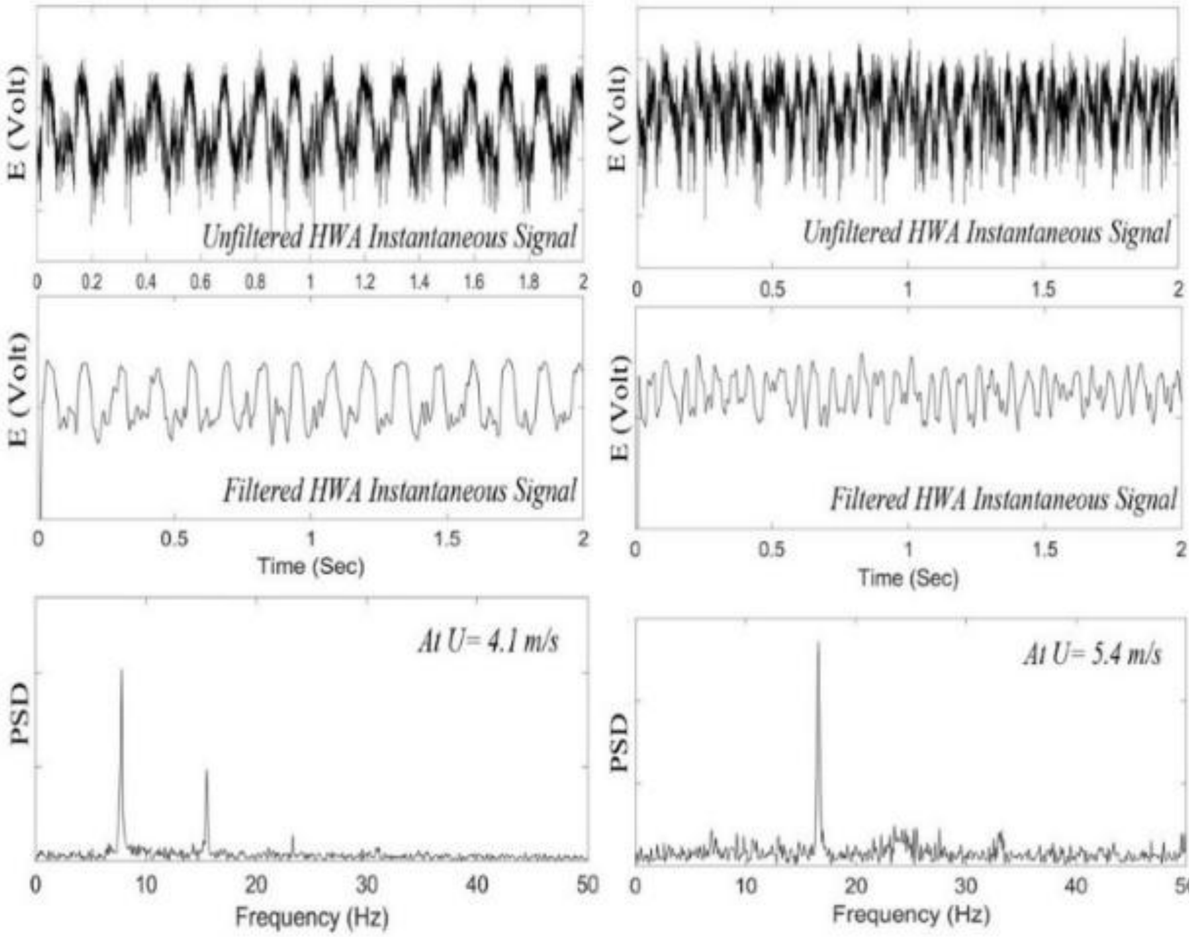

Fig. 3.8 Typical voltage signal and its corresponding power spectral density (PSD) from HWA measurement

The computed Fourier transformation estimated correction is such that it is within the range of windowed estimate filtering applied prior to transformation through Nyquist criteria. In this way, it gives a good estimation of power spectrum for required frequency range (<100 Hz) of vortex shedding. A typical time signal response comparison between raw unfiltered voltage signal and filtered signal with its corresponding power spectral density has been shown in Fig. 3.8. Phase-Locked averaged (PLA) method has been employed by simultaneous voltage signal acquired from HWA and RPM pulses from turbine shaft. For this purpose, a proximity sensor is located in the vicinity closer to the rotor shaft. As the turbine blade passes, the synchronic electromagnetic pulse generated by proximity sensor is used as reference and the resulting summation of pulse signal and HWA voltage signal is termed as PLA.

3.2.6 Uncertainty Analysis of Experimental Measurements

To assess the correctness and reliability of the experimental measurements presented in this paper, a thorough uncertainty analysis was conducted. Hot-wire calibration error, probe placement precision, electronic signal noise, temperature drift, and data acquisition resolution are some of the factors contributing to the overall uncertainty in the wake velocity measurements. The overall measurement uncertainty was estimated by methodically evaluating and propagating these individual contributions.

The hot-wire calibrating procedure is the primary source of uncertainty. Within the operational velocity range of 2.5–10 m/s, repeated calibrations against a reference Pitot-static system produced a maximum velocity uncertainty of ±2.0%. The Pitot-static system itself exhibited a standard deviation within acceptable tolerance limits, and the HWA voltage-velocity calibration showed excellent linearity with an R^2 value close to unity.

The positional uncertainty of the traversing mechanism was ±0.2 mm in both streamwise and lateral directions. which contributes to uncertainty when sampling steep velocity gradients in the near-wake and shear-layer regions, but introduces a minimal error in mean velocity estimation.

Shielded cables, appropriate grounding, and ensemble averaging reduced electronic noise and signal conditioning mistakes. A fluctuation uncertainty of less than ±0.5% of the observed root-mean-square (RMS) velocity signal was produced by the data acquisition system's voltage resolution. The hot-wire response's temperature-induced drift was reduced to within ±1% by regular zero-offset checks and recalibration.

A root-sum-square (RSS) approach was employed to determine the combined uncertainty in the instantaneous velocity measurement, yielding an overall velocity uncertainty of approximately ±2.5–3.0% under normal operating conditions. Due to the susceptibility of RMS velocity variations to electronic noise and frequency response constraints, the turbulence intensity uncertainty was calculated to be within ±3.5-4%.

Standard error propagation techniques were used to propagate uncertainty for derived wake metrics such as normalised velocity deficit and area-integrated velocity deficit. Even in areas of high wake interaction, the uncertainty in velocity deficit was within ±3.5–4.5%., whereas the uncertainty in the area-integrated velocity deficit stayed below ±5.5%

Additionally, it is acknowledged that the single-wire HWA system may underestimate the local velocity magnitude within vortex cores and introduce directional ambiguity in areas with significant transverse velocity components. However, these errors do not alter the primary physical conclusions, as the current work is primarily concerned with normalised wake trends, recovery behaviour, and spacing-dependent wake interactions, rather than absolute three-component velocity vectors.

To maintain the statistical significance and experimental robustness of the observed wake interaction, turbulence generation, and recovery features, the uncertainty bounds are explicitly considered in all quantitative comparisons and trend analyses presented in Chapters 4 to 6.

3.3 Rotor Design and Configuration

After thoroughly reviewing the literature, the SG6043 airfoil is selected to design the blades for the small HAWT and the MRS which performs well aerodynamically at low *Re* order of 10^5 (Giguere and Selig, 1998). Each airfoil features a geometric profile defined by a set of coordinates one along the chord line and another perpendicular forming the blade's cross-sectional shape. These coordinates are obtained from the airfoil tools database and used them to generate the blade profiles. The cross-section is extruded along the axial direction to create the three-dimensional blade geometry. Depending on the design requirements, a simple straight extrusion is applied to achieve a tapered blade configuration. At any point along the blade's span, the blade has a SG6043 sectional profile (Fig. 3. 9a), and the corresponding geometric parameters are shown in Fig. 3.9(b).

The rotor is designed to operate at low *Re* (0.6×10^4 to 1.4×10^4) and low λ (2.5 to 3) values to ensure optimal performance under small-scale wind energy conditions, this model has been categorized as a small HAWT (Siram et al., 2022; Keisar et al., 2020; Mohammed et al., 2019). Low turbulence wind tunnels typically have λ values between 3 and 15 (Fuglsang et al., 2004; Butterfield et al., 1992), classifying the current model turbine rotors as low λ. Table 3.2 contains the geometric specifications of the rotors.

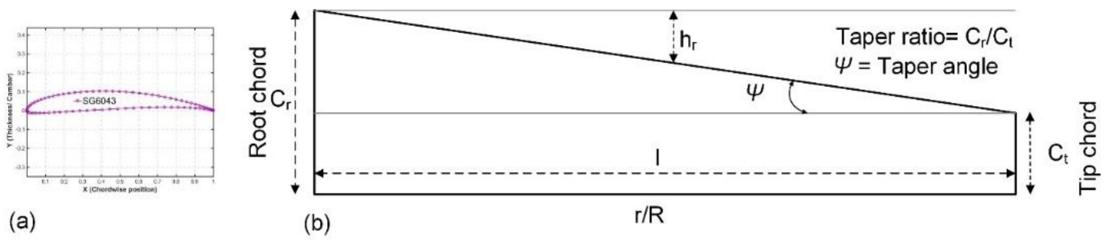

Fig. 3.9 (a) Sectional profile (SG6043) of HAWT blade; (b) Geometric parameters of straight blade

Table 3.2 Geometric specifications of the small HAWT rotor

Parameters	***Designation***
Rotor profile	SG6043
Rotor radius, R	65 mm
Hub height, H_b	215 mm
Number of blades, B	3
Maximum rpm	~2500 rpm at 5.53 m/s
Design process	Straight and tapered
Operational λ	2.5 – 3
Blockage Factor, BF	3.65% (Single rotor) 7.3% (Double rotor)
Fabrication method	FDM 3D printer
Material	PLA
Infill density	40%

Using SOLIDWORKS software, all three main components are modelled for the rotor blades, hub, and nacelle to match the design specifications. These all parts are fabricated using FDM 3D printing technology. The 3D printer has a large working area of (305 mm) x (305 mm) x (605 mm) and is equipped with a double extruder. The printing process necessitates a nozzle temperature ranging from 210° to 235°C and a bed temperature between 60° and 70°C. All these parts are printed with polylactic acid (PLA) material which is biodegradable and eco-friendly. Fig. 3.10 illustrates the steps required for fabrication. Notably, in the third step (Fig. 3.10), the IdeaMaker tool, a slicing software, transforms the computer-aided 3D model into a design ready for printing. The rotor achieves a maximum speed of approximately 2500 rpm at an inflow velocity of 5.53 m/s with infill density 40%. The vital printing parameters are listed in Table 3.3 with their purpose and range.

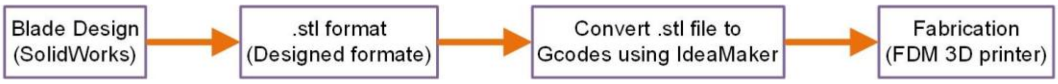

Fig. 3.10 Blade fabrication procedure

Table 3.3 Vital printing parameters

Parameters	Purpose	Range
Layer height	Surface finish	0.08-0.12 mm
Infill ratio	Stiffness	60-80 %
No. of shells	Strength	-----
First shell speed	Surface finish	20-25 mm/s
Infill ratio of support	-----	12-15 %
Platform support	Avoids detachment from printing bed	-----

The turbine hub is firmly fastened to these blades before being mounted inside the wind tunnel using a base frame. The sectional chord length (C_r), sectional taper height (h_r), and sectional solidity (σ_r) of the model turbines were calculated using mathematical equations 3.1 through 3.5. These values were determined at sectional radial intervals of 0.02 (*r/R*).

The variation of sectional chord length along *r/R* shown in Fig. 3.11(a), while Fig. 3.11(b) illustrates the change in sectional taper height along *r/R*. Additionally, Fig. 3.11(c) displays the solidity of the turbine, which represents the ratio of the blade area to the rotor's swept area. It is evident from Fig. 3.11(c) that the solidity is highest near the root of the blade and decreases towards the tip.

It is to be mentioned that a higher solidity results in a more significant blockage factor (Schubel and Crossley, 2012; Duquette and Visser, 2003). The effect of λ on wake generation behind the rotor has been investigated in this study. The parametric assessment has been made with reference to centre line of the wind tunnel. The scaling parameters such as (i) stream wise direction (*x/R*), (ii) span-wise directions (*y/R*), (iii) hub heights (H_b), and (iv) vertical directions (*z/R*) have been taken with respect to the rotor plane and central axis of the wind tunnel.

$$\tan\psi = (C_r - C_t)/l\ ;\ Or,\ \psi = \tan^{-1}[(C_r - C_t)/l] \tag{3.1}$$

$$C_r(r/R) = C_r(root) - h_r(r/R) \tag{3.2}$$

$$\text{Also,}\ \tan\psi = h_r / r \tag{3.3}$$

$$h_r\big|_{r/R} = (r/R)R\tan\psi\ ;\ Or\ \ h_r\big|_{\mu} = (\mu)R\tan\psi;\ \mu = r/R \tag{3.4}$$

$$\sigma_r = (N_B C_r / 2\pi r) = (N_B C_r / 2\pi\mu R) \tag{3.5}$$

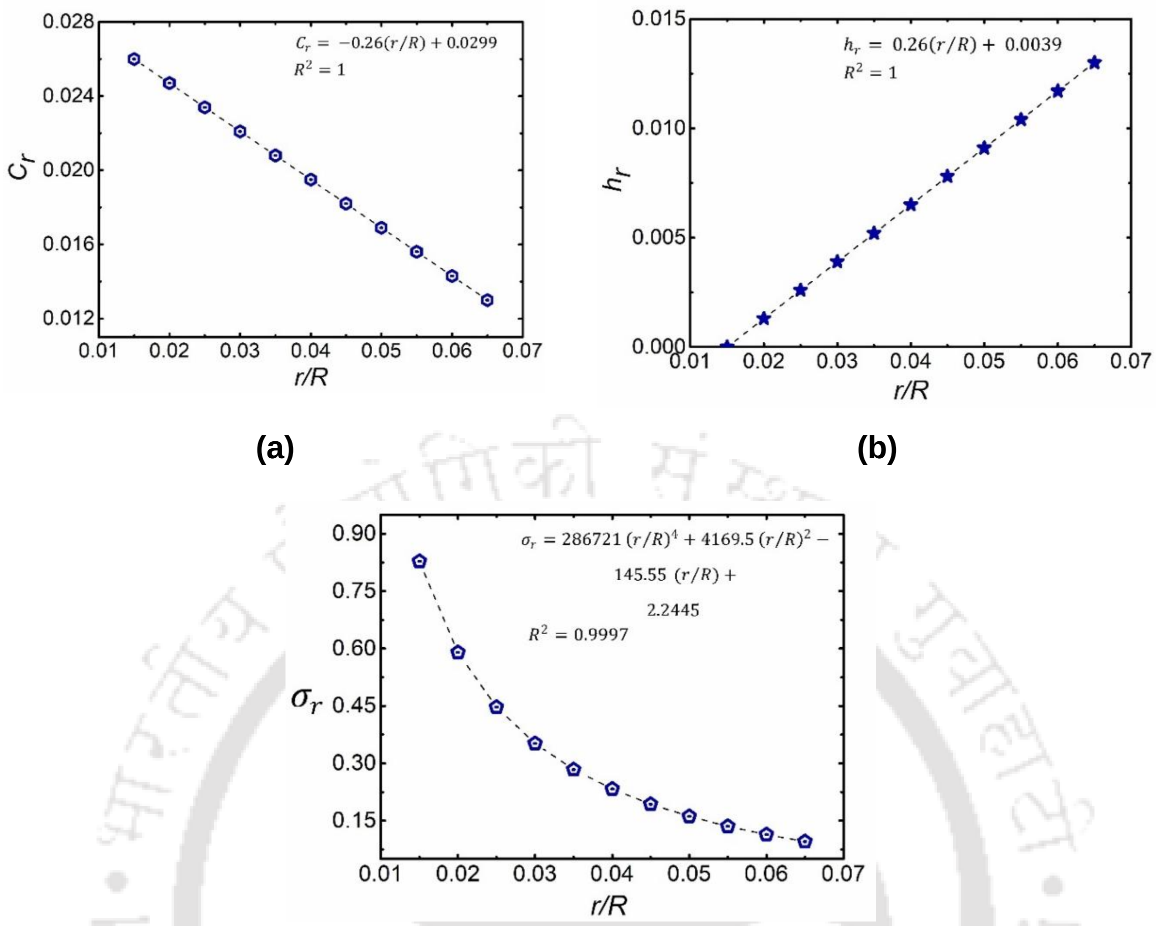

(a) **(b)**

(c)

Fig. 3.11 Variation of (a) sectional cord length (C_r) with *r/R*, (b) Blade taper height, and (c) Variation for sectional solidity (σ_r) with *r/R*

3.4 Measurement Strategy and Methodology

The model rotors placed inside the wind tunnel test section consists of small HAWT (Fig. 3.12). The velocity sensor used in the study is a constant temperature HWA. The flow field mapping is the key aspect of the present study which is done in the horizontal and vertical planes for different downstream location for single- and double-rotor configurations. The parametric assessment has been made with reference to centre line of the wind tunnel. The scaling parameters such as (i) stream wise direction (*x/R*), (ii) span-wise/horizontal directions (*y/R*), (iii) hub heights (H_b), and (iv) vertical directions (*z/R*) have been taken with respect to the rotor plane and central axis of the wind tunnel. For both *y/R* and *z/R* wake mapping, the coordinate origin (*y/R* = 0, *z/R* = 0) was taken at the centre of rotor (single-rotor) and midpoint between the two rotor hubs (double-rotor) at H_b. Figure 3.12(a) represents the model rotor arranged with reference to the tunnel test section. The setup of the experimental instruments, along with the data acquisition and processing layout, can be observed in Fig. 3.12(b).

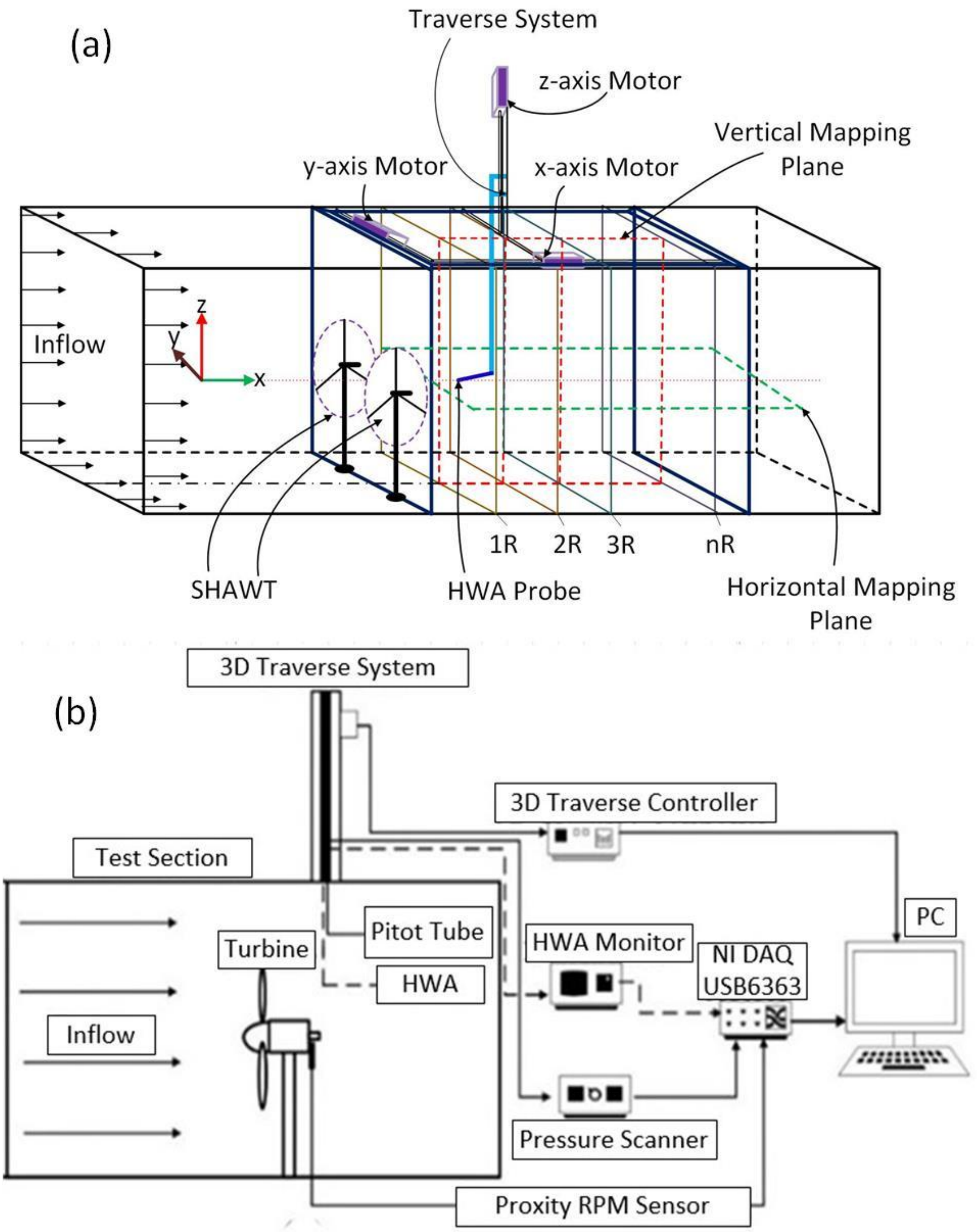

Fig. 3.12 (a) Schematic diagram of test section; (b) Data acquisition system of the setup

The span wise or side by side placement of rotor is to determine the wake characteristics along span wise direction because the interaction will be different from the stream wise placement. The rotor is placed along the tunnel's centre line, with variable distances between its blade tip and the sidewall. The side wall clearance from the blade tip is about 235 mm for a single rotor, and 153.75 mm and 137.5 mm for a double rotor with tip spacing (T_S) = *0.5R* and *1.0R* respectively. It indicates the distance between the tips of two rotors along the spanwise direction. In the present study, the issue of blockage has also been carefully navigated and the effect has been minimized by reducing the rotor diameter. At the same time, it is ensured that the rotor operate at the desired low λ condition.

The radius of the rotor (R) is 65 mm. Accordingly, for a single-rotor and a double-rotor, the blockage factors (BFs) are found to be around 3.65% and 7.3% respectively, which are within the acceptable bounds, and this negates the need for blockage corrections (Van Treuren, 2015; Werle, 2010). Most of the reported studies related to wake propagation are focused on LWTs of higher λ (> 10) (Elkodama et al., 2022; van der Laan et al., 2019; Kale and Sapali, 2013; Jameson and Branney, 2012; Vermeer et al., 2003; Frandsen, 1992; Magnusson and Smedman, 1999). In the present investigation, multiple experiments were conducted to ensure minimal errors.

The intended range of Re and λ for SWT are 0.6×10^4 - 1.4×10^4 and $2.5 < \lambda < 3$, for $D = 130$ mm, however, in most of the studies, the rotor diameter is kept much smaller. This is to overcome the blockage issue (Van Treuren, 2015; Burdett and Van, 2012). In such cases, although the C_p obtained may be promising, the instantaneous power acquired is minimal. The same rotor can therefore be analysed and tested in the scaled-up configuration to obtain the useful power. The scaling relations of wind turbines have already been reported by Van Treuren, (2015) and Burdett and Van, (2012).

To measure the rotor's rotational speed, an RPM proximity sensor that can save data up to 9999 times was used to calculate the rotational frequency. Under the no-load condition, the model rotor can rotate at a maximum speed of about 2500 rpm, when the wind speed is 5.73 m/s. An electronic manometer is employed to acquire the wind velocity within the tunnel, with a static pitot tube connected to a pressure sensor. The voltage difference obtained is then calibrated with respected to the velocity changes in the tunnel. The electronic manometer operates at a sampling frequency of 100 samples/sec, with a sample duration of 10 seconds.

The calibration of wind flow inside the working section shows that there is a linear correlation between the speed (U_∞) and the tunnel fan RPM, the result of which has been illustrated in Fig. 3.13(a). The upstream velocity measured using this electronic manometer is utilized to calibrate the HWA. A velocity range of 2.5–6.5 m/s is chosen for the calibration process. The respective standard deviation of velocity response of the pressure probe is found to be within the limit of acceptable tolerance, as shown in Fig. 3.13(b). The HWA probe selected for this investigation is a constant temperature type, and it has a 10 μm diameter tungsten platinum-coated wire capable of withstanding velocities exceeding 20 m/s. The NI USB6363 DAQ has been used for signal acquisition, and the signal processing has been performed with the help of a LabVIEW program. To ascertain a minimal deviation in the reading, the HWA probe has been calibrated before and after the experiments. The response of the hot-wire voltage to the freestream velocity, as measured during the method of calibration, is shown in Fig. 3.13(c). Figure 3.13(d) shows the resulting calibration curve for the HWA and King's law expresses the correlation between the HWA output voltage and the freestream velocity, and it is stated below,

$$E^2 = A + B\sqrt{U_\infty} \tag{3.6}$$

where the E is the output voltage, U_∞ is the freestream velocity, and A and B are calibration constants.

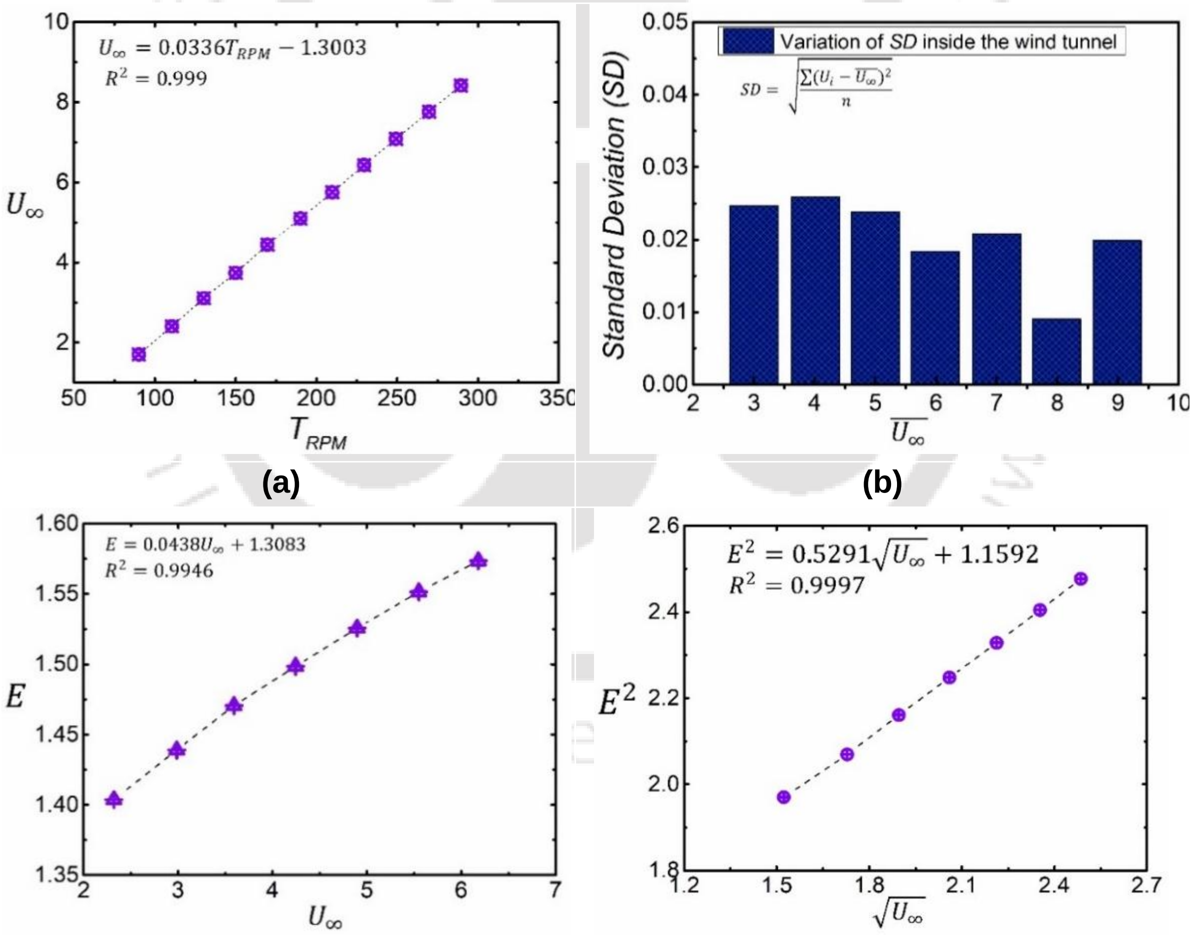

(a) **(b)**

(c) **(d)**

Fig. 3.13 (a) Tunnel RPM and freestream velocity, (b) Standard deviation in pitot-static probe velocity response, (c) HWA response, and (d) HWA King's law linearity curve

Further, the characteristics of the tunnel is expressed in terms of the turbulent intensity (TI), which is found to be about 0.3%. This value of TI is good enough to conduct the fundamental studies with minimal errors and this would yield the valuable data for comparison and validation. The influence of *Re* on small HAWT, however, is minimal for speeds below 6 m/s (Khorsand et al., 2018; Khan et al., 2017).

3.4.1 Normalised Velocity Deficit Calculation

The wake velocity deficit (U^*) is quantified in terms of the normalised velocity deficit where U_d represents the absolute velocity reduction in the wake compared to the U_∞ . This is computed at each measurement location by Eqn. (3.7) (Van Treuren, 2015), and it describes the deficit of downstream local velocity (*U*).

$$U^* = (U_\infty - U)/U_\infty = \Delta U/U_\infty = U_d/U_\infty \tag{3.7}$$

where:

U = local velocity at a given point (x, y, z) in the wake

$\Delta U = U_\infty - U$ = local velocity reduction relative to the freestream

U_d = velocity deficit magnitude

3.4.2 Area-Integrated Velocity Deficit

While the pointwise deficit reveals local flow features, it does not provide a measure of the overall energy deficit across the wake cross-section. To address this, the area-integrated velocity deficit (AIVD) was computed (Keane et al., 2016). AIVD is a surrogate for wake-induced energy loss since it physically represents the overall momentum deficit caused by the turbine or turbines across a specified cross-sectional plane. Larger integrated velocity deficit areas result in greater downstream power loss and lower aerodynamic efficiency for subsequent turbines, as aerodynamic power extraction scales with the cube of the local velocity. The continuous form is calculated with Eqn 3.8 as

$$AIVD(x/R) = \frac{1}{U_\infty} \iint_A U_d(x/R, y/R, z/R)\,dA \tag{3.8}$$

For discrete measurements, numerical integration is performed as Eqn 3.9

$$AIVD(x/R) \approx \frac{1}{U_\infty} \sum_i \sum_j U_d(x/R, y/R, z/R)\Delta y^* \Delta z^* R^2 \tag{3.9}$$

where: $\Delta y^{*} = \Delta y / \mathrm{R}$ = dimensionless spacings between measurement points in horizontal plane

$\Delta z^{*} = \Delta z / \mathrm{R}$ = dimensionless spacings between measurement points in vertical plane

and, R^{2} converts normalised area to physical units.

The resulting AIVD curves capture the net momentum loss at each downstream location. To illustrate the global spatial organisation of the wake, including wake merging, asymmetry, and recovery trends throughout the transverse plane, the surface plots in this work are intended to serve as qualitative visualisations. For the sole purpose of visual continuity, these charts are created using smooth interpolation from discrete hot-wire measurement points. Crucially, all quantitative comparisons are based on measured values and line profiles directly extracted from the experimental data; no quantitative inferences are made from local interpolated gradients. On the other hand, direct, pointwise comparisons of wake behaviour are also made using line plots of normalised velocity deficit along the horizontal and vertical centreline planes. Surface plots provide an additional tool for interpreting three-dimensional wake structures and interaction patterns. At the same time, these profiles serve as the primary foundation for the quantitative evaluation of wake recovery, spacing effects, and trends in Reynolds number.

3.5 Blockage Correction

A notable concern in wind tunnel studies is the hindrance created by the model under examination. High blockage can lead to distortions in the data collected and affect other connected variables (Treuren, 2015). The extent of this hindrance is typically measured using the blockage ratio (BR), which is calculated by comparing the model's frontal area to the wind tunnel test section area (Treuren, 2015; Howell et al. 2010). In the course of this study, it was discovered that the BRs stand at 3.65% and 7.3% for single and double rotor arrangement respectively. While this in the recommended limit, it was observed during the experiment that the tunnel boundary layer effect is negligible. Although this deviation is minimal, the impact of BR on C_p has been analysed using two distinct blockage correction methods, which are elaborated in the next paragraph.

Chen et al., (2011) proposed a method for correcting blockage in small wind turbines, which involves measuring the blockage factor (BF) expressed as the ratio of inlet velocity with and without the model in the wind tunnel, i.e., U_m / U_∞, as shown in Eq. (3.8). Using this method, the corrected values of λ and C_P can be obtained using Eqs. (3.10) and (3.12) respectively.

$$BF = U_m / U_\infty \tag{3.8}$$

$$\lambda_m = R\omega / U_m \tag{3.9}$$

$$\therefore \lambda = \lambda_m \times BF = R\omega / U_\infty \tag{3.10}$$

$$C_{P,m} = (2\tau\omega / \rho\pi R^2 U_m^3) \tag{3.11}$$

$$\therefore C_P = C_{P,m} \times BF^3 = (2\tau\omega / \rho\pi R^2 U_\infty^3) \tag{3.12}$$

where, the subscript *m* represents the condition with the model. Chen et al., (2011) note that it's crucial to account for the inlet velocity in the current wind tunnel experiments while excluding the model from the corrected parameters.

Consequently, the fan's revolutions per minute within the tunnel remain constant, regardless of whether the model is included or not, to ensure that the suction pressure is maintained at a similar level. Figure 3.14 illustrates how the inlet velocity changes, both with and without the inclusion of the model. The errors recorded in each scenario have been quantified using standard deviation. This study on blockage correction considers different wind speeds, and based on these, the corrected values for λ and C_P are determined using Eqns (3.10) and (3.12). Another widely used approach for wind tunnel correction in wind turbine research is the Pope and Harper blockage correction method (Pope and Harper, 1966). This method outlines the corrected velocity (U_c) through the correction factor (ε_t), as detailed in equation (3.13).

$$U_c = U_\infty(1+\varepsilon_t)\,;\ where,\ \varepsilon_t = \text{Model frontal area/ test section area} \tag{3.13}$$

The equations (3.14) and (3.15) can be used to express the corrected power coefficient ($C_{P,c}$) and corrected tip speed ratio (λ_c).

$$C_{P,c} = (2\tau\omega / \rho\pi R^2 U_c^3)\,;\ and\ \lambda_c = R\omega / U_c \tag{3.14}$$

$$C_{P,c} = C_P / (1+\varepsilon_t)^3\,;\ \text{and}\ \lambda_c = \lambda / (1+\varepsilon_t) \tag{3.15}$$

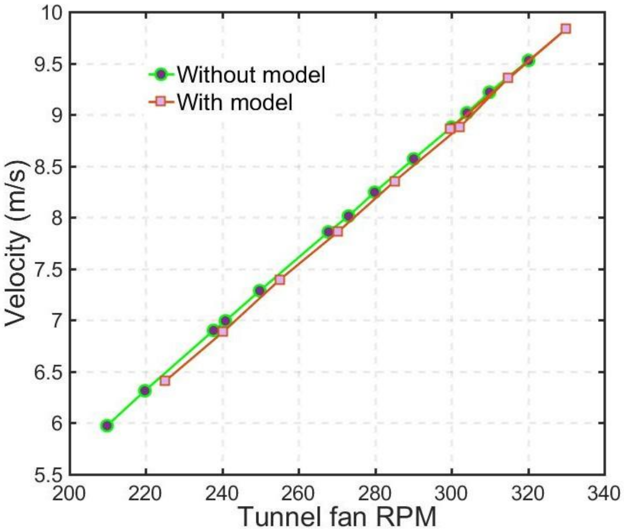

Fig. 3.14 Variation of inlet wind velocity inside the wind tunnel test section

3.6 Concluding *Re*mark

Reliable wake measurements were ensured by the experimental investigation's open-circuit wind tunnel, which had a 2000 mm × 600 mm × 600 mm test section, a contraction ratio of 6:1, a maximum velocity of 50 m/s, and low turbulence intensity (0.3%). Using PLA material and 3D printing, the test models were fabricated for miniature HAWTs with SG6043 airfoil blades with straight and tapered profiles. Operating at low $\lambda = 2.5–3$ within Re of 0.6×10^4 - 1.4×10^4, each rotor included three blades, a radius of 65 mm, and a hub height of 215 mm. The configurations included single- and double-rotor systems with *Ts* of *0.5R* and *1.0R* to prevent blockage adjustments. This resulted in blockage factors of 3.65% and 7.3%, respectively.

The methodology included downstream positions *x/R* = *1* to *4* and concentrated on precise wake mapping in the streamwise, spanwise, and vertical directions concerning the rotor plane. Both streamwise and spanwise velocity components were measured using the HWA technique, which uses a constant-temperature probe with a 10 µm tungsten platinum-coated wire. The HWA was calibrated both before and after tests using pitot-static tubes and an electronic manometer to measure freestream velocities. The data were then fitted to King's law. The data collection system, including a LabVIEW interface and an NI USB6363 DAQ, recorded signals at a sampling rate of 100 Hz at 10-second intervals. A proximity sensor detected the rotor RPM, allowing flow data and operating conditions to be correlated.

Accurate assessment of near-wake generation and wake interactions under low λ conditions was made possible by the setup's low turbulence maintenance, obstruction reduction, and precision calibration. The high-resolution data from this experimental setup were crucial for comprehending wake behaviour in small HAWTs and double-rotor systems, mainly how tip spacing affects wake strength and recovery.

CHAPTER 4

CHARACTERISING THE NEAR WAKE REGIME

4.1 Introductory Remark

In this chapter, the experimental results from investigations on wake characteristics behind SHAWTs are interpreted, focusing specifically on single- and double-rotor configurations. The wake behind the rotor plane of a small HAWT typically divided into several turbulent zones, where the interplay between kinetic energy deficit and helical vortex structures governs the complex three-dimensional flow behaviour (Magnusson and Smedman, 1999; Frandsen, 1992). To assess turbine performance accurately, especially in clustered setups like MRS, one must understand the dynamics and structure of these wake regions, as wake-induced turbulence and momentum deficits significantly influence downstream turbines (Vermeer et al., 2003; Magnusson and Smedman, 1999; Frandsen, 1992).

Researchers primarily study wakes to evaluate (a) the velocity deficit, which determines the power output of downstream turbines, and (b) the turbulence intensity, which causes unsteady loading and structural fatigue. These factors become even more critical in MRS configurations, where closely spaced rotors must minimize wake interference. The velocity deficit determines rotor placement, tip spacing, and overall aerodynamic efficiency (Siram et al., 2023).

The near wake zone typically features helicoidal flow structures, tip and hub vortices, significant velocity deficits, and minimal expansion (Vermeer et al., 2003; Magnusson and Smedman, 1999; Frandsen, 1992). In contrast, the far wake exhibits higher turbulence and gradual velocity recovery, strongly influenced by the ambient environment (Crespo and Herna´ndez, 1996). Rotor geometry and operational conditions shape the distinct dual-peak velocity profile in the near wake. Instability often breaks down tip vortices, leading to vortex coupling and turbulent diffusion (Hu et al., 2012; Li et al., 2016; Lignarolo et al., 2014; Odemark and Fransson, 2013).

To address this gap, systematically wake development and rotor performance are investigated under low *Re* and λ conditions. Then the data are analysed along streamwise (*x/R*), spanwise (*y/R*), and vertical (*z/R*) directions to evaluate how rotor configuration, λ, and BF influence wake propagation, turbulence intensity, and performance metrics.

4.2 Examination of Wake Flow Patterns

The turbine wake is produced by the boundary layer flow separation from the suction regime of the blade airfoil section, and the reverse pressure gradient is the driving parameter for creating the necessary lift. The boundary layer separated from the blade undergoes a complex stochastic flow depicting a pattern of roll-up structure known as vortices. The primary application of this valuable knowledge on wake parametric studies paves the way for defining the various flow regimes of wind turbine wakes, which are distinguished as near wake, far wake regime, and transitional regime. Researchers are often more interested in defining the impact of these wakes on downstream turbines in a wind farm. As the wake evolving from a wind turbine often carries turbulence along with it, any downstream turbine performance shall be greatly impacted when turbines are in close proximity. Many models of wake geometry have been proposed over the years, but the main constraint in describing wake behaviour's true nature has always been a great debate. Near wake regimes often portray the regime of a consistent helical spiral vortex evolving from the tip of the blade. Meanwhile, the far wake regime is described as a decrease in the velocity deficit followed by the recovery process, expansion, and ambient flow interaction in the Wakefield. The transitional regime's nature is still of great concern to have a more precise and physical picture of wind turbine wake vortices that could be employed explicitly to indicate the wake expansion and deficit behaviour by introspection of vortex shedding more profoundly.

The text discusses the increasing importance of wind turbines for generating clean, renewable energy, with a focus on small HAWTs as an efficient and cost-effective option for a wide array of locations. The wake analysis is also an important research prospect for the multirotor configuration. Providing space between wind turbines in an MRS is essential due to wake interaction and increased aggregate fatigue loads, which can lead to a decrease in the performance of adjacent turbines. The ideal spacing is influenced by various factors, including the length of the wind farm, inter-turbine spacing, alignment between the columns and the wind direction, horizontal and vertical staggering of similar or dissimilar turbines. MRS are getting attention because of their lower weight, fatigue loads, and cost.

4.2.1 Single-rotor arrangement

In the single rotor arrangement, the model turbine is placed on the central line axis of wind tunnel. The flow field mapping has been performed along the vertical plane, which includes the span-wise direction (*y/R*) and vertical direction (*z/R*). The velocity mapping has been made with respect to the centre of rotor and with respect to the hub height as shown in Fig. 4.1.

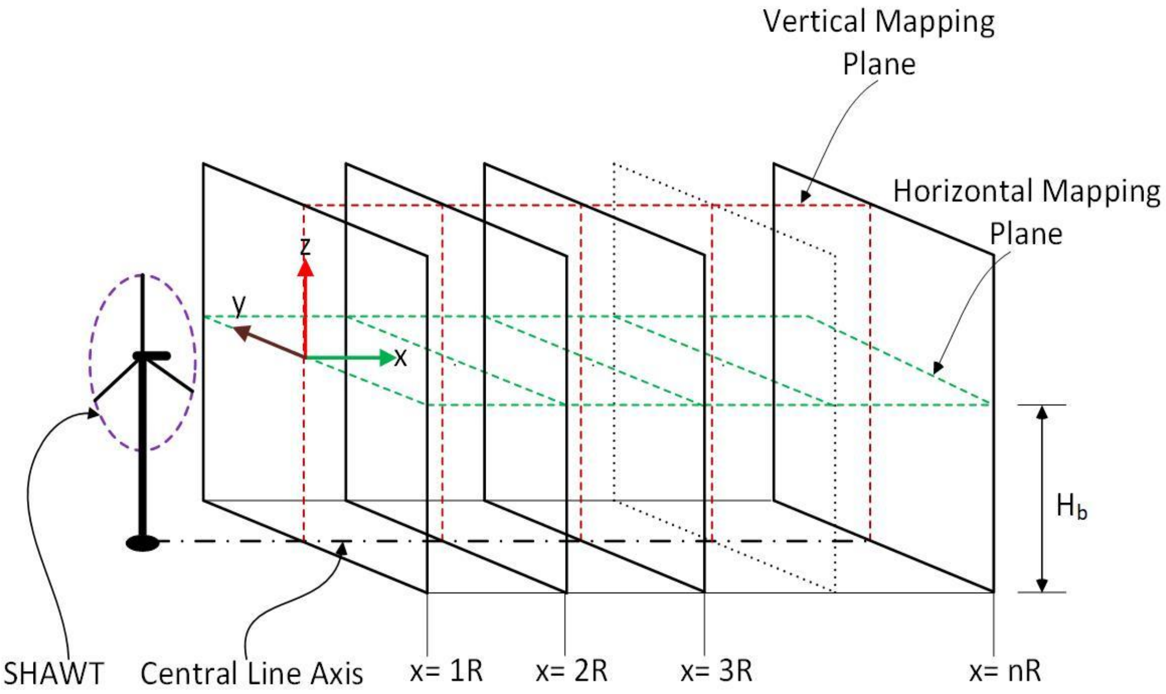

Fig. 4.1 Schematic diagram for single rotor arrangement and mapping planes

4.2.1.1 Span-Wise Analysis in Horizontal Mapping Plane

In the downstream of the rotor, U^* (Eq. 3.7) has been assessed along the span-wise direction. In Fig. 4.2, the result shows that along the span-wise mapping, there is U^* of about 100-75% thereby suggesting the velocity recovery. There is a significant decrease particularly close to the rotor tip, at $y/R = +1$, the U^* decreases from 30% to -5% as one moves downstream. On the other hand, towards the other half, at $y/R = -1$, the U^* ranges between 25% and 3% (Fig. 4.2). It can be said that the deficit near the rotor plane is higher and this can be attributed to both the nacelle and the hub. One can expect the strong presence of hub and tip vortices, which remain intact within the near wake, especially, the top vortices that last longer than the hub/root vortices. The particle image velocity observation by Zhang et al. (Zhang et al., 2012) has reported the presence of tip vortices around 4-6 rotor radius downwind of the rotor plane.

From Fig. 4.2, the deficit at $y/R = \pm 1$ is found to be more than 1, and this behaviour is due to the enhanced velocity caused by the helical motion of wake. The influence of helical vortex in the tangential velocity component is very much prominent within the near wake, as shown in Fig. 4.3. The classical analogy of such behaviour can be taken from the idea that the shear layers created on the wake's edge and the helicoidal tip vortices that diffused through the measurement plane (Singh and Ahmed, 2013; Refan and Hangan, 2012).

4.2.1.2 Span-Wise Analysis in Vertical Mapping Plane

The flow field assessment carried out along the vertical plane suggests the decrease of U^* from 100% to 78%. This effect is noticed at different downstream locations from the rotor plane (Figs. 4.4 and 4.5). Above the rotor plane (z/R = +1), the U^* decreases from 4% to 2% along the downstream locations. However, below the rotor plane (z/R = -1), the U^* is 90%, 23%, and 30% at x/R = *1*, *2*, and *3* respectively. Similar to the observation made along the horizontal mapping, here also, the deficit is found to be minimum near the helical vortex indicating a localized increment of wind speed as compare to other locations, the tower effect is more pronounced at x/R = 1, and this found to be is more dominant than the boundary layer flow in the vertical mapping plane when $H_b/R = 3.308$.

Usually, the wind turbine wake study comprises of two scenarios viz., (i) neutral boundary layer (NBL) and (ii) ABL (Khan et al., 2017). In contrast to the ABL situation, the NBL shows the distinct tip vortices. Additionally, the NBL exhibits a significant rise in the fluctuations of stream-wise velocity in the wake, indicating that the turbine generates turbulence and disperses energy (Adhikari et al., 2018; Hancock et al., 2014; Tieleman, 1992). The vortices in NBL therefore become stronger and more densely packed in a smaller vertical space. Khan et al., (2017) observed similar impact of blade aerodynamics in the near wake flow as the primary cause of the variations between the two scenarios. Their three-component velocity assessment using PIV suggests that a rotor will have a concentrated band close to the blade tip but not at the bottom-tip height. This discrepancy results from the slower tip vortex dissipation at the top-tip height where the entering flow has a lesser turbulence than at the bottom-tip height (Singh and Ahmed, 2013).

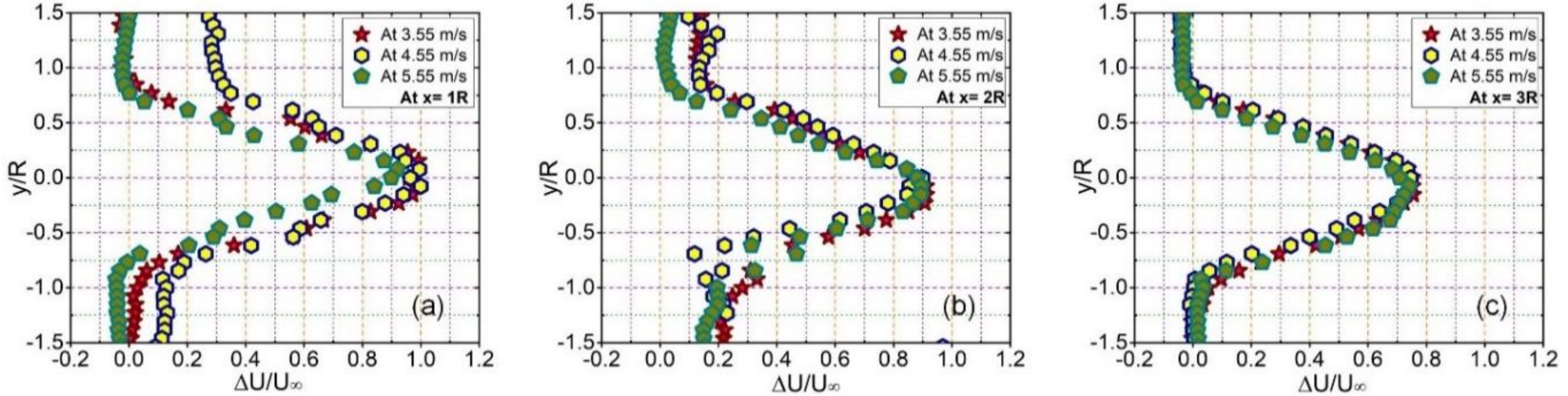

Fig. 4.2 Velocity deficit along downstream locations in horizontal plane of the single rotor arrangement (a) at *x/R* = *1*, (b) at *x/R* = *2* and (c) at *x/R* = *3*

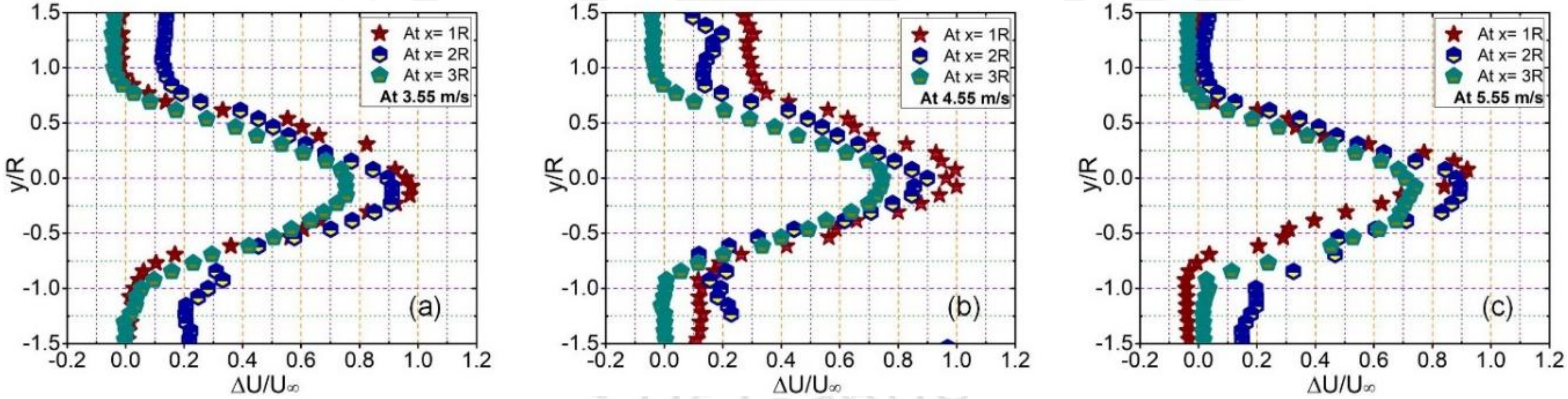

Fig. 4.3 Effect of wind speed on velocity deficit in horizontal plane of the single rotor arrangement (a) at U_∞ = 3.55 m/s, (b) at U_∞ = 4.55 m/s and (c) at U_∞ = 5.55 m/s

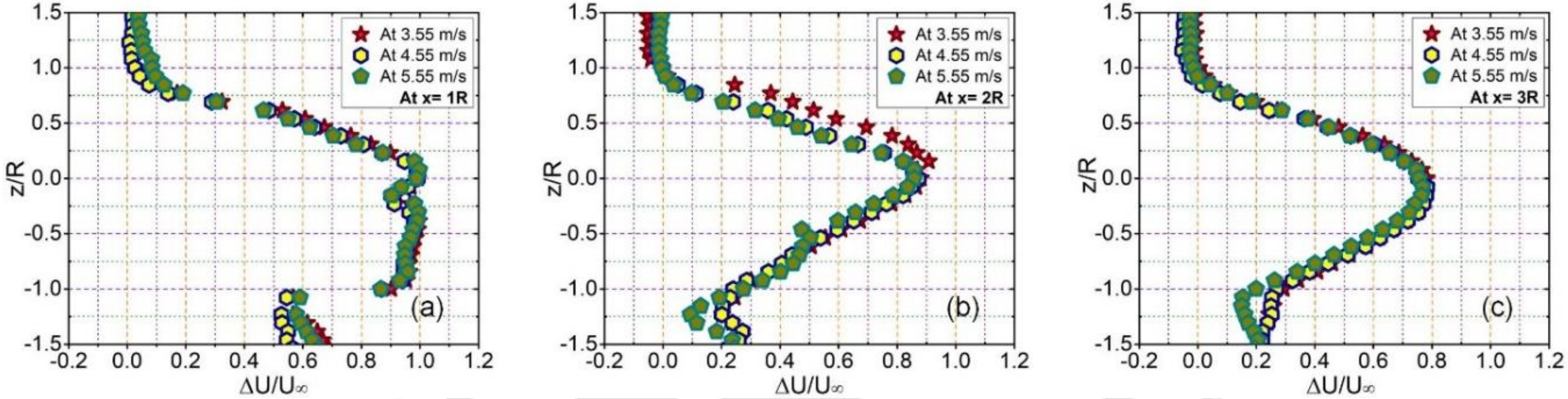

Fig. 4.4 Velocity deficit along downstream locations in vertical plane of the single rotor arrangement (a) at *x/R = 1*, (b) at *x/R = 2* and (c) at *x/R = 3*

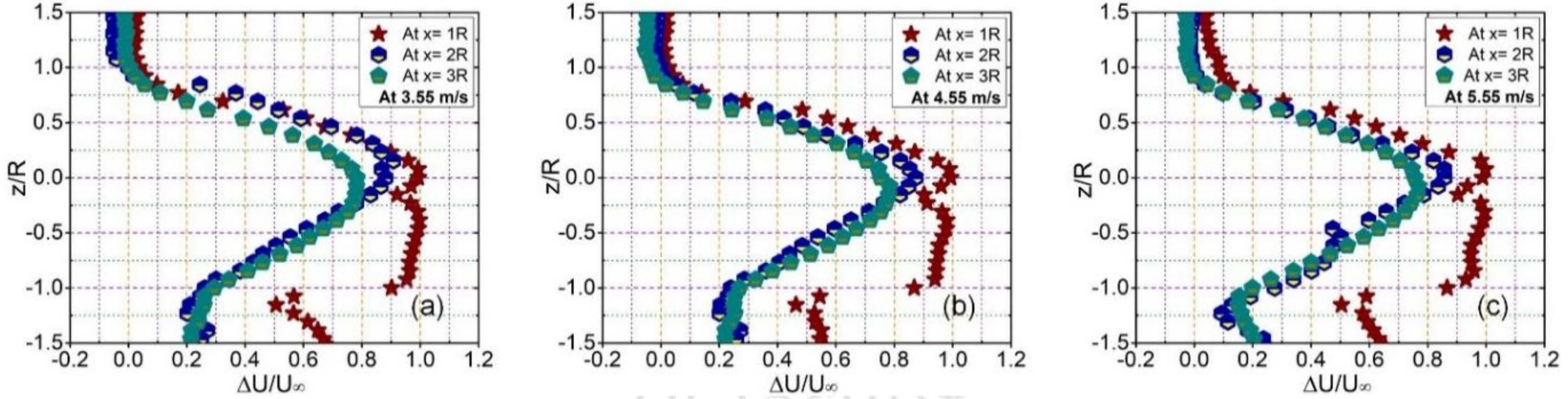

Fig. 4.5 Effect of wind speed on velocity deficit in vertical plane of the single rotor arrangement (a) at U_∞ = 3.55 m/s, (b) at U_∞ = 4.55 m/s and (c) at U_∞ = 5.55 m/s

4.2.2 Double-rotor arrangement

In the double-rotor arrangement, the model turbines of identical configuration are placed equidistantly from the tunnel central axis (Fig. 4.6). The flow field mapping has been performed along the horizontal and vertical planes, which includes the downstream direction (x/R), span-wise direction (y/R) and the vertical direction (z/R). The characterization reference has been taken with respect to the rotors plane at hub height and along the tunnel central axis. Further, the spacing between the rotors has been marked with respect to the blade tip is defined as tip spacing (T_S) as shown in Fig. 4.6. In this arrangement, models are placed at two different $T_S = 0.5R$ and $1.0R$.

One essential geometric factor that controls MRS's wake formation, interaction, and recovery characteristics is the tip spacing between rotors. When several rotors are positioned laterally, the separation between the tips of their blades can significantly impact how each wake interacts with the others. Increased turbulence and asymmetric flow patterns can arise from early wake merging and more mutual interference caused by a more minor tip separation. However, greater separation tends to lessen direct contact, enabling the wakes to develop more autonomously and recover more consistently downstream. Optimizing rotor arrangements requires understanding how tip spacing affects wake characteristics, particularly in applications like small-scale distributed wind farms, dual-rotor turbines, and experimental testing in restricted spaces. This section uses span-wise velocity deficit profiles at several downstream locations to examine the effects of rotors tip spacing variations ($T_S = 0.5R$ and $T_S = 1.0R$) on wake behavior in both vertical and horizontal directions.

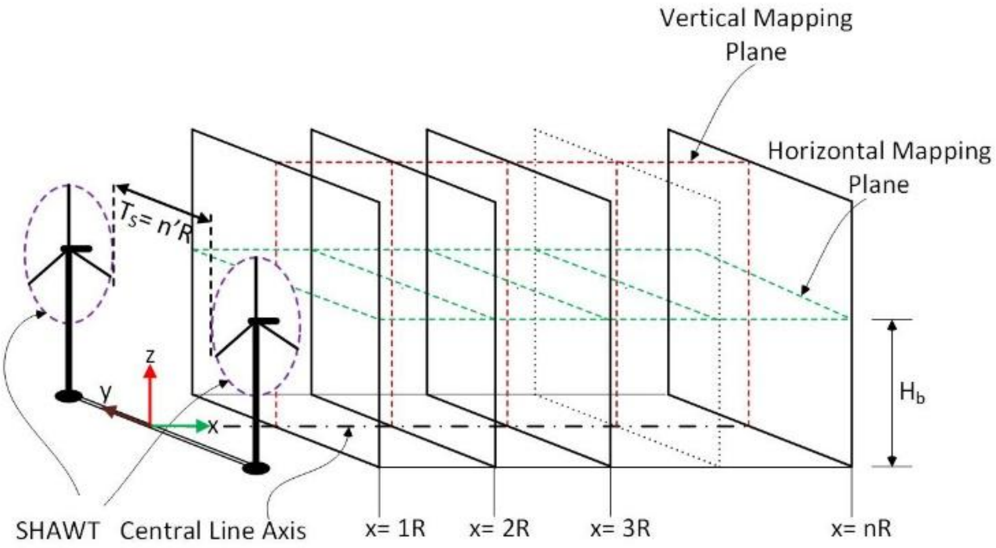

Fig. 4.6 Schematic diagram of the double rotor's arrangement and the mapping planes

4.2.2.1 Span-Wise Analysis in Horizontal and Vertical Mapping Planes at $T_S = 0.5R$

In this study, the flow field mapping has been done along the y/R and x/R or x-y plane (Fig. 4.6). The wake investigation has been made at four downstream locations ($x/R = 1, 2, 3$, and 4) and at two lateral or span-wise positions ($y/R = +1.25$ and $y/R = -1.25$) with respect to the tunnel central axis. At $x/R = 1$, a maximum U^* of about 5% is noted at $U_\infty = 5.55$ m/s, and the minimum U^* is around -3% at $U_\infty = 4.55$ m/s at the central axis. At $y/R = +1.25$, U^* is around -3% for all the wind speeds close to the rotor blade tip ($y/R = +0.5$). Whereas, at $y/R = -1.25$, the maximum U^* is around 2% at $U_\infty = 5.55$ m/s, and the minimum U^* is found to be around -2% at $U_\infty = 4.55$ m/s. It can be observed that with the increase of wind speeds, there is higher fluctuations in U^* particularly in the region $0 < y/R < +1.25$ (Fig. 4.7(a)). The assessment at $x/R = 2$ shows the maximum U^* of about -2% at $U_\infty = 3.55$ m/s, and the minimum U^* of about -5% at $U_\infty = 5.55$ m/s at the central axis. When the model turbines are placed at $y/R = +1.25R$, the maximum U^* is found to be around 4% at $U_\infty = 3.55$ m/s, and the minimum U^* is around -4% at $U_\infty = 5.55$ m/s at the rotor blade tip.

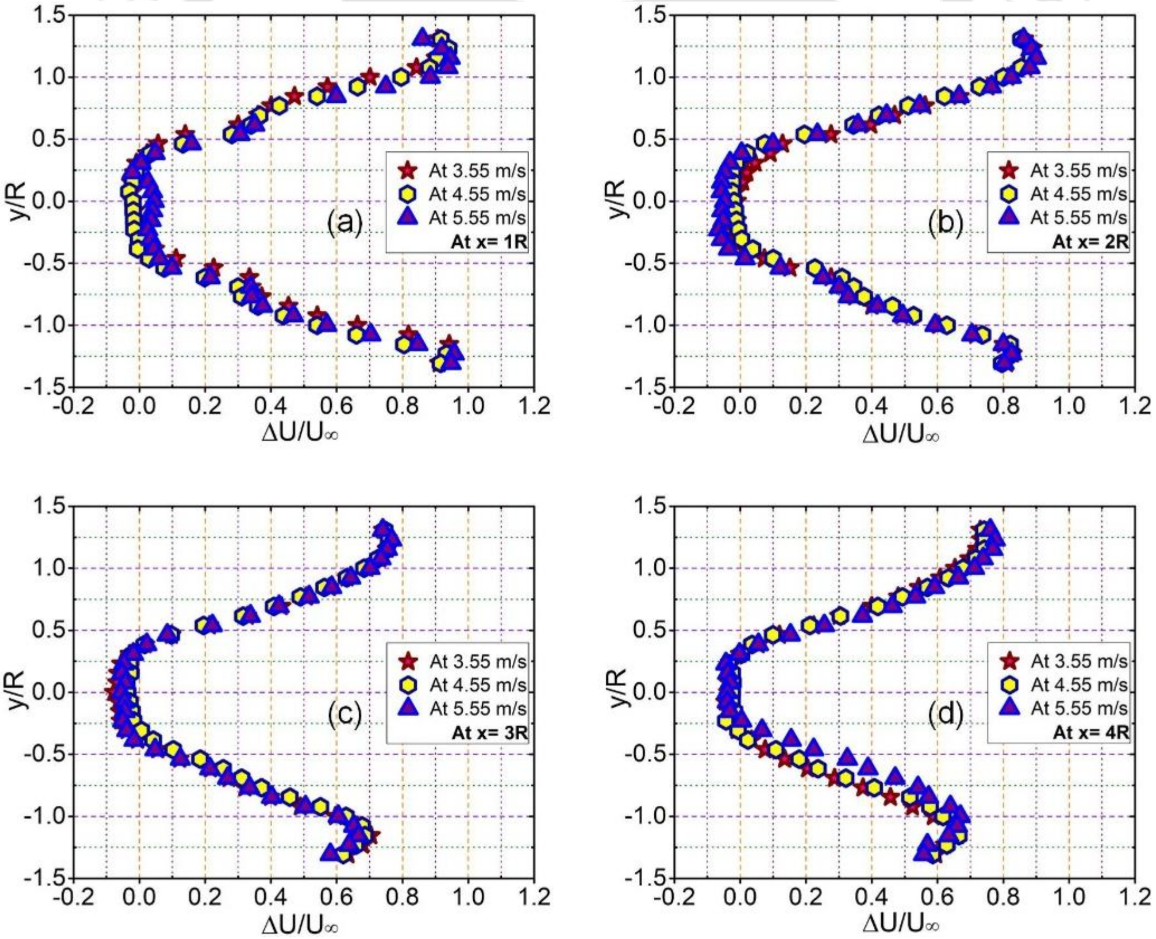

Fig. 4.7 Velocity deficit along downstream locations in horizontal plane of the double rotor arrangement (a) at $x/R = 1$, (b) at $x/R = 2$, (c) at $x/R = 3$ and (d) at $x/R = 4$

Whereas, at *y/R = -1.25*, the maximum U^* is around -1% at U_∞ = 4.55 m/s, and the minimum U^* is around -5% at U_∞ = 5.55 m/s at the tip of the rotor blade (Fig. 4.7(b)). At *x/R = 3*, a maximum U^* is about -4% at U_∞ = 4.55 m/s, and the minimum U^* is around -6% at U_∞ = 3.55 m/s has been observed (Fig. 4.7(c)). Again, at *y/R= +1.25*, the U^* of about -3% at U_∞ = 4.55 m/s, and a U^* is around -5% at U_∞ = 3.55 m/s has been observed at the rotor blade tip. Further, at *y/R*= -1.25, a maximum U^* of about -2% at U_∞ = 4.55 m/s, and a minimum U^* of about -4% at U_∞ = 3.55 m/s has been observed at the tip of the rotor blade (Fig. 4.7(c)). Finally, at *x/R = 4*, the U^* is around -4% for all wind speeds in between the tip spacing of rotors (Fig. 4.7(d)). It is to be noted that negative velocity deficit is attributed to the enhanced velocity far from the rotor tip. Due to the closer tip spacing, the tip vortices generated from the rotor blades interact with each other. This phenomenon help increases the stream velocity in downstream.

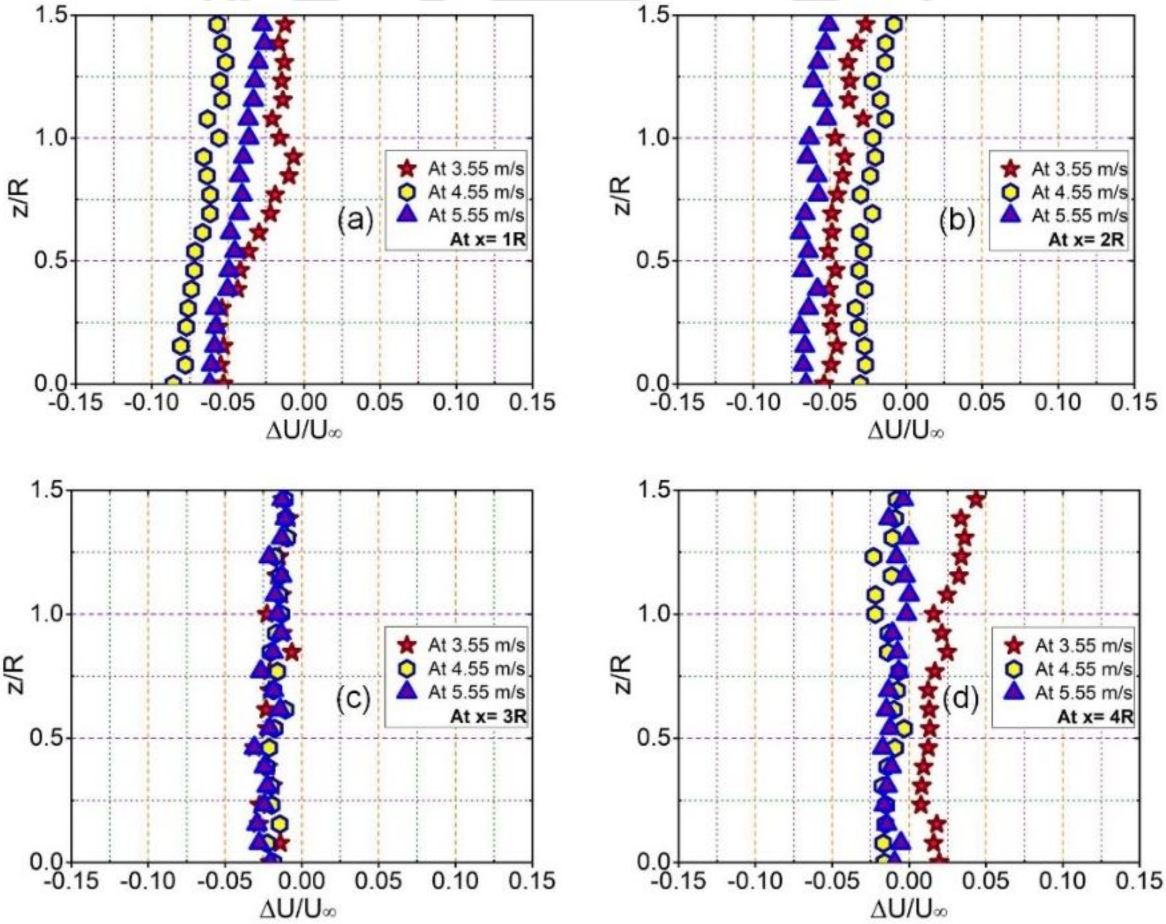

Fig. 4.8 Velocity deficit along downstream locations in vertical plane of the double rotor arrangement (a) at *x/R = 1*, (b) at *x/R = 2*, (c) at *x/R = 3* and (d) at *x/R = 4*

The results of span-wise wake characteristics along the vertical direction and at different downstream locations of the double-rotor arrangement is discussed here. Figure 4.8 presents the detailed U^* profiles at various downstream locations (*x/R = 1, 2, 3,* and *4*) along the tunnel central axis. At $x/R = 1$, the U^* is minimum at $U_\infty = 4.55$ m/s through the vertical axis; while it is maximum at $U_\infty = 3.55$ m/s and at $U_\infty = 5.55$ m/s for the upper half and lower half of the hub height, respectively (Fig. 4.8(a)).

A similar observation has been made at $x/R = 2$, where U^* is maximum at $U_\infty = 4.55$ m/s, and minimum at $U_\infty = 5.55$ m/s along vertical line of the central axis (Fig. 4.8(b)). At $x/R = 3$, the U^* is almost the same in the tested range of wind speeds and increases from -2.5 to 0% in vertically upward direction on the central axis where the influence of freestream becomes prominent (Fig. 4.8(c)). Finally, at $x/R = 4$, the U^* is maximum at $U_\infty = 3.55$ m/s, and minimum at $U_\infty = 4.55$ m/s and 5.55 m/s along a vertical line of the central axis (Fig. 4.8(d)). It is to be noted here that the observation has been made with respect to the tunnel central line. Thus, a very minimal deficit is obtained in most of the cases, unlike the measurements taken with respect to the center of the rotor plane and hub height.

4.2.2.2 Span-Wise Analysis in Horizontal and Vertical Mapping Planes at $T_S = 1.0R$

In this case, the wake flow characteristics are analysed for a $T_S = 1.0R$, with measurements taken at four downstream locations ($x/R = 1, 2, 3$, and 4) and lateral spanwise positions of **$y/R = \pm 1.5$**. At **$x/R = 1$** (Fig. 4.9(a)), the maximum U^* reaches approximately **4%** at **$U_\infty = 5.55$ m/s** along the central axis, while the minimum value of about **-2%** is observed at **$U_\infty = 3.55$ m/s**. At **$y/R = +1.5$**, the velocity deficit drops to nearly **0%**, indicating a **weaker wake influence** and minimal interaction at this outer radial location. Similarly, at **$y/R = -1.5$**, the wake influence is low, with U^* values hovering between **-1% and 1%**, suggesting effective diffusion of tip vortex effects toward the periphery. At **$x/R = 2$** (Fig. 4.9(b)), the wake spreads further laterally. Along the central axis, U^* ranges from **-1% to -4%** depending on wind speed, while at **$y/R = +1.5$**, the velocity deficit remains small (0% to 2%), reflecting **partial diffusion and recovery** of the wake. At **$y/R = -1.5$**, a slight asymmetry is noticed, with some **velocity amplification ($U^* > 0\%$)**, especially at **$U_\infty = 3.55$ m/s**, which may be due to minor vortex interaction or localized acceleration near the tip region.

At **$x/R = 3$** (Fig. 4.9(c)), the **wake recovery becomes more prominent**, with a more uniform velocity deficit distribution across y/R. The central region shows U^* values around **-3% to -4%**, and values at $y/R = \pm 1.5$ range between **-1% and 1%**, indicating **weaker tip vortex interaction** and continued diffusion of wake effects laterally. The overall profile exhibits improved symmetry across the span. Finally, at **$x/R = 4$** (Fig. 4.9(d)), the velocity profile flattens significantly, and U^* remains between -2% and -4% near the rotor region. At y/R = ± 1.5, the U^* values approach 0%, showing that the wake has nearly recovered in these outer lateral positions. This suggests minimal residual wake energy beyond the rotor tip extent.

Compared to the $T_S = 0.5R$ case, the tip vortex interaction is significantly reduced at $T_S = 1.0R$, leading to greater lateral wake dispersion**,** lower peak fluctuations, and smoother downstream flow. The enhanced spacing prevents strong vortex merging, promoting wake symmetry and reducing the induced acceleration between the rotors.

For given tip spacing, the effect of tip and root vortices interaction propagates downstream of laterally placed wind turbines. For a particular location, only tip vortices come into the picture, and after that tip and root vortices affect the flow behind the plane of the rotors, and after a certain point only tip vortices with wake superposition effect appear, however, root vertices disappear after that certain point because the strength of root vortices is less than the strength of tip vortices.

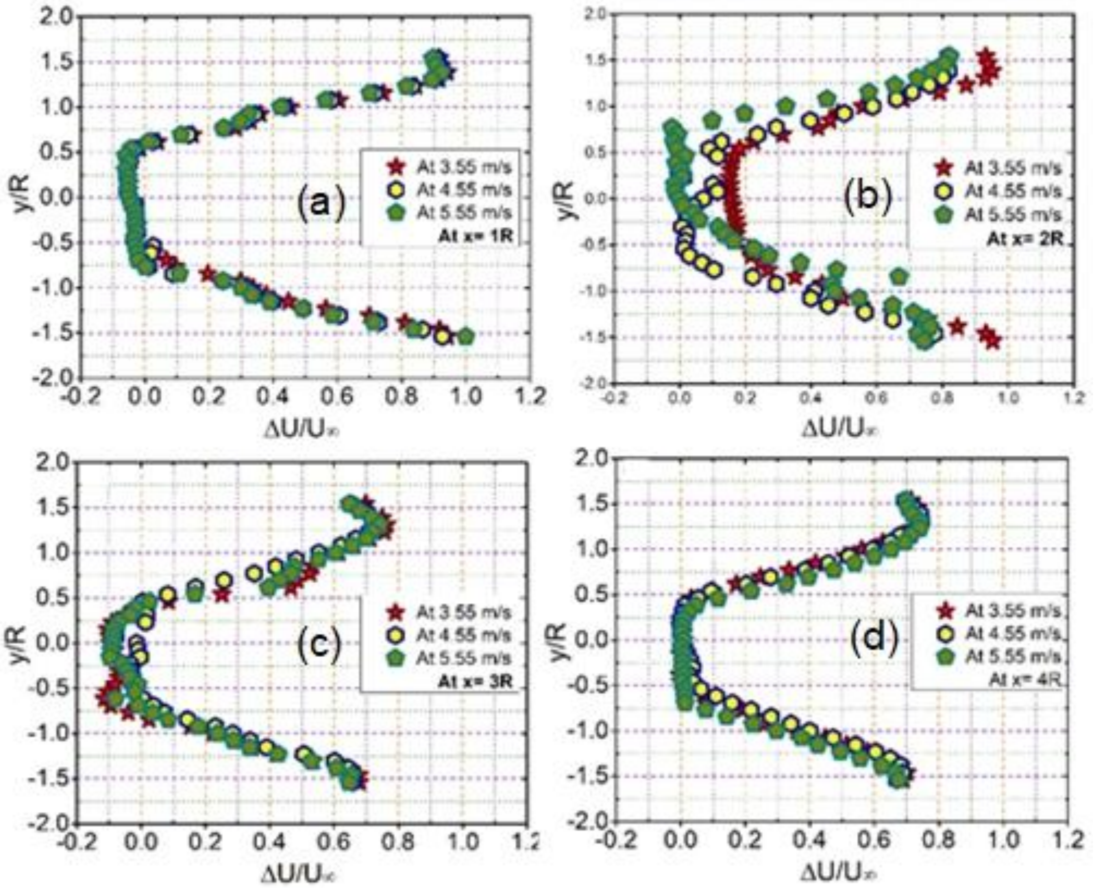

Fig. 4.9 Velocity deficit along downstream locations in horizontal plane of the double rotor arrangement (a) at $x/R = 1$, (b) at $x/R = 2$, (c) at $x/R = 3$ and (d) at $x/R = 4$

At $x/R = 1$ (Fig. 4.10(a)), a symmetric wake structure is observed across the vertical axis. The U^* remains consistent for all three inlet wind speeds (U_∞ = 3.55, 4.55, and 5.55 m/s), especially within the range $z/R = -1$ to $+1$. The profiles show a gradual wake recovery trend from lower to upper tip regions, and the minimum deficit occurs near the rotor plane for all speeds. **At** $x/R = 2$ (Fig. 4.10(b)), significant asymmetry develops in the U^*, particularly at lower wind speeds. The profile for U_∞ = 3.55 m/s shows large deviation and scattered values below the hub height ($z/R < 0$), indicating wake deflection or turbulence possibly caused by rotor interaction. Meanwhile, U_∞ = 4.55 and 5.55 m/s profiles display more structured but bifurcated wake cores on either side of the vertical axis.

At $x/R = 3$ (Fig. 4.10(c)), partial recovery is evident. The U^* profiles for U_∞ = 4.55 and 5.55 m/s merge more clearly in the upper half of the rotor zone ($z/R > 0$), but U_∞ = 3.55 m/s still shows signs of persistent wake deviation and fragmentation in the lower half. Overall, wake coherence improves for higher inflow speeds. **At** $x/R = 4$ (Fig. 4.10(d)), the U^* profiles converge considerably for all three wind speeds. The deficits are centred and consistent, indicating that the wake becomes stabilized and more symmetric downstream. This suggests a strong influence of freestream mixing and minimal impact from the initial wake distortion seen closer to the rotor.

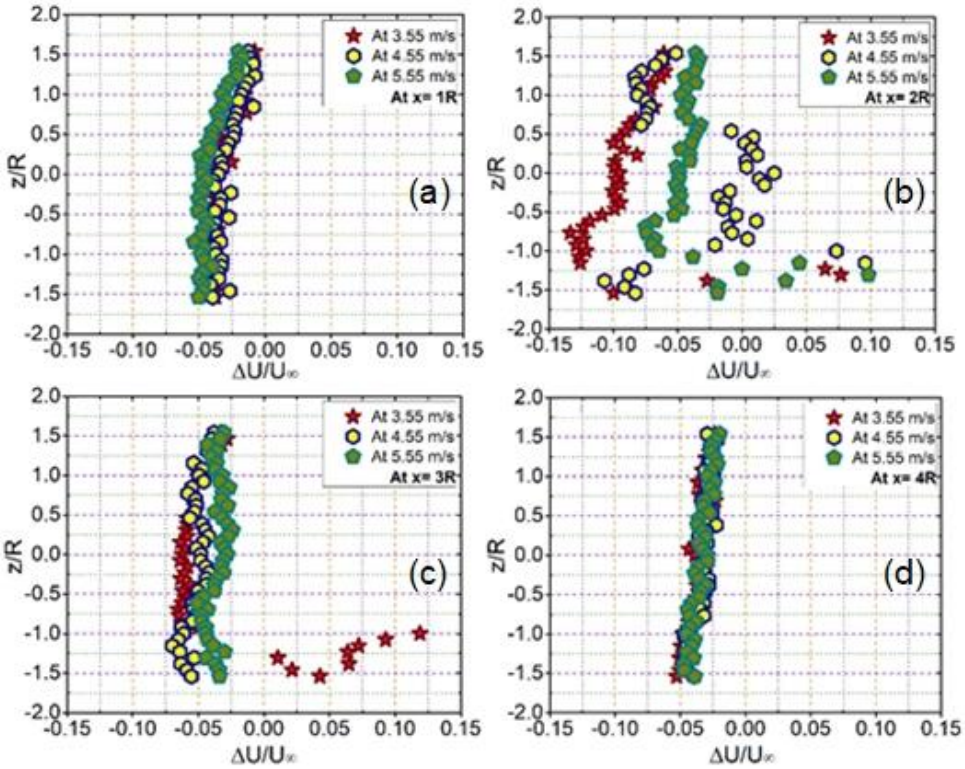

Fig.4.10 Velocity deficit along downstream locations in vertical plane of the double rotor arrangement (a) at $x/R = 1$, (b) at $x/R = 2$, (c) at $x/R = 3$ and (d) at $x/R = 4$

4.2.3 Comparative Analysis

To evaluate the impact of rotor tip spacing on wake development, two configurations were compared: $T_S = 0.5R$ and $T_S = 1.0R$. The main focus of this investigation is the span-wise wake characteristics at different downstream places in both vertical and horizontal mapping planes. A comparison of the velocity deficit (U^*) distributions across the tunnel cross-sections revealed significant variations in wake symmetry, recovery, and extent. The configuration with $T_S = 0.5R$ showed higher wake interactions in the near-wake region, leading to smaller and more asymmetric profiles, particularly in the vertical direction. On the other hand, the $T_S = 1.0R$ arrangement produced wider wake patterns that were more symmetrical and had a quicker velocity recovery downstream. This suggests that there was less mutual interference between the two rotors. A deeper understanding of the effects of rotor spacing on aerodynamic performance, wake stability, and flow quality—all crucial elements in the design and optimization of double-rotor systems—is provided by this comparative study. Finally, overall comparison in between single- and double-rotor arrangements in horizontal mapping plane.

4.2.3.1 Comparative Analysis in Horizontal Mapping

In the case of $T_S = 0.5R$, the U^* profiles show a pronounced double-peak structure at all downstream locations. At $x/R = 1$, these peaks are sharp and well-separated, indicating limited wake mixing immediately behind the rotor. As the flow progresses to $x/R = 2$, 3, and 4, the two wake cores begin to merge and become increasingly diffuse due to turbulent interaction. Nevertheless, even at $x/R = 4$, the overlapping structure remains evident, reflecting strong mutual interference between the closely spaced rotors. The central region between the rotors exhibits a persistent velocity deficit, suggesting slower wake recovery.

On the other hand, the $T_S = 1.0R$ configuration demonstrates distinct wake behaviour. At $x/R = 1$, the wakes are still clearly separated, and the core deficits are slightly more pronounced due to reduce near-field mixing. From $x/R = 2$ onward, the profiles show wider spreading and more uniform distribution across the span. By $x/R = 3$ and 4, the wake becomes more symmetric and smoother, indicating weaker interaction between the two wakes. The larger spacing allows greater flow entrainment from the sides, leading to more effective wake dissipation and faster velocity recovery. Comparatively, the $T_S = 0.5R$ spacing leads to stronger wake overlap, greater asymmetry, and slower flow recovery, while $T_S = 1.0R$ facilitates more isolated wakes with quicker dissipation and improved symmetry. This implies that increasing rotor spacing can significantly improve aerodynamic performance and minimize energy losses due to wake interference.

4.2.3.2 Comparative Analysis in Vertical Mapping

The U^* for $T_S = 0.5R$ remains relatively narrow and symmetric across downstream positions. At ***x/R* = *1***, the deficit is concentrated near the upper rotor region. As the flow moves downstream to ***x/R* = *2* and *3***, symmetry is maintained and the deficit reduces, indicating steady wake recovery. By ***x/R* = *4***, significant recovery is seen, with some overcompensation at low wind speeds suggesting enhanced freestream mixing. Overall, the close rotor spacing leads to constrained but stable wake development with limited vertical deflection.

For $T_S = 1.0R$, the wake is broader and more scattered at $x/R = 1$, due to reduced rotor interaction. At $x/R = 2$, significant vertical asymmetry and wake deflection appear, particularly at lower wind speeds. These effects begin to stabilize by $x/R = 3$, though some asymmetry persists. By $x/R = 4$, the wake is fully recovered and symmetric, with minimal U^*. This suggests that while the larger spacing allows more turbulence and deflection early on, it supports cleaner wake recovery farther downstream.

4.2.3.3 Comparison in between Single- and double-rotor arrangements

In this subsection, a direct comparison is made among the test cases. For $x/R = 1$, a comparative assessment within $y/R < 1$ suggests that there is higher U^* for the double rotor ($T_S = 0.5R$) as compared to the single rotor at $U_\infty = 5.55$ m/s (Fig. 4.11(a)). Whereas at $y/R > 1$, there is more U^* for the single rotor at $U_\infty = 4.55$ m/s as compared to double rotor ($T_S = 1.0R$). Now, as seen in Fig. 4.11(b), at $x/R = 2$, there is more U^* ($T_S = 1.0R$) for $U_\infty = 3.55$ m/s, while there is lesser U^* for $T_S = 1.0R$ at $U_\infty = 5.55$ m/s within $y/R < 1$. On the other hand, there is relatively more U^* for the single rotor at all the wind speeds as compared to the double rotor when $y/R > 1$. Further, at $x/R = 3$, there is more U^* for $T_S = 1.0R$ for $U_\infty = 3.55$ m/s, whereas there is lesser U^* for the single rotor for $U_\infty = 4.55$ m/s when $y/R < 1$ (Fig. 4.11(c)).

The tip velocity is more enhanced by the closer tip spacing in downstream ($2 < x/R < 3$) of rotor plane, while the rotor plane flow velocity is enhanced in case of the single rotor. It is evident that for all the test cases, the double rotor with $T_S = 0.5R$ has the lower value of U^* relative to the single rotor. From the comparative analysis, it can be understood that the tip spacing increases the amount of streamwise distance that each rotor's wake can transport without experiencing significant interactions with the wakes of nearby rotors (Milborrow, 1980).

The observed wake behaviour is intimately related to the accompanying turbulence intensity and shear-layer instability mechanisms, even though the current chapter focuses mainly on the spatial evolution of the normalised velocity deficit to characterise the near wake regime. Strong velocity gradients at the rotor slipstream boundary, along with the roll up of tip vortices and hub shed vortical structures, are the sources of high turbulence levels in the near wake. In both single and double-rotor configurations, these mechanisms control wake stability, symmetry breakdown, and the early phases of wake recovery.

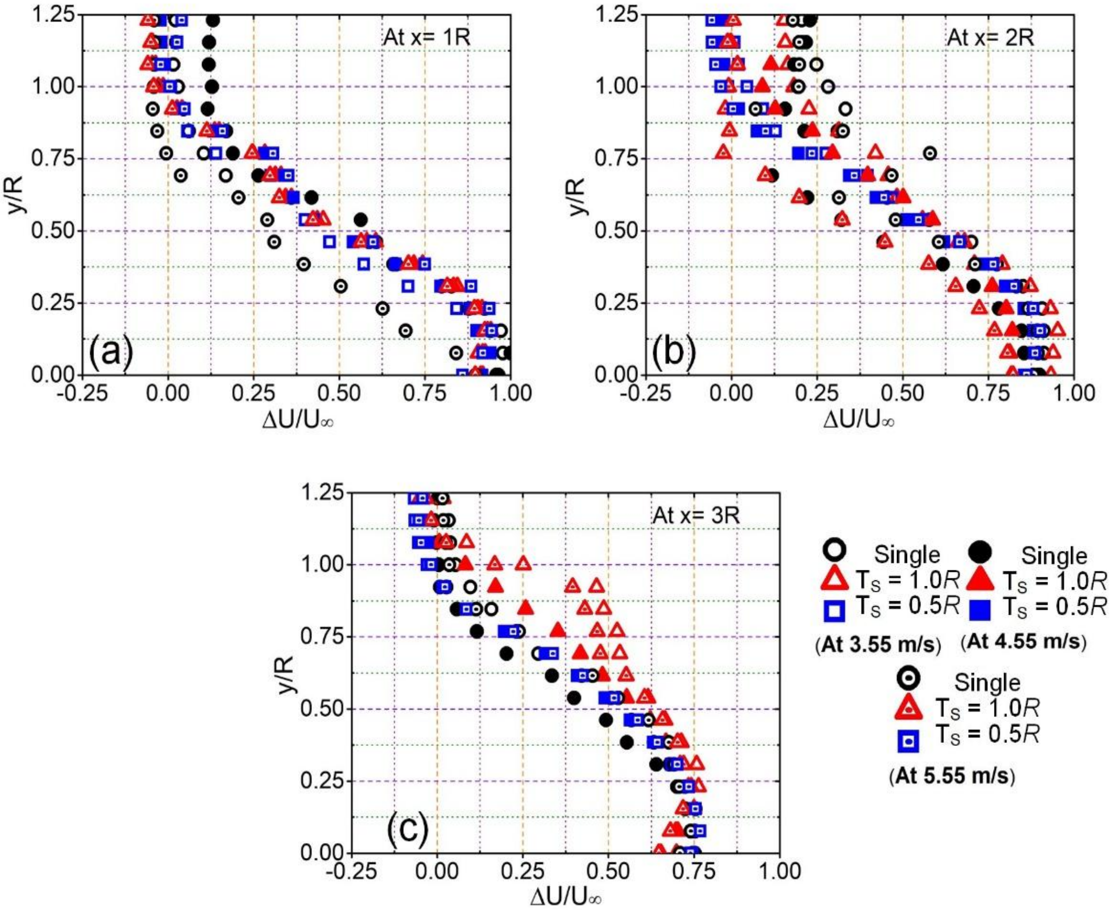

Fig 4.11 Span-wise flow analysis at (a) x/R = 1, (b) x/R = 2, and (c) x/R = 3 downstream location for all configurations

The measured velocity deficit decay trends qualitatively follow self-similar wake growth behaviour from a classical wake development perspective, in which the centreline velocity deficit decreases as a function of streamwise distance, and the wake width grows roughly linearly with downstream distance. However, the combined effects of low *Re* operation, higher viscous diffusion, and strong vortex coherence typical of small-scale rotors cause deviations from perfect self-similarity in the current investigation. In contrast to large-scale turbines, these effects prolong the persistence of near-wake asymmetry and delay the breakup of organised tip vortices.

Through the mutual interference of nearby shear layers and induced velocity fields, wake interaction further affects this classical behaviour in the double-rotor arrangement, changing both momentum recovery and turbulence creation. Wider spacing allows for partial rebuilding of individual rotor wakes before collision, whereas closer spacing increases shear layer interaction and accelerates wake spreading. Therefore, the current results show that near-wake evolution in small double-rotor systems is strongly conditioned by low *Re* aerodynamics and rotors interaction effects, justifying the need for dedicated experimental characterisation as undertaken in this chapter, even though classical wake-scaling concepts offer a helpful qualitative framework.

4.3 Summary of the Study

A thorough experimental study of wake production in a single and double-rotor HAWT system. A double-rotor system with different tip spacing (T_S = $0.5R$ and $1.0R$). Both horizontal and vertical mappings were used to examine the wake behaviour at three different inflow wind speeds (U_∞ = 3.55 m/s, 4.55 m/s, and 5.55 m/s) and several downstream locations (x/R = *1, 2, 3,* and *4*).

A single-rotor wind turbine's wake shows a progressive recovery in wind speed, less flow distortion as the downstream distance increases, and a steady decrease in the velocity gradient. A prominent velocity deficit core, surrounded by shear layers and tip vortices, defines the wake structure, whereas the near-wake region is asymmetrical and has high turbulence intensity. Minor yaw misalignments add to wake asymmetry, whereas localised disturbances from the nacelle, hub, and tower further aggravate non-uniformities. When helical vortex structures form, tangential velocity components are introduced at lateral regions, and the vortex pitch increases downstream as a function of inflow velocity. Partial velocity recovery is facilitated by ongoing ambient flow entrainment, which results in a more dispersed wake downstream.

In the horizontal plane, strong interaction zones between the two rotor wakes, particularly close to the central region, were produced by the T_S = $0.5R$ configuration, resulting in symmetric profiles and larger velocity deficits. Conversely, the T_S = $1.0R$ configuration showed less turbulent interaction in the near wake and wider wake spreading and decreased deficit intensity, indicating increased independence across rotor wakes. With a distinct concentration of velocity deficit close to the upper part of the rotor, the T_S = $0.5R$ condition showed more symmetric and compact wake formations in the vertical direction close to the rotor plane. On the other hand, the $T_S = 1.0R$ configuration displayed more asymmetric and larger wake profiles, especially between $x/R = 2$ and 3.

Single- and double-rotor systems show different wake patterns influenced by downstream position and rotor tip spacing. Single rotor configuration exhibits higher U^* at $y/R > 1$, while double rotors with $T_S = 0.5R$ have higher U^* within $y/R < 1$ at inflow velocity. At $x/R = 2$, single rotor maintains higher U^* beyond $y/R > 1$, whereas the $T_S = 1.0R$ configuration shows elevated U^* at lower inflow velocity. By $x/R = 3$, single rotor regains higher values at moderate speeds, while $T_S = 1.0R$ still exhibits enhanced U^* at low speeds.

Overall, our findings suggest that larger spacing ($T_S = 1.0R$) permits higher flow generation and further downstream recovery, while closer tip spacing ($T_S = 0.5R$) improves velocity deficits in the near wake. Higher core velocities close to the rotor plane are typically encouraged by single rotors, but stronger interactions with double rotors result in lower U^*. This is consistent with the hypothesis that greater tip separation permits individual wakes to grow more freely across longer streamwise lengths by reducing mutual wake interference.

CHAPTER 5

LOW TIP SPEED RATIO CONDITIONS

5.1 Introductory Remark

Low λ wind turbines, which are generally characterised by λ values less than 3, have aerodynamic properties that are significantly different from those seen at higher λ. These regimes cause reduced aerodynamic loading, decreased efficiency, and noticeable wake structures because the blades rotate more slowly about the incoming wind speed. Designing reliable multi-rotor systems requires an awareness of these situations, which are prevalent in small-scale wind turbines, start-up stages, or low-wind regions.

This chapter only discusses experimental settings that correlate to $\lambda = 2.5 - 3$, which apply to the three inflow velocities investigated in this study (U_∞ = 3.55 m/s, 4.55 m/s, and 5.55 m/s) in the double-rotor configuration and assesses deficit behaviour. The normalised velocity deficit, a direct measure of the energy collected by the double-rotors turbine and the momentum loss imparted to the flow, is the main aerodynamic parameter that is investigated. The evolution of wake shape, depth, and expansion under these low λ conditions are revealed by analysing surface plots of velocity deficit in both the horizontal and vertical planes.

5.2 Double-Rotor Wake Behaviour under Low Tip Speed Ratio

5.2.1 Overview of Wake Interaction Mechanisms

A HAWT's wake is an area of momentum deficit brought on by the airflow's energy being extracted. Because the rotors are so close together in a double-rotor arrangement, wake interaction is increased. Tip spacing and input velocity determine the degree of wake merging, turbulence mixing, and flow recovery speed. This study uses qualitative visualisations and quantitative integration approaches to examine the effects of various characteristics on aerodynamic performance. Conversely, more independent wake development and smoother downstream flow are encouraged by larger separation.

5.2.2 Wake Characteristics at $T_S = 0.5R$

5.2.2.1 Horizontal Plane Behaviour

The results of U^* of the double-rotor arrangement at three different wind speeds (U_∞ = 3.55 m/s, 4.55 m/s, and 5.55 m/s) and at four different downstream positions (x/R = *1*, *2*, *3*, and *4*) are discussed in Fig. 5.1. The region opted is within the near wake regime. At U_∞ = 3.55 m/s, a maximum U^* occurs at $x/R = 2$ along the central axis, while the minimum U^* is observed at $x/R = 3$. The placement of model turbines at $y/R = +1.25$ and -1.25 influences U^* which is minimum near the central axis (Fig. 5.1(a)). At U_∞ = 4.55 m/s, relatively consistent velocity deficits are observed in between the tip spacing of rotors at all the downstream locations (Fig. 5.1(b)). A slight deviation can be observed at $x/R = 1$ as compared to other downstream locations (Fig. 5.1(c)). The maximum U^* occurs at $x/R = 1$, and minimum U^* is observed at $x/R = 2$ and *3* along the central axis, suggesting an improvement in flow recovery. At $y/R = +1.25$ and -1.25, the placement of model rotors affects U^* at the tips of each rotor blade with varying magnitudes at different downstream locations. With an increased wind speed, the U^* patterns in between the tip spacing become flatter from a round shape.

Bastankhah and Abkar, (2019) observed four high-velocity deficit zones in the near wake ($x/R = 4$) of the four-rotor system corresponding to the wakes of its individual rotors. In their study, the wakes of the several rotors started to mingle as the flow moves downstream resulting in a more even distribution of the entire wake. The velocity recovery for the four-rotor system started somewhat higher than the single-rotor due to local obstruction effects on the former at starting ($x/R = 4$). The four-rotor velocity recovers faster than the single-rotor up to around $x/R = 8$ at the rotor centre. Additionally, it has been shown that the double-rotor wake rebounds initially and more quickly than the single-rotor wake, but this quick recovery only lasts until the wakes of the double-rotor combine to create a single wake (Bastankhah and Abkar, 2019). Thus, one can expect quick recovery in the multirotor system within a certain region of interest, and because of this, the placement or integration of subsequent rotor can be proposed.

5.2.2.2 Vertical Plane Behaviour

The U^* profiles at different downstream locations and wind speeds are depicted in Fig. 5.2. At U_∞ = 3.55 m/s, the U^* is maximum at $x/R = 4$, and minimum at $x/R = 2$ along a vertical line of the central axis (Fig. 5.2(a)). This U^* has a range of -5% to 5%. At U_∞ = 4.55 m/s, the U^* is maximum at $x/R = 2, 3,$ and 4, and minimum at $x/R = 1$ along vertical line of the central axis (Fig. 5.2(b)). The U^* has a range of -8 to -1%. Finally, at U_∞ = 5.55 m/s, the U^* is maximum at $x/R = 4$, and minimum at $x/R = 2$ along a vertical line on the central axis (Fig. 5.2(c)). The U^* has a range of -6 to 0%. Thus, it has been observed that the velocity deficit becomes minimal when the tip spacing between the rotors is large. One of the interesting observations is that the deficit is minimal close to the rotor plane and maximum away from the plane. Such observation can be attributed to the interaction of expanding wake dissipating from the two model rotors.

5.2.3 Wake Characteristics at $T_S = 1.0R$

5.2.3.1 Horizontal Plane Behaviour

The effect of wind speed on velocity deficit at $T_S = 1.0R$ is shown in Fig. 5.3. At U_∞ = 3.55 m/s, the maximum U^* is found to be of about 20% (at $x/R = 2$) under low λ (Fig. 5.3(a)). The minimum U^* occurs at $x/R = 3$ and is about -10%. While in Fig. 5.3(b), it is difficult to find the location of maximum U^* at U_∞ = 4.55 m/s, however, the minimum U^* of about -10% to 0% is observed at $x/R = 3$. At $x/R = 2$, there is more non-axisymmetric pattern, while in other cases, the presence of nearly axis-symmetric deficit is observed about the central line axis. Further, there is a fluctuation of U^* at $x/R = 2$ and 3. Similarly, at U_∞= 5.55 m/s, the maximum U^* (at $x/R = 2$) of about 0 to 10% occurs in between the tip spacing (Fig. 5.3(c)). The minimum U^* of about -10% to 0% (at $x/R = 1$) in between the tip spacing. A lesser fluctuation of U^* occurs at $x/R= 1$ as compared to the ones at $x/R = 2$ and 3.

At the higher tip spacing ($T_S = 1.0R$) it has been observed that the deficit is quite significant (Fig. 5.3(a)), however, it becomes relatively stable at higher wind speeds (Fig. 5.3(b) and 5.3(c)). The primary reason of such behaviour lies with the faster recovery of downstream flow. At $x/R = 1$, the tip vortices only effect the flow behind the rotors' plane in between the tip spacing. At $x/R = 2$ and 3, the tip and root vortices affect the flow behind the rotors' plane in between the tip spacing. The tip vortices are found to be stronger than the root vortices, and this is the reason why the root vortices do not have the capacity to propagate in the downstream direction (> $3R$) but do affect in the region $2 < x/R < 3$.

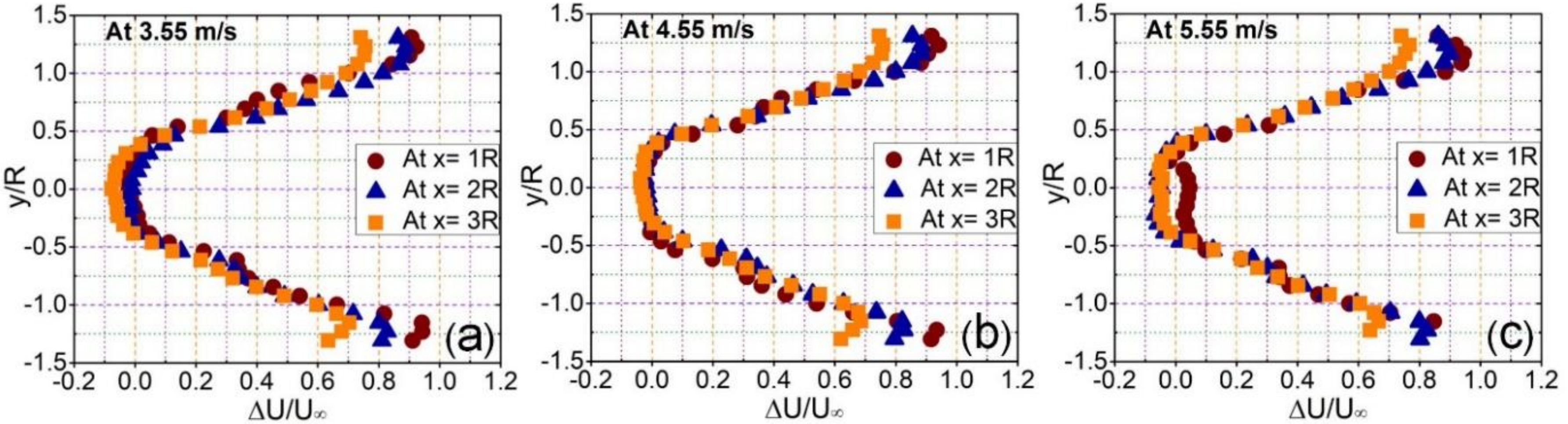

Fig. 5.1 Effect of wind speed on velocity deficit in horizontal plane of the double rotor arrangement at $T_S = 0.5R$ (a) at U_∞ = 3.55 m/s, (b) at U_∞ = 4.55 m/s and (c) at U_∞ = 5.55 m/s

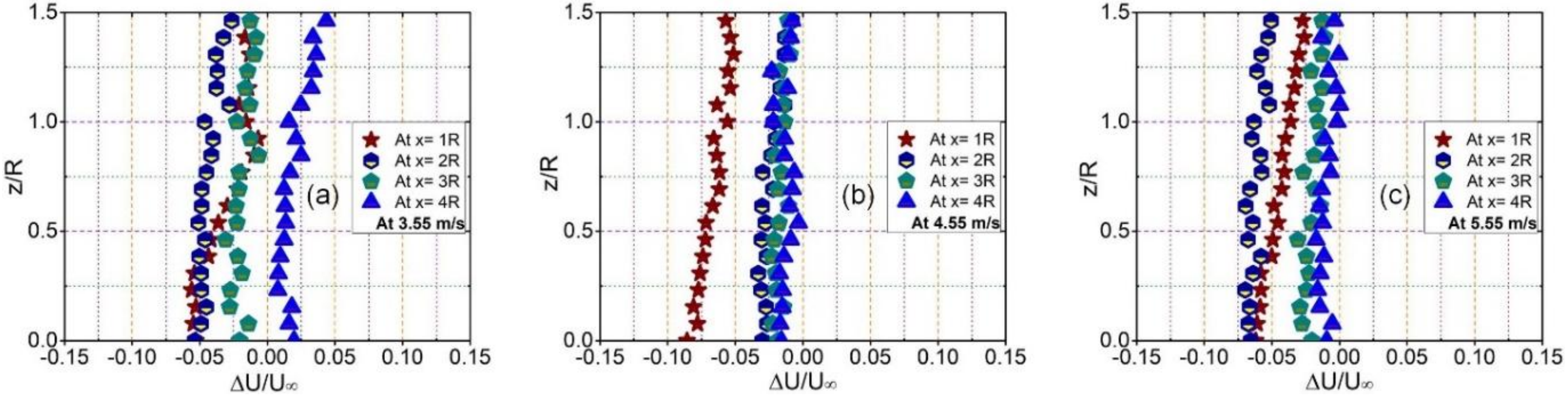

Fig. 5.2 Effect of wind speed on velocity deficit in vertical plane of the double rotor arrangement at $T_S = 0.5R$ (a) at U_∞ = 3.55 m/s, (b) at U_∞ = 4.55 m/s and (c) at U_∞ = 5.55 m/s

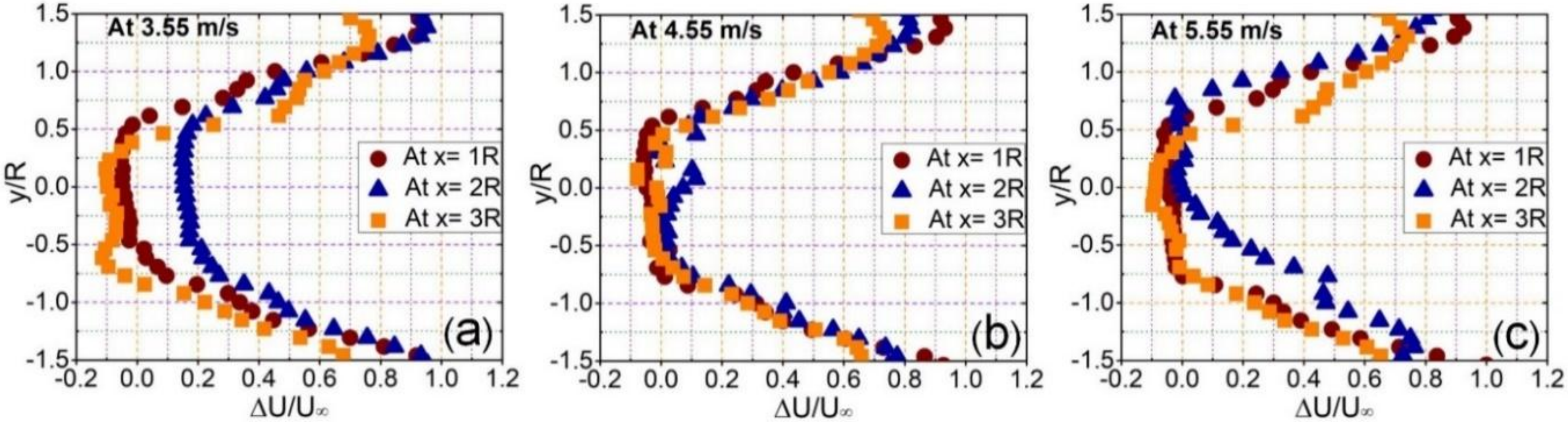

Fig. 5.3 Effect of wind speed on velocity deficit in horizontal plane of the double rotor arrangement (a) at U_∞ = 3.55 m/s, (b) at U_∞ = 4.55 m/s and (c) at U_∞ = 5.55 m/s

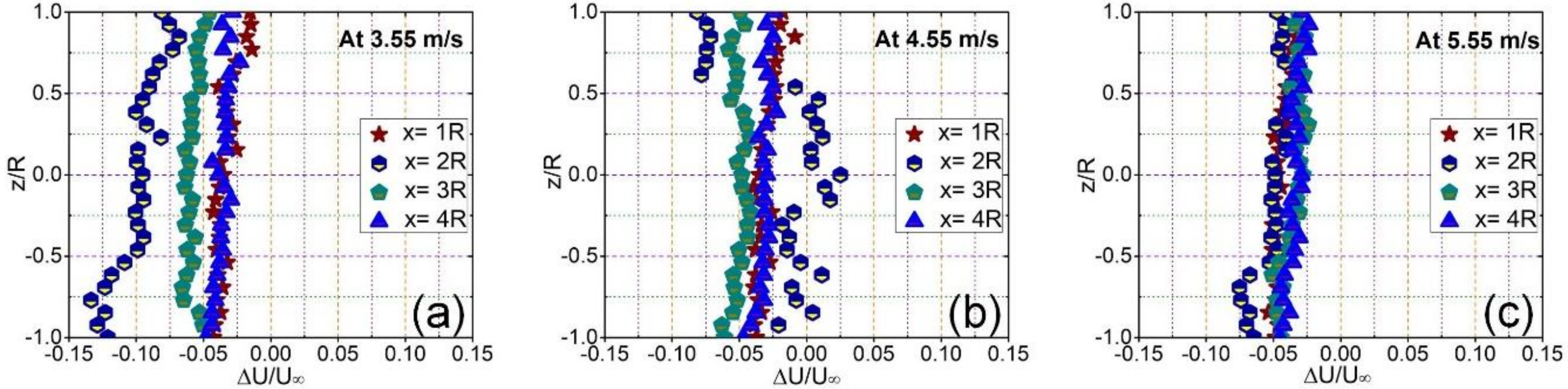

Fig. 5.4 Effect of wind speed on velocity deficit in vertical plane of the double rotor arrangement (a) at U_∞ = 3.55 m/s, (b) at U_∞ = 4.55 m/s and (c) at U_∞ = 5.55 m/s

5.2.3.2 Vertical Plane Behaviour

The U^* profiles at different downstream locations and wind speeds are depicted in Fig. 5.4. At $U_\infty = 3.55$ m/s, the U^* is maximum at $x/R = 4$ and minimum at $x/R = 2$ along a vertical line on the central axis (Fig. 5.4(a)). The U^* spans a range of approximately –10% to 5%, with noticeable asymmetry along the vertical direction. At $U_\infty = 4.55$ m/s, the U^* is maximum at $x/R = 2$, 3, and 4, and minimum at $x/R = 1$ (Fig. 5.4(b)). Here, the U^* range lies between –8% and –1%, showing progressive wake recovery with downstream distance. Finally, at $U_\infty = 5.55$ m/s, the U^* is maximum at $x/R = 4$ and minimum at $x/R = 2$ along the same vertical line (Fig. 5.4(c)), with the deficit range between –6% and 0%.

In both single and double-rotor arrangements, operation at low λ directly controls the observed wake dynamics and significantly changes the aerodynamic loading characteristics of the rotor blades. Over a significant portion of the blade span, the local angle of attack approaches or surpasses stall conditions due to the substantial increase in relative flow angle at the blade sections at low λ. This results in uneven blade loading, a lower lift-to-drag ratio, the beginning of flow separation, and unstable vortex shedding.

An enhanced and spatially non-uniform velocity deficit in the near wake is the direct result of these aerodynamic alterations. Through shear-layer instabilities and the rapid destabilisation of tip vortices, the increased separation and unstable loading encourage the formation of increased turbulence. Consequently, the higher turbulence accelerates momentum entrainment from the surrounding freestream, resulting in a comparably faster breakdown of coherent wake structures and an earlier commencement of wake recovery, even if the near-wake deficit gets deeper under low TSR operation.

Strong unsteady blade loading linked to low λ implies higher cyclic aerodynamic forces from a structural perspective, which can result in higher fatigue loading on the rotor, shaft, and support structures especially in closely spaced multi-rotor configurations where wake-induced turbulence is amplified. Unsteady load transfer and vibrational response may be exacerbated by fluctuating induction zones between adjacent rotors, as evidenced by observed wake asymmetry, vortex interaction, and intermittent recovery.

BEMT predictions for low λ operation is very qualitatively consistent with these experimental data. Under such circumstances, BEMT anticipates higher angles of attack, decreased aerodynamic efficiency, uneven axial induction, and greater unstable loads. Therefore, by offering comprehensive experimental insight into the downstream turbulence generation, wake recovery behaviour, and rotor–rotor interaction effects unique to small-scale multi-rotor systems, the current wake measurements both support and expand upon these theoretical trends.

5.3 Design Implications for Low TSR Operation

The results of this investigation highlight the critical role that rotor spacing plays in wake formation and recovery in double-rotor systems that operate at low λ. These aerodynamic effects are particularly significant in applications where optimising efficiency in low-wind conditions is crucial, such as tiny wind turbine systems and compact arrays.

The wakes produced by each rotor interact strongly in the near-wake area when the rotor spacing is minimal (e.g., $T_S = 0.5R$). This causes a delayed wake recovery downstream and noticeable velocity deficit, especially in the area between the rotors. In a wind farm setup, such strong wake merging may result in irregular flow patterns, which could strain downstream rotors unevenly. These flow anomalies may shorten the operating lifespan of turbine components by increasing mechanical fatigue and decreasing the downstream units' aerodynamic performance. Conversely, wake contact is greatly decreased by raising the rotor spacing to $T_S = 1.0R$. More symmetric wake structures, fewer velocity deficits, and an earlier flow recovery result from the two rotors starting to function more independently regarding aerodynamics. When increased turbulence promotes momentum exchange and speeds up wake dissipation at higher inflow velocities, this impact is most noticeable. The overall energy extraction capability is enhanced by the smoother wake profile, which also makes it easier to install more rotors downstream.

Under low λ circumstances, a minimum $T_S = 1.0R$ is recommended for constructing double and multi-rotor designs or closely spaced wind turbine arrays. This spacing strikes a compromise between the aerodynamic requirement of preserving adequate wake separation to reduce energy loss from wake overlap and the requirement for spatial compactness. The design process should also incorporate site-specific wind characteristics like directionality, turbulence intensity, and prevailing wind speed. To reduce wake-related performance losses, designers may use more conservative spacing or extra flow control techniques, including rotor staggering or yaw optimisation, in areas with consistently low wind speeds or extremely variable flow conditions.

Ultimately, the spacing plan must consider both aerodynamic efficiency and real-world limits, such as cost, structural restrictions, and land availability. In both stand-alone and grid-connected applications, the knowledge gained from this study lays the groundwork for improving rotor design in low λ wind systems, increasing energy yield and system longevity.

5.4 Summary of the Study

This chapter used point-wise velocity measurements to investigate the aerodynamic behaviour of a side-by-side double-rotor horizontal-axis wind turbine system operating under low λ conditions. The findings showed that wake interactions and recovery dynamics are significantly impacted by rotor spacing. More profound velocity deficits and delayed flow re-energisation resulted from the wake interaction between rotors being especially significant in the horizontal plane at a reduced tip spacing of $T_S = 0.5R$. On the other hand, these effects were greatly reduced by raising the rotor spacing to $T_S = 1.0R$, which led to earlier recovery downstream and smoother, more symmetric wake profiles. With greater spacing and higher wind speeds, vertical wake behaviour much improved, but at close spacing, it recovered more slowly and was less sensitive to inflow velocity. Higher inflow velocities were shown to speed wake dissipation and improve turbulence mixing in both planes, particularly at the wider spacing. Together, these results demonstrate that inflow velocity and rotor closeness are essential factors affecting wake formation when operating at low λ. The aerodynamic optimisation of compact wind turbine design requires understanding these connections, especially in small-scale systems where performance and dependability depend heavily on efficiency and flow quality.

CHAPTER 6

AERODYNAMIC DESIGN AND TESTING

6.1 Introductory Remark

O optimising rotor performance and layout efficiency requires understanding the aerodynamic behaviour of wind turbine wakes, especially in MRSs where wake interference can significantly impact energy harvest. The aerodynamic testing results of small HAWT configuration with two rotors positioned side by side are presented in this chapter. The study uses surface plots of normalised velocity deficit obtained from wind tunnel observations to characterise the wake flow.

Three inflow velocities U_∞ = 3.55 m/s, 4.55 m/s, and 5.55 m/s, and two rotor tip spacings, corresponding to rising λ, were investigated experimentally. A hot-wire anemometer was used to obtain wake data in horizontal and vertical planes, with the origin placed halfway between the rotor tip at hub height. The chapter is set up to look into:

- First wake development over tip-speed ratio and tip spacing;
- Aerodynamic interaction between rotors and wake merging behaviour;
- Variations between the horizontal and vertical axes of wake development;
- The impact of inflow velocity on recovery and wake structure;
- Consequences for turbine array design and aerodynamic performance.

The subsequent sections offer a thorough analysis of the wake flow behaviour utilising area-integrated velocity deficit data and 2D surface plots, offering crucial information about the double-rotor configuration's aerodynamic performance.

6.2 Wake Formation and Initial Structure

An outline of the wake structure produced by the double-rotor wind turbine system directly downstream of the rotor plane is given in this section. The initial wake formation significantly influences energy recovery, turbulence production, and future flow development. Normalised velocity deficit (U^*) surface plots provide a spatial representation of wake expansion and flow slowing in both the horizontal and vertical planes.

6.2.1 Wake Structure at Closer ($T_S = 0.5R$) in Horizontal and Vertical Planes

Two distinct regions of velocity deficit are evident behind each rotor as shown in Fig. 6.1, indicating dual wake structures beginning to interact. The lateral spread of the wake in the *y/R* direction reveals moderate expansion, suggesting some degree of aerodynamic interference between the rotors. The streamwise direction (*x/R*) shows a gradual recovery of velocity, though the deficit remains significant up to *x/R = 4*, implying slower wake re-energisation at this lower tip speed ratio. The wake appears symmetric mainly about the centreline, which indicates balanced rotor loading and minimal yaw effects. The relatively broad and merged deficit zone implies overlapping shear layers and increased turbulence generation, typical of closely spaced rotor configurations. This figure highlights the impact of lower λ on wake development characterised by wider, less concentrated wakes and delayed velocity recovery.

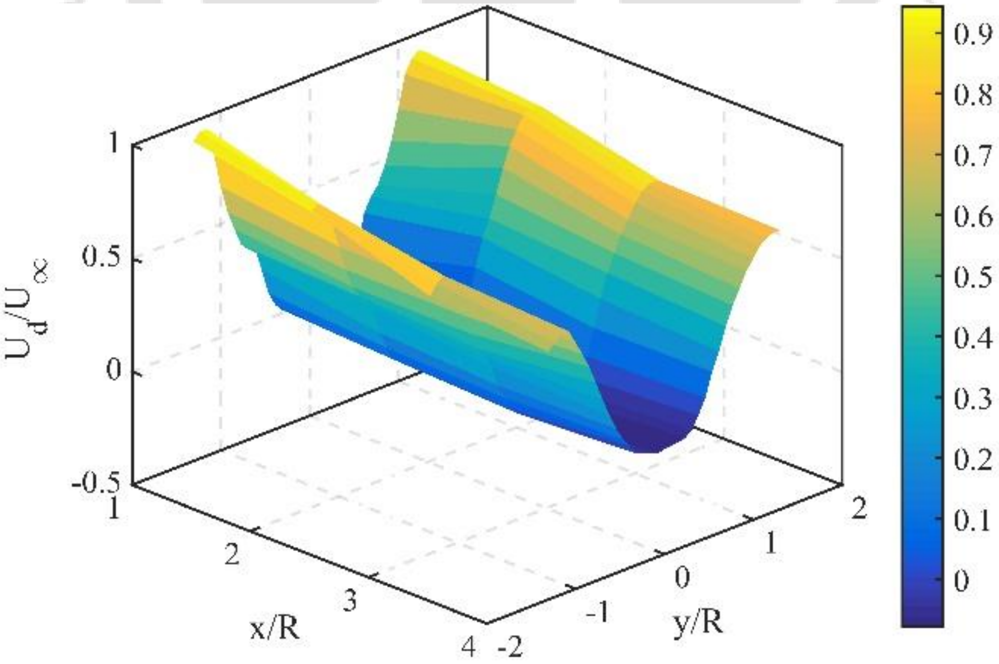

Fig. 6.1 Surface plot of U^* at $U_\infty = 3.55$ m/s in horizontal plane for $T_S = 0.5R$

Compared to the lower velocity case, the wake regions appear more confined laterally, and the minimum deficit values are deeper, indicating stronger energy extraction by the rotors at this higher λ as shown in Fig. 6.2. The two wake cores remain identifiable but exhibit greater overlap, suggesting an increase in rotor-rotor aerodynamic interference. Along the streamwise direction (x/R), the deficit shows a smoother gradient with signs of faster velocity recovery beyond $x/R = 3$. The central merging zone between the two wakes is more pronounced, indicating intensified mixing due to reduced spacing and increased rotor-induced turbulence. Overall, the plot demonstrates that increasing inflow velocity enhances the coherence and sharpness of the wake, but also amplifies the aerodynamic interaction in close-spacing configurations.

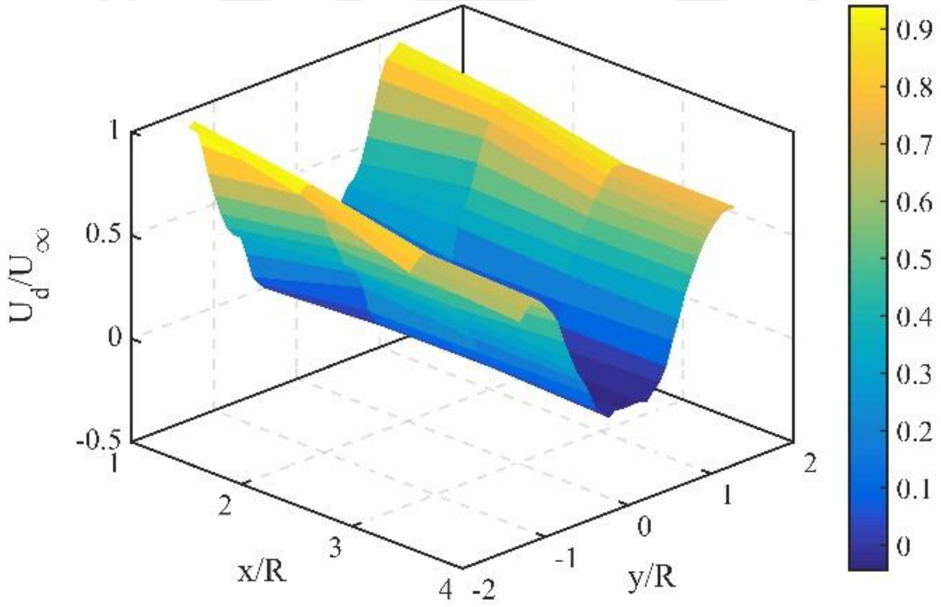

Fig. 6.2 Surface plot of U^* at $U_\infty = 4.55$ m/s in horizontal plane for $T_S = 0.5R$

At this higher inflow velocity corresponding to the highest λ in the study the wake structures become significantly narrower and more defined. The deficit cores are deeper and exhibit sharper gradients in both x/R and y/R as shown in Fig. 6.3, indicating more intense energy extraction and stronger rotor-induced flow deceleration. While the two wake regions remain individually discernible, the central merging zone has grown more prominent and turbulent, revealing a higher degree of aerodynamic interaction due to both the increased rotational speed and the close rotor spacing. Additionally, the streamwise progression shows signs of faster velocity recovery beyond $x/R = 2$, a result of enhanced turbulent mixing. This plot highlights the competing effects of higher λ: increased rotor performance and wake coherence, but also intensified rotor-rotor interference in compact configurations.

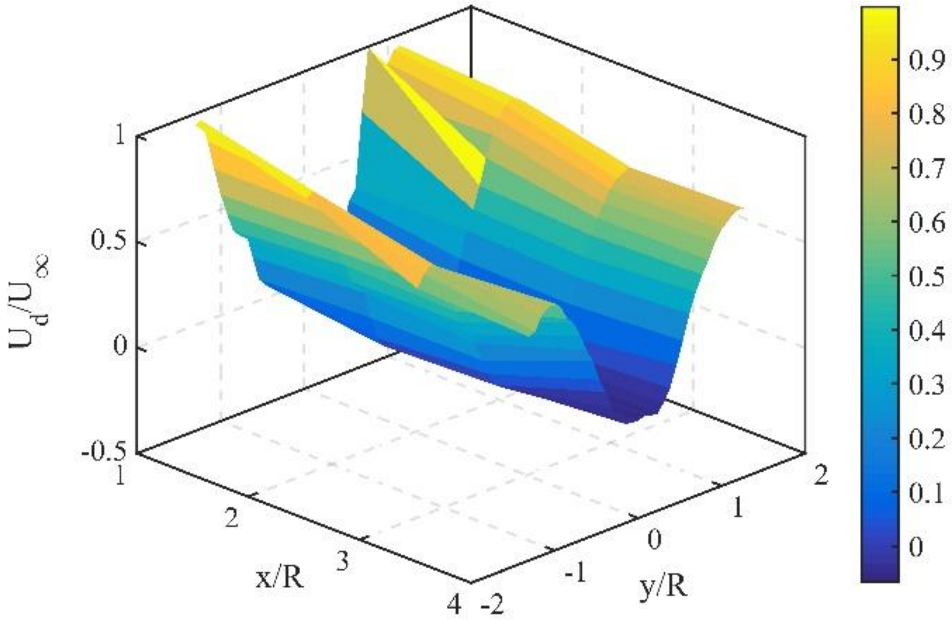

Fig. 6.3 Surface plot of U^* at $U_\infty = 5.55$ m/s in horizontal plane for $T_S = 0.5R$

The plot reveals a vertically symmetric wake structure cantered around the hub height as shown in Fig. 6.4, which corresponds to *z/R = 0*. The velocity deficit is modest in magnitude at this lower inflow speed, and the deficit region spreads broadly in the vertical direction. The wake appears to expand significantly with downstream distance (*x/R*), indicating limited energy extraction and weak momentum confinement. The smooth and gradual contours suggest that turbulence and mixing are relatively low under this condition. Overall, the figure characterizes an early-stage wake with minimal interference and low aerodynamic loading serving as a baseline for evaluating how increased speed or spacing affects wake behaviour vertically.

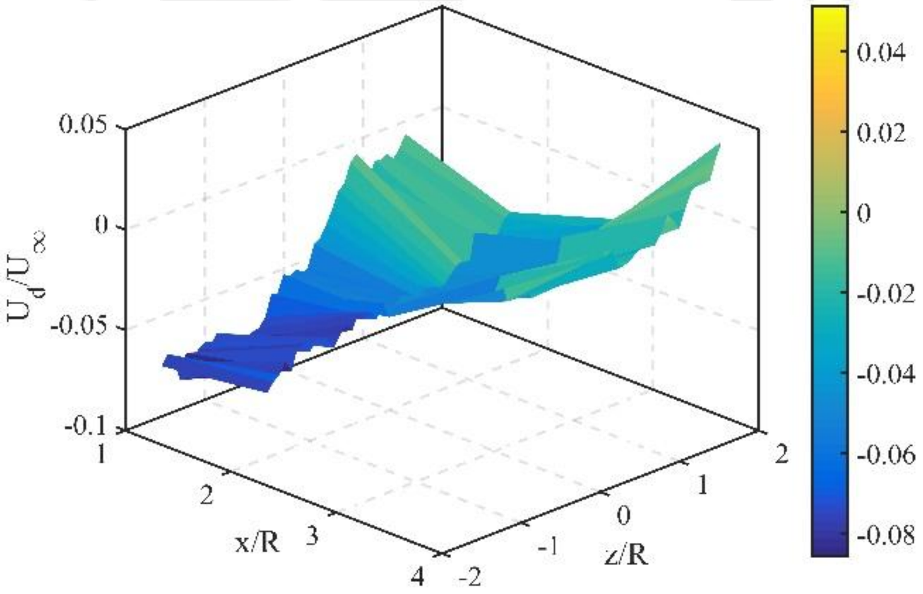

Fig. 6.4 Surface plot of U^* at $U_\infty = 3.55$ m/s in vertical plane for $T_S = 0.5R$

Compared to the U_∞ = 3.55 m/s case as shown in Figure 6.5, the wake exhibits a more concentrated deficit zone around the hub height, with steeper gradients along the vertical direction (*z/R*). The deficit reaches deeper minima and extends farther downstream, indicating enhanced energy extraction and stronger wake confinement due to the increased λ. Additionally, the flow recovers more quickly beyond *x/R* = *3*, as evidenced by the gradual slope of the surface, suggesting improved turbulent mixing. The symmetry of the wake about *z/R* = *0* remains evident, indicating balanced rotor performance. The plot captures the transition from a diffuse to a more focused and energetic wake, consistent with increased aerodynamic loading and interaction between the vertically spreading wakes of both rotors.

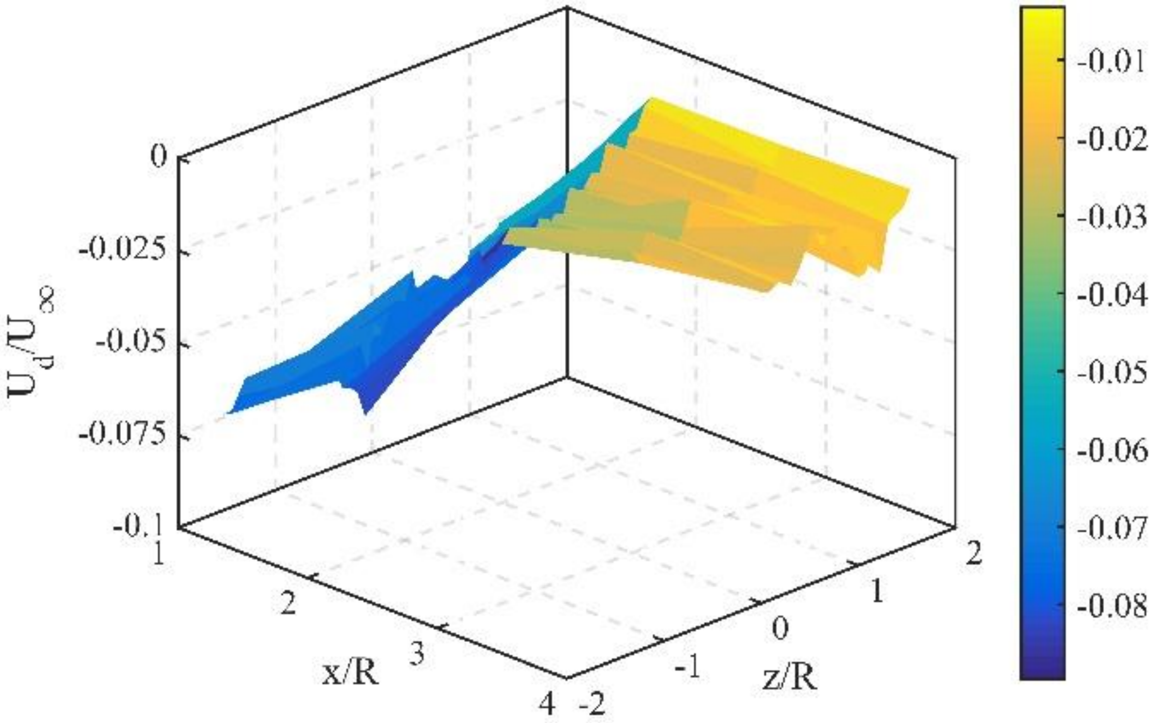

Fig. 6.5 Surface plot of U^* at $U_\infty = 4.55$ m/s in vertical plane for $T_S = 0.5R$

The wake structure is sharply defined as shown in Figure 6.6, with a deep and concentrated deficit region cantered around the hub height (*z/R* = 0). The vertical spread of the wake is narrower compared to the lower velocity cases, indicating stronger flow confinement and enhanced aerodynamic loading at the highest tested λ. The streamwise evolution along *x/R* shows a well-formed recovery gradient, with the deficit beginning to attenuate beyond *x/R* = *3*. The wake exhibits vertical symmetry and pronounced axial stretching, characteristic of efficient energy extraction with limited turbulent diffusion. This figure confirms that increased λ not only intensifies the wake but also leads to faster recovery due to elevated rotor-induced mixing and organized flow structures.

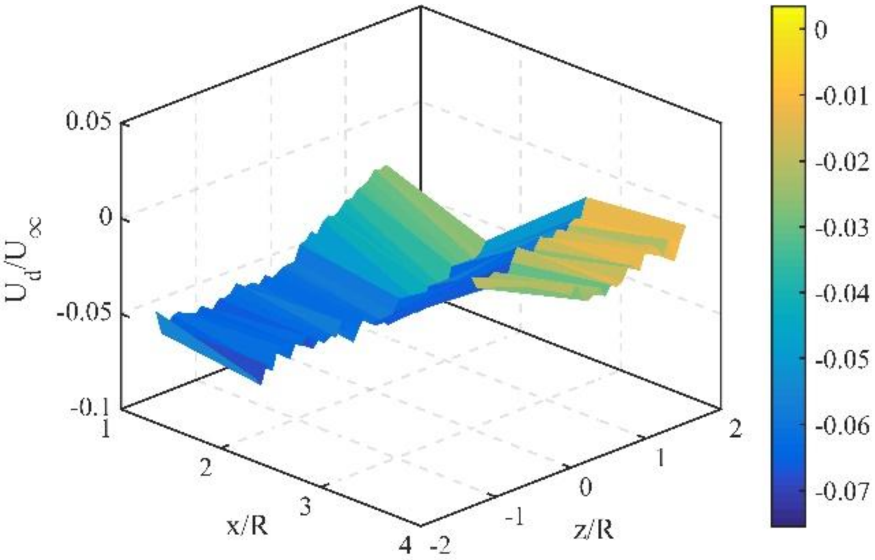

Fig. 6.6 Surface plot of U^* at $U_\infty = 5.55$ m/s in vertical plane for $T_S = 0.5R$

6.2.2 Wake Structure at Wider (T_S= *1.0R*) in Horizontal and Vertical Planes

In contrast to the *Ts = 0.5R* case, the two wake cores appear clearly separated as shown in Fig. 6.7, with minimal overlap in the central region. This spatial separation leads to a more symmetric and stable wake pattern along the lateral direction (*y/R*), with reduced aerodynamic interference between the rotors. The deficit zones are broader but shallower compared to higher λ cases, reflecting lower energy extraction and weaker wake confinement at this lower inflow velocity. Downstream progression along *x/R* shows a gradual recovery, with moderate steepness in the recovery gradient. The figure effectively demonstrates how increasing rotor spacing at a given λ minimizes wake merging and fosters independent wake evolution an important consideration for optimizing double-rotor turbine layout.

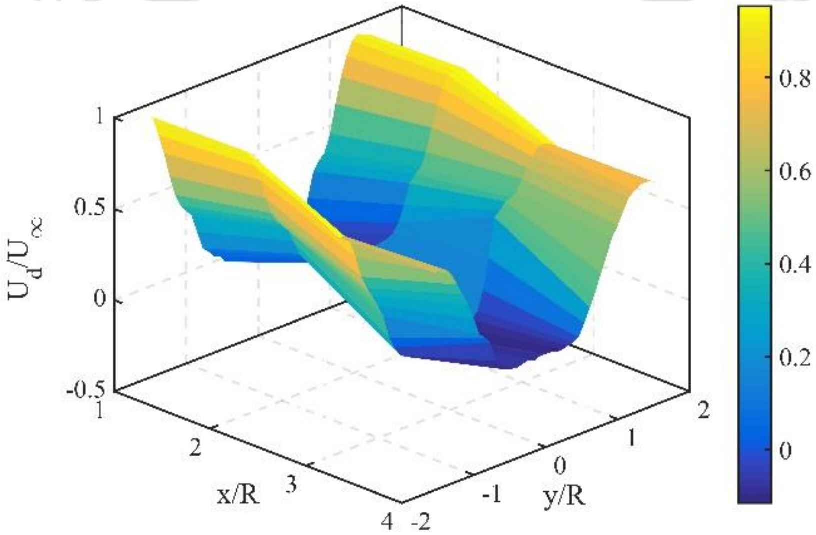

Fig. 6.7 Surface plot of U^* at $U_\infty = 3.55$ m/s in horizontal plane for T_S = *1.0R*

The two wake cores remain distinctly separated along the lateral direction (*y/R*) as shown in Fig. 6.8, demonstrating minimal aerodynamic interaction between the rotors. The deficit zones are deeper and more focused compared to the lower-speed case, indicating enhanced energy extraction due to the higher λ. However, the wider rotor spacing helps preserve individual wake identities and delays merging, which contrasts with the stronger overlap observed at *Ts* = *0.5R*. Streamwise evolution along *x/R* reveals steady velocity recovery, with more pronounced gradients suggesting improved downstream mixing and entrainment. The plot highlights the aerodynamic advantage of increased spacing in reducing wake interference, even at moderately high operating speeds.

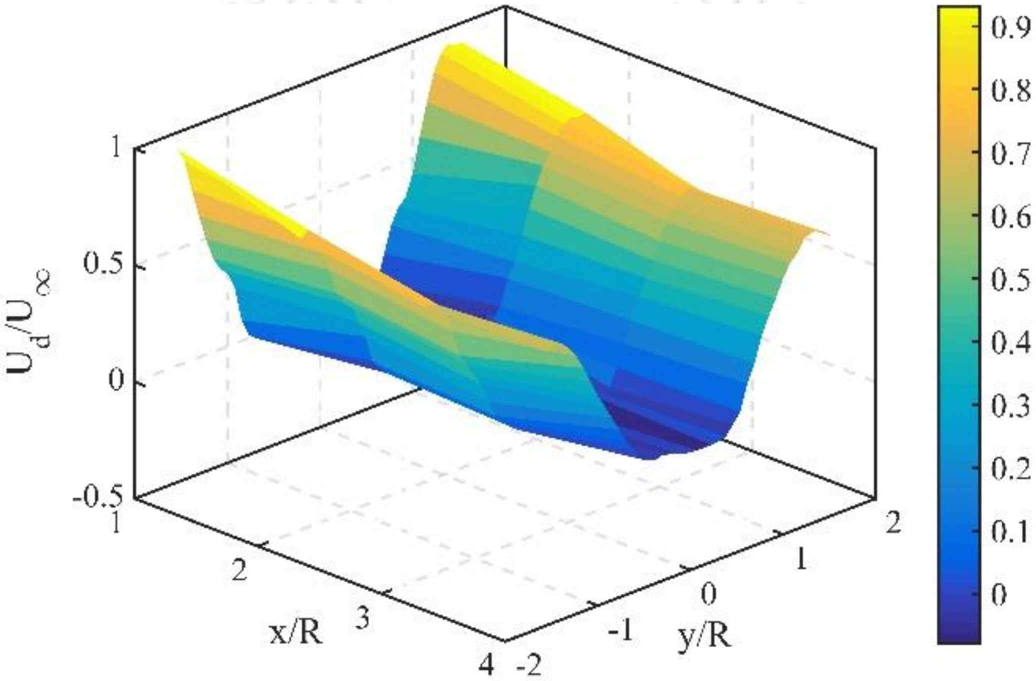

Fig. 6.8 Surface plot of U^* at U_∞ = 4.55 m/s in horizontal plane for T_S = *1.0R*

At this highest inflow velocity, corresponding to the maximum λ tested as shown in Fig. 6.9, the wake cores are distinctly defined and symmetrically placed about the centreline (*y/R*= *0*). The deficit regions are deep and narrow, indicating strong energy extraction by each rotor. Despite the increased rotor activity, the wider spacing effectively minimizes wake interference, preserving the identity of each wake and preventing premature merging. The streamwise evolution along *x/R* shows a sharper recovery slope compared to the lower velocity cases, reflecting more efficient turbulent mixing and re-energization of the flow. This plot reinforces the aerodynamic benefits of increased spacing in double-rotor systems, particularly at higher operating speeds, where performance gains are maximized without introducing excessive wake interaction.

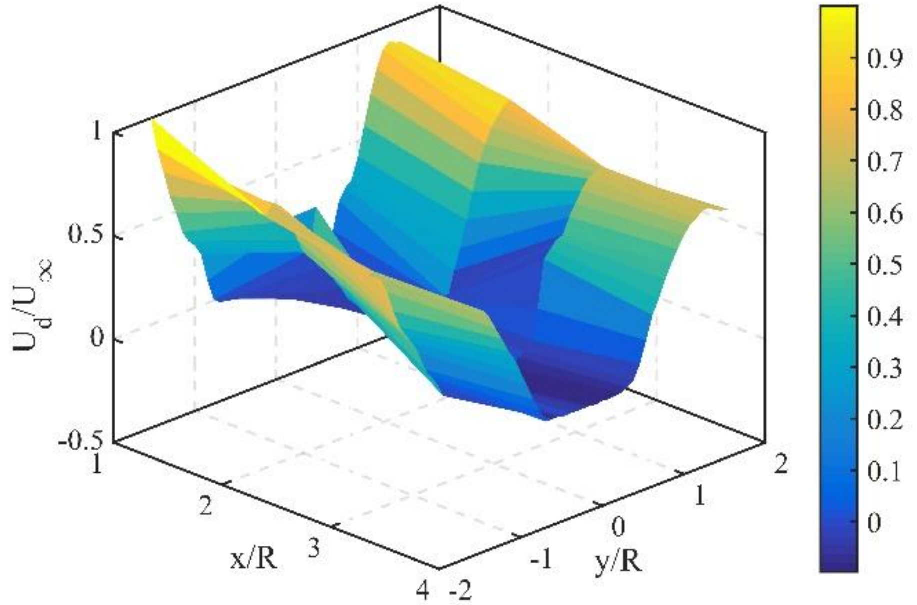

Fig. 6.9 Surface plot of U^* at U_∞ = 5.55 m/s in horizontal plane for $T_S = 1.0R$

The wake structure is relatively diffuse and vertically expanded, with shallow deficit values that indicate moderate energy extraction at this lower λ. The symmetry of the wake about the hub height ($y/R = 0$) is maintained, while the flow field shows minimal steep gradients suggesting limited turbulent mixing and slow recovery as shown in Fig. 6.10. Compared to the closer spacing case, the wider tip spacing appears to reduce vertical overlap and aerodynamic interference between the rotors, allowing for more independent wake development. The broader, low-intensity wake also indicates that the flow has sufficient space to expand vertically without strong rotor-rotor interaction. This figure serves as a baseline for comparison with higher inflow velocities where more dynamic vertical wake behaviour is expected.

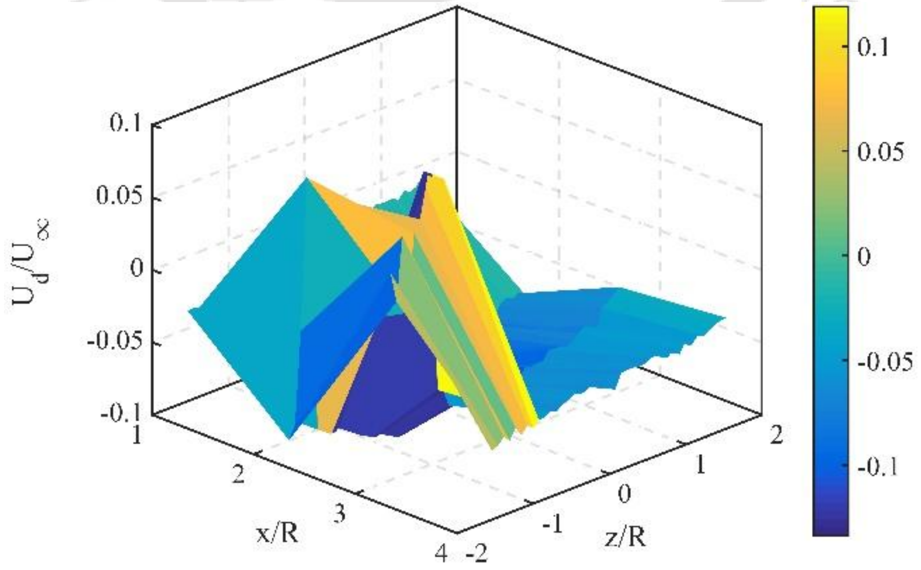

Fig. 6.10 Surface plot of U^* at U_∞ = 3.55 m/s in vertical plane for $T_S = 1.0R$

The plot illustrates the downstream wake evolution from the rotor plane ($x/R = 1$ to 4) and shows a symmetric distribution of the wake about the vertical axis ($y/R = 0$) as shown in Fig. 6.11, consistent with the symmetrical rotor arrangement. A distinct velocity deficit region is observed near the hub height around $x/R \approx 2–3$, indicating the core of the wake. Slight positive values in the centre suggest localized acceleration, possibly due to wake entrainment and partial recovery. As the flow progresses downstream, the deficit weakens, indicating gradual wake recovery. The symmetry and limited wake interaction reflect the minimal interference between the rotors at this larger spacing.

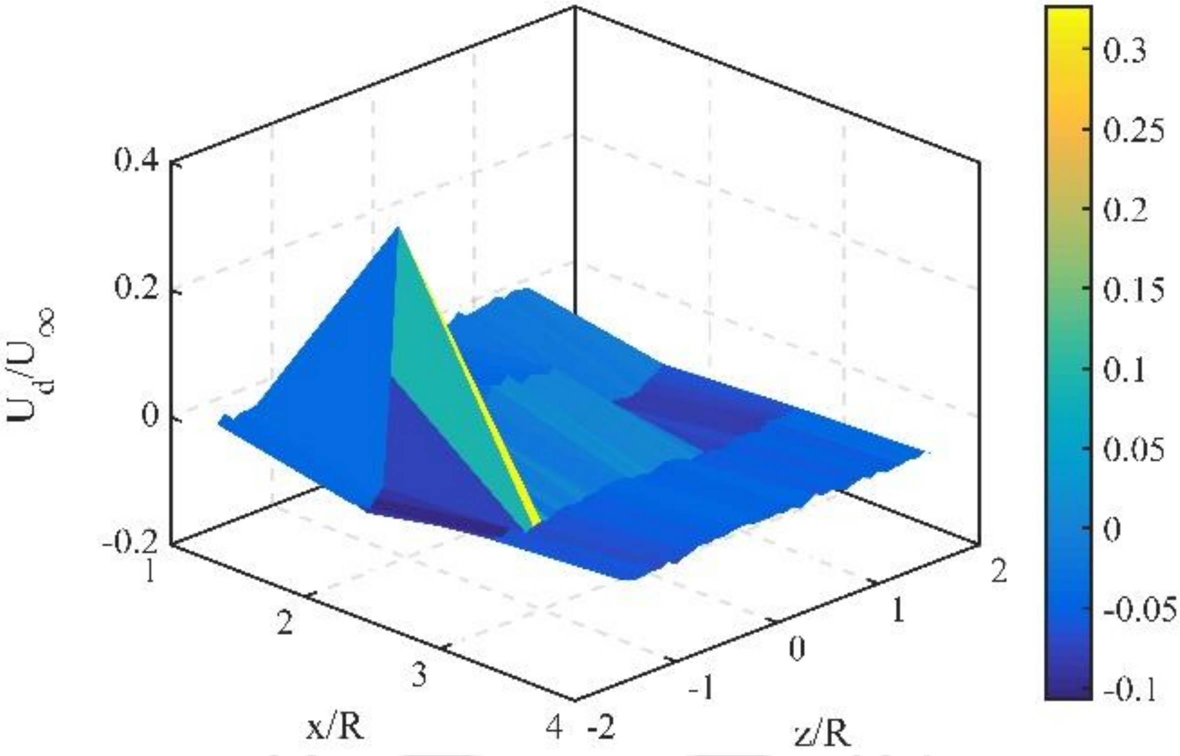

Fig. 6.11 Surface plot of U^* at $U_\infty = 4.55$ m/s in vertical plane for $T_S = 1.0R$

The wake profile retains its symmetry about the vertical axis ($z/R = 0$) as shown in Fig. 6.12, indicating consistent rotor operation and minimal vertical interference. The peak velocity deficit is observed around $x/R \approx 2.5$, similar to the lower-speed case, but the magnitude is reduced, suggesting faster wake recovery at higher wind speeds. The wake region appears more uniform and flattened in the downstream sections, indicating enhanced mixing and reduced influence of individual rotor wakes. Overall, the plot demonstrates that at $T_S = 1.0R$, increasing the inflow velocity promotes earlier and smoother wake dissipation.

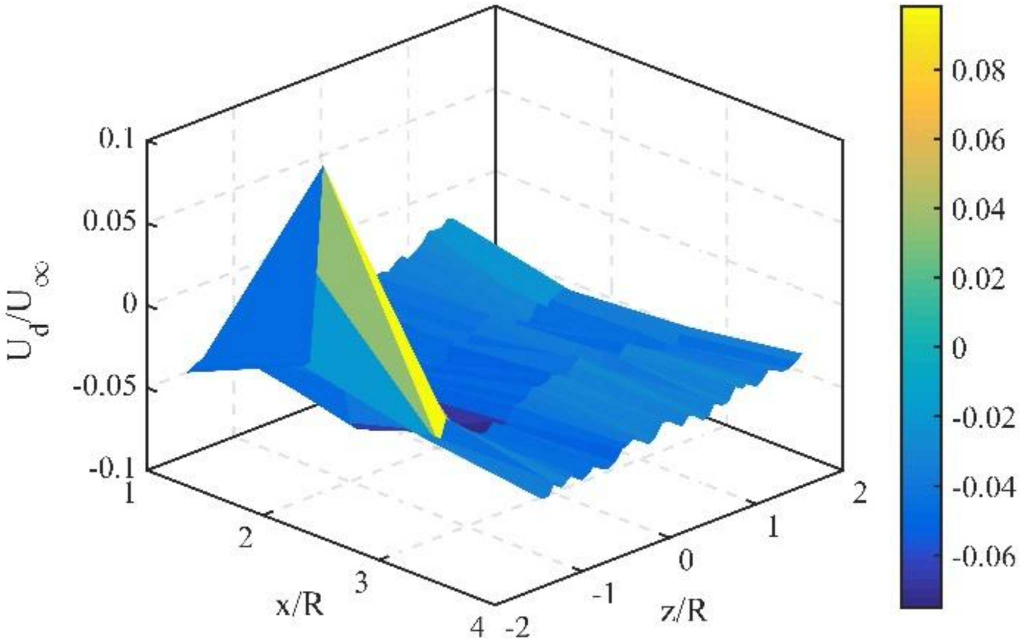

Fig. 6.12 Surface plot of U^* at $U_\infty = 5.55$ m/s in vertical plane for $T_S = 1.0R$

6.3 Wake Interaction and Recovery Analysis

This section presents a detailed analysis of the area-integrated velocity deficit (AIVD) in both horizontal and vertical planes for the double-rotor configuration at two different rotor spacing conditions: $Ts = 0.5R$ and $Ts = 1.0R$. AIVD is calculated on the basis of equation 3.9 in discrete manner for local point in horizontal and vertical planes. The objective is to evaluate how rotor proximity and inflow velocity influence wake interaction, merging behaviour, and recovery characteristics in the near and far wake regions.

6.3.1 Horizontal Wake Interaction at Closer $T_S = 0.5R$

Across all velocities, the integrated deficit deepens from $x/R = 1$ to 3, indicating progressive wake development and interaction between closely spaced rotors. The greatest deficit is seen at $x/R = 3$, particularly for the lowest wind speed, reflecting limited recovery under low turbulence conditions, where wake merging and interference are strongest. The wake partially recovers by $x/R = 4$, especially at higher wind speeds. Notably, the $U_\infty = 5.55$ m/s case shows the shallowest initial deficit but exhibits more fluctuation, suggesting complex mixing behaviour due to higher kinetic energy in the flow. This trend highlights how reduced tip spacing enhances wake interaction and delays recovery, especially in the near-wake region as shown in Fig. 6.13.

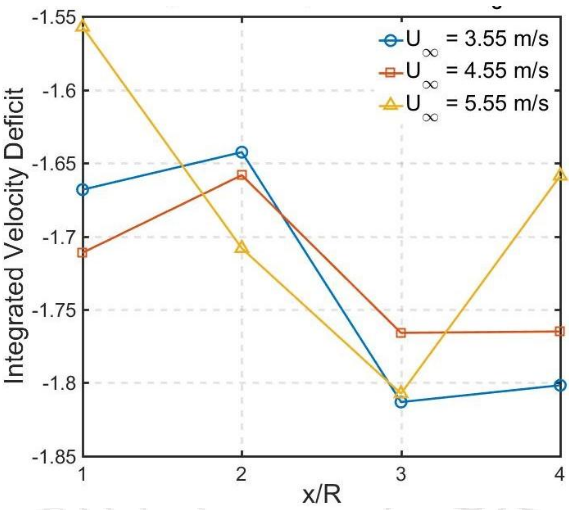

Fig. 6.13 Area-Integrated velocity along downstream at $T_S = 0.5R$ in horizontal plane

6.3.2 Vertical Wake Interaction at Closer $T_S = 0.5R$

The plot reveals a consistent trend across all wind speeds, with the highest integrated deficit observed between $x/R = 1$ and 2, indicating strong vertical wake confinement and limited vertical mixing in the near wake. A sharp recovery occurs between $x/R = 2$ and 3, followed by a plateau, suggesting that significant vertical wake recovery takes place by $x/R = 3$. The close similarity among all three curves indicates that, unlike the horizontal wake behaviour, the vertical integrated deficit is less sensitive to changes in inflow velocity at this close rotor spacing. This reflects that wake interference in the vertical direction remains strong and consistent, dominated by rotor proximity rather than flow speed as shown in Fig. 6.14.

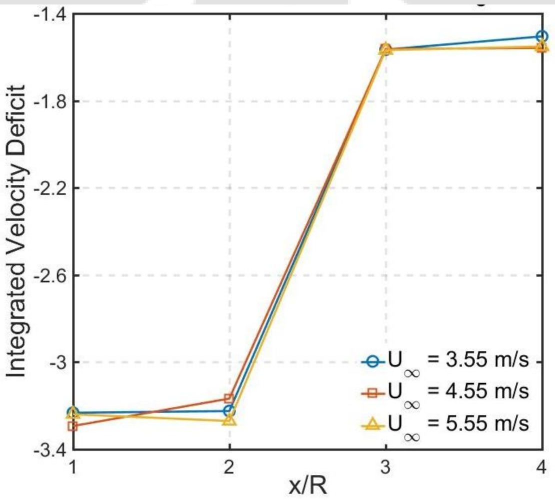

Fig. 6.14 Area-Integrated velocity along downstream at $T_S = 0.5R$ in vertical plane

6.3.3 Horizontal Wake Interaction at Wider $T_S = 1.0R$

Unlike the closer spacing case, the wake behaviour here shows more stable and consistent recovery trends. The 3.55 m/s case exhibits a noticeable peak at $x/R = 2$, possibly due to enhanced lateral wake interaction or turbulence spreading. However, at higher velocities (4.55 and 5.55 m/s), the integrated deficit values remain nearly identical, indicating minimal variation and faster stabilization of the wake. The overall smoother and flatter trend compared to the *Ts = 0.5R* case confirms that increased rotor spacing reduces aerodynamic interference and leads to more uniform wake development in the horizontal direction as shown in Fig. 6.15.

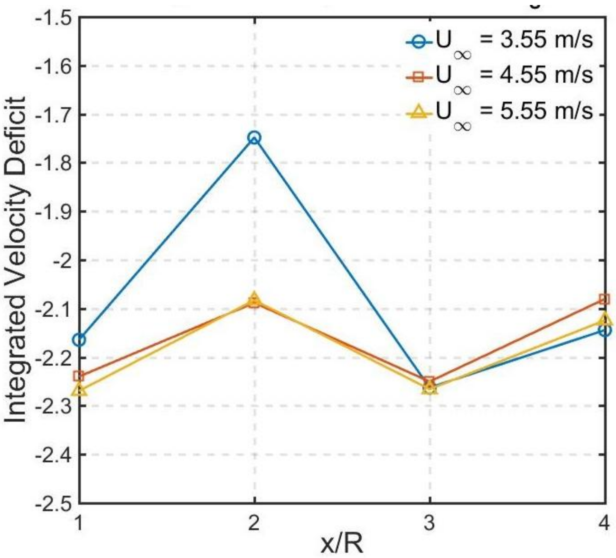

Fig. 6.15 Area-Integrated velocity along downstream at $T_S = 1.0R$ in horizontal plane

6.3.4 Vertical Wake Interaction at Wider $T_S = 1.0R$

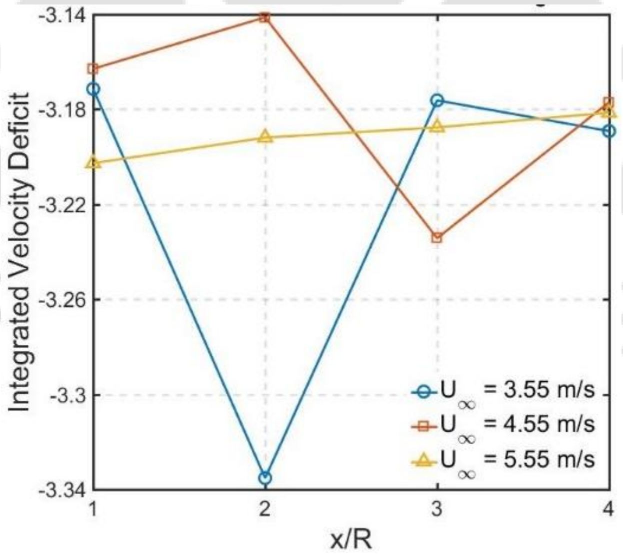

Fig. 6.16 Area-Integrated velocity along downstream at $T_S = 1.0R$ in vertical plane

The plot shows a significant dip in deficit at *x/R = 2* for the 3.55 m/s case, indicating strong vertical wake interaction and limited recovery at lower wind speeds. In contrast, the U_∞ = 4.55 and 5.55 m/s cases exhibit smoother trends with reduced overall deficit and more uniform wake recovery downstream. This suggests that higher inflow velocities promote faster vertical wake mixing and reduce the persistence of wake effects. The variability seen at lower velocity highlights the greater sensitivity of vertical wake dynamics to rotor-induced flow structures when spacing is moderate as shown in Fig. 6.16.

6.4 Effect of Tip Spacing on Wake Structure and Recovery

The rotor tip spacing largely determines the degree of aerodynamic interference between neighbouring rotors in a double-rotor wind turbine system. To evaluate their effects on wake merging, flow distortion, and recovery behaviour, two spacing configurations were investigated in this study: $T_S = 0.5R$ (closer tip spacing) and $T_S = 1.0R$ (wider tip spacing).

The surface plots in the horizontal and vertical planes (Figs. 6.1–6.6) in the $T_S = 0.5R$ configuration demonstrate a considerable wake overlap between the two rotors, especially at higher inflow velocities. Because of the rotors' proximity, shear layers merge, increasing turbulence, causing more profound combined velocity deficits, and delaying wake recovery. Strong aerodynamic coupling is suggested by this interaction, which is visible in the core region's vertical stretching and the lateral wake distortion in horizontal maps.

In contrast, the rotor wakes in the $T_S = 1.0R$ configuration (Figs. 6.7–6.12) remain substantially independent. The wakes' spatial separation lessens mutual interference, which produces smoother flow fields, less turbulent mixing in the centre, and a quicker recovery of downstream velocity. The deeper and better-defined individual deficit cores show more effective and less disrupted energy extraction. Vertical wake growth becomes more limited and symmetrical, particularly at higher λ.

Wider tip spacing reduces aerodynamic interference between rotors, as these measurements verify. From the standpoint of a compact layout, close spacing can be ideal; however, wake interaction reduces aerodynamic performance. The findings support the necessity of striking a compromise between flow stability and rotor proximity in multi-rotor wind turbine systems.

In addition to demonstrating significant aberrations resulting from low *Re* aerodynamics and rotor-rotor interaction effects, the wake recovery behaviour reported in the current tests can be usefully explained within the framework of traditional wake-growth and self-similarity theories. In traditional momentum-deficit-based wake models, the centreline velocity deficit decays according to a self-similar scaling controlled by momentum conservation, whereas the wake width is predicted to rise roughly linearly with downstream distance due to turbulent diffusion. These presumptions form the basis for popular analytical methods used in predicting wake recovery.

The current observations of transverse wake spreading and area-integrated velocity deficit show qualitative agreement with this conventional framework, particularly in the far-wake domain, where turbulent mixing predominates, and the impact of organised vortex structures diminishes. However, apparent deviations from perfect self-similarity are seen in the near- and intermediate-wake areas. The prolonged persistence of coherent tip-vortex structures typical of small-scale rotors and increased viscous diffusion at low Reynolds numbers are the leading causes of these discrepancies. Thus, in the early phases of wake generation, wake contraction and recovery do not adhere to the assumptions of completely equilibrium turbulence.

Substantial mutual interference between neighbouring shear layers and overlapping induction zones results in increased turbulence generation and faster wake spreading in the closer spacing configuration ($T_S = 0.5R$). Despite an initially deeper velocity deficit, the quick disintegration of coherent tip vortices in this regime encourages increased momentum entrainment from the surrounding freestream, resulting in an earlier wake recovery. Wider spacing ($T_S = 1.0R$), on the other hand, allows for greater preservation of the vortex core and delays complete wake merger and recovery, as partial reconstruction of the individual rotor wakes occurs before collision.

The balance between turbulence-driven diffusion and coherent vortex-induced transport is further reflected in the spatial evolution of wake symmetry seen under various spacing conditions. Asymmetric vortical interactions at closer spacing dominate the early wake region, while classical turbulent diffusion drives the recovery process more slowly at broader spacing. These findings verify that two mechanisms drive wake recovery in tiny multi-rotor systems: turbulence-dominated self-similar diffusion in the distant wake and coherent-structure-controlled transport in the close wake.

6.5 Comparative Analysis of Rotor Spacing Effects

The wake interaction and recovery behaviour presented in the previous sections highlight significant differences between the two rotor spacing configurations: $Ts = 0.5R$ and $Ts = 1.0R$. This section provides a comparative assessment of how tip spacing influences wake merging, turbulence intensity, and recovery efficiency in both horizontal and vertical planes.

6.5.1 Comparison Across Planes

The three-dimensional character of the flow field downstream of the double-rotor system can be better understood by comparing the wake behaviour in the horizontal and vertical planes cross-sectionally. Both planes emphasise distinct physical principles of flow initiation and recovery but highlight important wake formation characteristics. Wake profiles' side-by-side arrangement in the horizontal plane makes them more susceptible to rotor-rotor interaction. The wakes from each rotor combine laterally with closer tip spacing ($Ts = 0.5R$), which causes interference effects and unbalanced flow patterns close to the centre axis. The overlap is still noticeable at low spacing, but the wake cores get more defined and narrower as the inflow velocity rises. The horizontal plane displays separated wakes with little interference at wider tip spacing ($Ts = 1.0R$).

The wakes are typically symmetrical about the hub height in the vertical plane. These profiles reflect the vertical extension and dissemination of the deficiency region. More substantial rotational effects and improved axial momentum extraction cause the wake to become more limited in the vertical direction as λ increases, particularly at higher velocities. Additionally, the vertical plane makes it easier to see where the peak shortfall is and how deep the wake is. The vertical plane generally promotes confinement, symmetry, and axial wake recovery, whereas the horizontal plane stresses lateral interaction and wake merging between rotors. A more thorough knowledge of how tip spacing and λ affect the aerodynamic performance of MRSs is possible when both viewpoints are combined.

6.5.2 Wake Deficit Magnitude and Evolution

At $Ts = 0.5R$, the wakes from the two rotors are in close proximity, leading to pronounced interference effects. This is particularly evident in the horizontal plane (Fig. 6.13), where the area-integrated velocity deficit increases downstream up to $x/R = 3$, indicating strong wake merging. In contrast, the same horizontal metric at $Ts = 1.0R$ (Fig. 6.15) shows a more subdued deficit, with smoother profiles across all velocities, suggesting less interaction and more independent wake development. In the vertical direction, while both spacing configurations exhibit wake confinement near the hub height, the deficit profiles show different sensitivities to inflow velocity. For $Ts = 0.5R$, vertical deficits (Fig. 6.14) are nearly identical across all velocities, indicating that rotor proximity dominates the wake behaviour. However, at $Ts = 1.0R$ (Fig. 6.16), inflow velocity plays a more active role in shaping the vertical wake structure, with higher wind speeds leading to earlier and more uniform recovery.

6.5.3 Influence of Inflow Velocity

The λ, which controls the rotor system's aerodynamic loading and wake dynamics, is directly impacted by inflow velocity. This section examines how wake characteristics change as λ values increase at three different inflow velocities: U_∞ = 3.55 m/s, 4.55 m/s, and 5.55 m/s. The wake at U_∞ = 3.55 m/s is diffuse and broad in vertical and horizontal planes. The shallow, laterally and vertically distributed velocity deficit regions indicate weak flow confinement and reduced energy extraction. Because of the comparatively low rotor-induced turbulence, the wakes behind the two rotors at close spacing combine, but the overall interaction stays moderate. The wake gets more organised at U_∞ = 4.55 m/s. The outlines of the deficiency zones narrow and deepen, indicating increased aerodynamic loading. While larger spacing preserves discrete wake cores, lower spacing intensifies the merger of wakes. As momentum re-entrainment is enhanced by increased λ-driven mixing, there is also evidence of improved streamwise recovery.

The impact of high λ is evident at U_∞ = 5.55 m/s. Particularly after $x/R = 2$, the streamwise velocity recovery quickens, and the wake regions are well delineated with profound deficits. However, the aerodynamic interaction between the two rotors increases with close spacing, leading to a more complex flow field and considerable wake overlap. Wider spacing allows the two wakes to recover more independently and maintain their shape. Across both spacing configurations, increasing the inflow velocity generally promotes faster wake recovery. This is most clearly seen in Figs. 6.13 and 6.16, where the U_∞ = 5.55 m/s cases show reduced or flattened deficits downstream. The higher kinetic energy and turbulence levels at elevated velocities enhance mixing and entrainment, accelerating the decay of wake deficits. However, the impact of velocity is more pronounced at $Ts = 1.0R$ compared to $Ts = 0.5R$. At closer spacing, the wake interference is so strong that it overwhelms the benefits of increased turbulence, particularly in the vertical plane. At wider spacing, the reduced interaction allows the benefits of higher inflow velocity to manifest more clearly, resulting in faster recovery.

6.5.4 Wake Symmetry and Recovery Onset

The wake fields at $Ts = 1.0R$ exhibit better symmetry and earlier onset of recovery in both planes, particularly beyond $x/R = 2$. At $Ts = 0.5R$, the merging wakes create asymmetries and delay recovery until around $x/R = 3$. This has implications for the layout of turbine arrays, as closer spacing may lead to reduced performance in downstream units due to prolonged wake interference.

The comparison confirms that rotor tip spacing has a significant influence on wake behaviour. Closer spacing (*Ts* = *0.5R*) intensifies wake interaction, delays recovery, and reduces the effectiveness of velocity-driven turbulence, especially in the vertical direction. Wider spacing (*Ts* = *1.0R*) facilitates more independent wake development, smoother recovery, and greater sensitivity to inflow velocity. These findings are critical for optimizing turbine placement in MRSs and dense wind farm configurations.

6.6 Summary of the Study

This chapter provided a thorough aerodynamic analysis of a double-rotor wind turbine system by examining the distribution of velocity deficits in horizontal and vertical planes under different rotor tip spacings and inflow velocities. The wake structures were analysed using U^* as the main parameter to comprehend the impact of rotor-rotor interaction and λ. The findings showed that input velocity and tip spacing significantly impacted wake structure and recovery. The wakes were scattered, symmetrical, and broad at lower inflow velocities, suggesting low turbulence and limited energy extraction. Particularly when $x/R = 2$, the wakes become more restricted as the velocity rises, exhibiting more profound deficits and quicker recovery. Stronger and more consistent wakes resulted from increased aerodynamic loading caused by higher λ values.

Tip spacing significantly affected wake interference. Increased turbulence and a delayed recovery resulted from the wakes merging early at *Ts* = *0.5R*, particularly at higher velocities. *Ts* = *1.0R*, on the other hand, minimised aerodynamic interference and permitted smoother re-energisation of the flow by permitting each wake to form independently. When comparing different planes, the vertical plane focuses on the function of confinement and symmetry around hub height. In contrast, the horizontal plane highlighted lateral wake merging and asymmetry at close spacing. To fully capture the dynamics of wake evolution, both perspectives were necessary.

The area-integrated velocity deficit along the downstream direction for a side-by-side double-rotor wind turbine configuration. For two rotor spacing conditions, *Ts* = *0.5R* and *Ts* = *1.0R*, the wake behaviour is investigated in both horizontal and vertical planes under three inflow velocities: U_∞ = 3.55 m/s, 4.55 m/s, and 5.55 m/s. These numbers shed light on how rotor proximity and free-stream velocity impact wake interaction, merging, and recovery.

Overall, the results highlight correctly choosing tip spacing and operational λ to reduce wake losses and maximise aerodynamic performance in multi-rotor systems. Independent of inflow velocity, close rotor spacing ($Ts = 0.5R$) results in stronger wake interactions, especially in the horizontal plane, and delays recovery. Wider spacing ($Ts = 1.0R$), on the other hand, lessens wake interference and permits inflow velocity to contribute more significantly to wake dissipation, especially in the vertical direction. These realisations are essential for comprehending wake dynamics in small turbine configurations and maximising rotor location in MRSs. The development of more effective rotor configurations for small wind turbine arrays is based on these discoveries.

CHAPTER 7

CONCLUSION AND FUTURE SCOPES

7.1 Summary of Key Findings

The presents study examined the aerodynamic wake properties of HAWTs in single- and double-rotor configurations. The study focused on the wake creation, interaction, and recovery behaviour under different tip speed ratios and rotor tip spacings. In controlled wind tunnel circumstances, complete flow field assessments behind SHAWTs were made possible by experimental observations employing sophisticated flow diagnostic methods as HWA.

7.1.1 Wake Behaviour of Single-Rotor Arrangement

The downstream wake in the single rotor arrangement shows a slow decrease in velocity gradient, indicating wind speed recovery and decreasing flow distortion as one gets farther from the rotor. The conventional wake structure, which consists of a high-velocity deficit core surrounded by shear layers and tip vortices, was discovered. Strong asymmetry and high turbulence intensity, especially in the area just downstream of the rotor, were characteristics of the near wake. The nacelle and hub significantly impact near the rotor plane, which causes localised velocity decreases and increased flow non-uniformity. The tower introduces disturbances that further disrupt wake structure, particularly in the near-wake region, and even small yaw misalignments affect the flow's symmetry.

Developing a helical vortex structure adds a tangential component to the flow by introducing increased velocities at lateral points ($y/R = \pm 1$). As the wake changes, the vortex pitch rises downstream, influenced by wind speed and the λ. With velocity recovery and partial re-energisation from the surrounding flow, the wake progressively changed into a more scattered structure further downstream. These aspects characterise the intricate aerodynamic properties of the single rotor wake, which affect the accuracy of wake modelling and performance prediction. Although these data supported theoretical predictions, they also demonstrated the necessity of correction factors in low *Re* scenarios, common in small wind turbines.

7.1.2 Wake Interaction in Double-Rotor Arrangement

In systems with two or more rotors, intricate wake interactions were noted. The wake interaction is more complicated in the double-rotor design since two rotor systems are next to each other. The velocity gradient decreases with downstream distance, suggesting a slow wake recovery. However, the central wake region shows more interference because of overlapping shear layers and mutual aerodynamic impact than in the single-rotor scenario. Due to increased hub and nacelle effects and broken flow symmetry, the proximity of the rotors causes a greater velocity deficit zone close to the rotor plane at $T_S = 0.5R$. These vortices interact with one another to produce a tangential velocity component. As tip spacing increases to $T_S = 1.0R$, these vortical structures are more spatially separated, reducing mutual interference and enhancing wake recovery. Significant mutual interference was seen at closer tip spacing ($T_S = 0.5R$), which resulted in compounding velocity deficits, decreased wake symmetry, and delayed recovery. On the other hand, due to the increased entrainment of ambient flow, the wider tip spacing ($T_S = 1.0R$) demonstrated better flow structure, less overlap of individual wakes, and faster recovery. These results offer empirical support for optimal rotor placement in distributed arrays and highlight the significance of tip spacing in MRS design.

The flow field is further distorted by yaw misalignment between the rotors, which can be caused by wake distortion or is intrinsic. This results in asymmetric velocity profiles and performance abnormalities. Particularly in low λ conditions, when higher wake rotation continues closer to the rotor, the pitch of the helical vortex shedding rises with downstream distance. Near the centreline, the tower shadow effects are still noticeable, but as tip spacing increases, their impact decreases. All things considered, the double-rotor system displays wake behaviours that are extremely sensitive to operating circumstances and spacing. Wider spacing promotes a more stable and symmetric flow, providing a design trade-off between compactness and aerodynamic efficiency in multi-rotor wind turbine arrays. In contrast, tighter spacing increases interaction and slows wake recovery.

7.1.3 Influence of Rotor Spacing and Tip Speed Ratio

The combined effects of λ and rotor tip spacing on wake behaviour were thoroughly examined. Wider, more dispersed wakes with slower recovery were the outcome of lower λ conditions, indicative of small wind turbine operation. Due to increased wake interactions and turbulence, the aerodynamic performance further declined when close rotor spacing was used. These patterns demonstrate how sensitive wake development is to operational and geometrical factors, and they provide design recommendations for optimising efficiency in small-scale turbine arrays.

7.2 Contributions to the Field

This thesis makes a significant and original contribution to the field of wind turbine wake aerodynamics, with a particular emphasis on small-scale and MRSs configurations operating under low *Re* conditions. By combining systematic wind-tunnel experimentation with physically grounded analysis, the present work establishes a robust foundation for advancing wake modelling, optimising small turbine layouts, and improving the performance of distributed wind energy systems, and raising the general efficiency of distributed wind energy systems by offering an experimental insights and design guidance. The key contributions of this research are summarised as follows:

- The study substantially extends the current understanding of wake behaviour in small and MRS configurations, particularly under low TSR and closely spaced rotor arrangements, which are relevant to practical small-scale wind energy deployment.
- A Comprehensive experimental wake database has been generated for both single and double-rotor arrangements, spanning multiple downstream locations and covering both horizontal and vertical planes. High resolution planar velocity mapping using HWA has enabled detailed three-dimensional interpretation of wake formation, interaction, symmetry breakdown, and recovery trends, which remain limited in the existing literature for small-scale rotors.
- With rigorous blockage correction, a strong experimental methodology was developed, including manometry, and HWA. Future research in this area will be guided by the methodology's optimization for SHAWTs and low *Re* flows.
- The wake analysis's conclusions turned into helpful design advice. These include recommendations for blade design appropriate for small MRS layouts, the best tip spacing for reducing wake interference, and the use of operating λ for efficient wake management.

- The experimental findings provide a valuable benchmark for validation and improving classical wake models. The results explicitly demonstrate the limitations of traditional momentum based and self-similar wake models when applied to small-scale, low *Re*, and MRS configurations, thereby highlighting the need for hybrid, modified, or data-driven modelling approaches in such complex flow environments.

7.3 Limitations of the Present Work

Some limitations should be noted, even though this study offers comprehensive experimental insights into the near-wake behaviour of single and double-rotor HAWTs under low λ situations. Although the controlled wind tunnel environment allowed for accurate observations, the studies could not adequately represent the large-scale flow structures and atmospheric turbulence variations in real-world settings. Because the study only examined two fixed $T_S = 0.5R$ and $1.0R$ for double-rotor system and a small λ range (≈ 2.5–3.0), it was impossible to extrapolate the results to the larger operating envelope of MRSs. The observations were based on hot-wire anemometry, which requires interpolation to produce full-field visualisations despite having excellent temporal resolution and being restricted to single-point measurements. Additionally, the study focuses on wake recovery and velocity deficit. Still, it ignores turbulence strength, spectral content, and unstable vortex dynamics, all known to affect wake mixing and stability. Lastly, it may be necessary to consider scaling effects before extrapolating the results to utility-scale wind turbines, as the results are specific to the rotor geometry, size, and wind tunnel blockage ratio utilised in this work. Future research should include turbulence intensity measurements and unstable vortices, expand the study to include broader operating circumstances, and examine scaling impacts for practical uses. These initiatives will aid in generalising the results and improving wake interaction models for MRSs.

The use of HWA, which offers excellent temporal resolution but only point-wise velocity data and indirect inference of three-dimensional flow structures, limits the current investigation. Probe alignment, calibration uncertainty, and strong turbulence in the immediate wake all affect measurement accuracy. Direct extrapolation to utility-scale turbines must be done carefully because the trials were conducted at low *Re* relevant to small HAWTs. The impacts of residual blocking and wind tunnel confinement may affect wake recovery and spreading. The study excluded power output, blade loading, and acoustic effects, concentrating mainly on velocity deficit. The only factors taken into consideration were uniform inflow circumstances, operating λ, and restricted tip spacing. There was no modelling of atmospheric phenomena, including shear, yaw, and gusts.

7.4 Future Research Directions

Even though this study has effectively improved our knowledge of wake behaviour in small HAWTs and MRSs, it also creates several new research opportunities.

(a). Advanced Wake Measurement Techniques

- Employ high-speed imaging and volumetric PIV methods (such as tomographic PIV) to capture vortex dynamics, three-dimensional flow structures, and near-wake instabilities with higher accuracy.
- Combine quantitative measurements with flow visualisation methods like smoke or dye injection could be used with quantitative measures for more complete understanding of wake formation and breakdown.

(b). Integrated Numerical-Experimental Frameworks

- Couple high-fidelity numerical simulations (LES, DES) with multi-component experimental measurements to better resolve low-Re aerodynamics and wake evolution.
- Conduct performance validation under controlled inflow to correlate wake characteristics with power/torque outputs more rigorously.

(c). Optimised Rotor Positioning for MRS

- Use wake-interference insights to determine optimal rotor spacing and alignment for future MRS-based wind farms.
- Combine wake datasets with computational optimisation methods (adjoint optimisation, evolutionary algorithms) for improved layout design.

(d). Wake-Aware Control and Smart Grid Integration

- Investigate real-time wake adaptation strategies, active control schemes, and load-management approaches to enhance system robustness.
- Explore how small HAWTs and MRSs can operate efficiently within decentralised or smart-grid energy networks.

(e). Acoustic, Structural, and Environmental Considerations

- Extend wake studies to include acoustic emissions, structural fatigue response, and environmental effects critical for residential or semi-urban applications.

- Develop assessment methods to ensure safe, quiet, and sustainable deployment of small wind systems.

(f). Broader Practical Implications for Micro-Wind Systems

- Translate wake insights into practical guidelines for micro-wind farm layout, turbine spacing, and operating strategies.
- Support optimisation of small-scale wind systems through improved understanding of wake-driven performance limits.

7.5 Winding Up

In conclusion, wake production, interaction, and recovery in single and double-rotor HAWTs under low tip speed ratio conditions have been thoroughly experimentally characterised in this thesis, with special attention paid to the effects of tip spacing and inflow velocity. The findings fill a significant knowledge vacuum for small-scale and MRSs by providing empirical support for better wake modelling, aerodynamic design, and spacing optimisation. The study creates a strong methodological and analytical framework for further research, even while some limitations, such as small working environments, wind tunnel scaling effects, and the exclusion of turbulence spectrum analyses, temper the generalisation of the results. The suggested research directions provide a clear path for improving MRS technology's scientific understanding and practical application, which range from sophisticated flow diagnostics to computational optimisation and integration with real-world energy systems. The significance of near-wake research in forming the upcoming generation of effective, flexible, and decentralised wind energy systems is ultimately reaffirmed by this work. Overall, the work provides a strong foundation for future innovations in aerodynamic design, wake modelling, and micro-wind system optimisation.

References

Abdelsalam, A. M., El-Askary, W. A., Kotb, M. A., and Sakr, I. M. (2021). Experimental Study on Small Scale Horizontal Axis Wind Turbine of Analytically-Optimized Blade with Linearized Chord Twist Angle Profile. *Energy*, 216, 119304.

Adaramola, M. S., and Krogstad, P. Å. (2011). Experimental Investigation of Wake Effects on Wind Turbine Performance. *Renewable Energy*, 36(8), 2078–2086.

Adhikari, J., Sapkota, R., and Panda, S. K. (2018). Impact of Altitude and Power Rating on Power-to-Weight and Power-to-Cost Ratios of the High Altitude Wind Power Generating System. *Renewable Energy*, 115, 16–27.

Adjiri, S., Dobrev, I., Benzaoui, A., Nedjari-Daaou, H., and Massouh, F. (2023). New Actuator Disk Model for the Analysis of Wind Turbines Wake Interaction with the Ground. *Journal of Applied Fluid Mechanics*, 16(1), 75-88

Aftab, S. M. A., Razak, N. A., Rafie, A. S. M., and Ahmad, K. A. (2016). Mimicking the Humpback Whale: An Aerodynamic Perspective. *Progress in Aerospace Sciences*, 84, 48–69.

Akour, S. N., Al-Heymari, M., Ahmed, T., and Khalil, K. A. (2018). Experimental and Theoretical Investigation of Micro Wind Turbine for Low Wind Speed Regions. *Renewable Energy*, 116(A), 215–223.

Albi, Anand, M.D., and Herbert, G.M.J. (2018). Aerodynamic Analysis on Wind Turbine Aerofoil. *International Journal of Engineering and Technology*, 7(3.27), 456-465

Anderson, M. B., Milborrow, D. J., and Ross, N. J. (1982). Performance and Wake Measurements on a 3 m Diameter Horizontal Axis Wind Turbine: Comparison of Theory, Wind Tunnel and Field Test Data. *United Kingdom.*

Annoni, J., Howard, K., Seiler, P., and Guala, M. (2016). An Experimental Investigation on the Effect of Individual Turbine Control on Wind Farm Dynamics. *Wind Energy*, 19(8), 1453–1467.

Bahaj, A. S., Molland, A. F., Chaplin, J. R., and Batten, W. M. J. (2007). Power and Trust Measurements of Marine Current Turbines Under Various Hydrodynamic Flow Conditions in a Cavitation Tunnel and a Towing Tank. *Renewable Energy*, 32(3), 407–426.

Barthelmie, R. J., Folkerts, L., Ormel, F. T., Sanderhoff, P., Eecen, P. J., Stobbe, O., and Nielsen, N. M. (2003). Offshore Wind Turbine Wakes Measured by Sodar. *Journal of Atmospheric and Oceanic Technology*, 20(4), 466–477.

Bastankhah, M., and Abkar, M. (2019). Multirotor Wind Turbine Wakes. *Physics of Fluids*, 31(8).

Bastankhah, M., and Porté-Agel, F. (2016). Experimental and Theoretical Study of Wind Turbine Wakes in Yawed Conditions. *Journal of Fluid Mechanics*, 806, 506-541.

Becerra, M., Morán, J., Jerez, A., Cepeda, F., and Valenzuela, M. (2017). Wind Energy Potential in Chile: Assessment of a Small-Scale Wind Farm for Residential Clients. *Energy Conversion and Management*, 140, 71–90.

Bianchini, A., Bangga, G., Baring-Gould, I., Croce, A., Cruz, J. I., Damiani, R., Erfort, G., Simao Ferreira, C., Infield, D., Nayeri, C. N., Pechlivanoglou, G., Runacres, M., Schepers, G., Summerville, B., Wood, D., and Orrell, A. (2022). Current Status and Grand Challenges for Small Wind Turbine Technology. *Wind Energy Science*, 7(5), 2003–2037.

Bilgili, M., Tontu, M., & Sahin, B. (2020). Aerodynamic Rotor Performance of a 3300-kW Modern Commercial Large-Scale Wind Turbine Installed in a Wind Farm. ASME. *Journal of Energy Resources Technology*, 143(3), 031302.

Bishop, M., and Yarusevych, S. (2011). Mitigating Blockage Effects on Flow Over a Circular Cylinder in an Adaptive-Wall Wind Tunnel. *ASME Journal of Fluids Engineering*, 133(8), 081101.

Bortolotti, P., Bottasso, C. L., and Croce, A. (2020). Comparison of Electrical Collection Topologies for Multi-Rotor Wind Turbines. *Wind Energy Science*, 5, 1237–1251.

Burdett, T., and Van, K. (2012). Scaling Small-Scale Wind Turbines for Wind Tunnel Testing. *ASME Paper No. GT2012-68359*, 811–820.

Burton, T., Sharpe, D., Jenkins, N., and Bossanyi, E. (2007). Wind Energy Handbook. *John Wiley & Sons* ,3rd Edition.

Butterfield, C. P., Scott, G., and Musial, W. (1992). Comparison of Wind Tunnel Airfoil Performance Data with Wind Turbine Blade Data. *ASME Journal of Solar Energy Engineering*, 114(2), 119–124.

Carrión, M., Woodgate, M., Steijl, R., Barakos, G. N., Gomez-Iradi, S., and Munduate, X. (2015). Understanding Wind-Turbine Wake Breakdown Using Computational Fluid Dynamics. AIAA *Journal*, 53(3), 588-602.

Casini, M. (2016). Small Vertical Axis Wind Turbines for Energy Efficiency of Buildings. *Journal of Clean Energy Technology*, 4, 56–65.

Chamorro, L.P., Arndt, R.E., and Sotiropoulos, F. (2011). Reynolds Number Dependence of Turbulence Statistics in the Wake of Wind Turbines. *Wind Energy*, 15(5), 733-742.

Chen, L., and MacDonald, E. (2012). Considering Landowner Participation in Wind Farm Layout Optimization. *Journal of Mechanical Design*, 134, 084506.

Chen, T. Y., and Liou, L. R., 2011. Blockage Corrections in Wind Tunnel Tests of Small Horizontal-axis Wind Turbines. *Experimental Thermal and Fluid Science*, 35(3), 565-569.

Churchfield, M. J., Lee, S., Michalakes, J., and Moriarty, P. J. (2013). A Numerical Study of the Effects of Atmospheric and Wake Turbulence on Wind Turbine Dynamics. *Journal of Solar Energy Engineering*, 135(3).

Costello, S., Costello, C., François, G., and Bonvin, D. (2015). Analysis of the Maximum Efficiency of Kite-power Systems. *Journal of Renewable and Sustainable Energy*, 7, 053108.

Dehouck, V., Lateb, M., Sacheau, J., and Fellouah, H. (2018). Application of the Blade Element Momentum Theory to Design Horizontal Axis Wind Turbine Blades. *ASME Journal Solar Energy Engineering*, 140(1), 014501.

Dilimulati, A., Stathopoulos, T., and Parashivoiu, M. (2018). Wind Turbine Designs for Urban Applications: A Case Study of Shrouded Diffuser Casing for Turbines. *Journal of Wind Engineering and Industrial Aerodynamics*, 175, 179–192.

Duquette, M. M., and Visser, K. D. (2003). Numerical Implications of Solidity and Blade Number on Rotor Performance of Horizontal-Axis Wind Turbines. *Journal of Solar Energy Engineering, Transactions of the ASME*, 125(4), 425–432.

Elkodama, A., Ismaiel, A., Abdellatif, A., and Shaaban, S. (2022). Aerodynamic Performance and Structural Design of 5 MW Multi Rotor System (MRS) Wind Turbines. *International Journal of Renewable Energy Research*, 12(3), 1495–1505.

Eriksen, P-E., and Krogstad. P. A. (2018). An Experimental Study of the Wake of a Model Wind Turbine Using Phase-averaging. *International Journal of Heat and Fluid Flow*, 67(Part B), 52-62.

Evans, S.P., Bradney, D.R., and Clausen., P. D. (2017). Development and Experimental Verification of a 5 kW Small Wind Turbine Aeroelastic Model. *Journal of Wind Engineering and Industrial Aerodynamics*, 181, 104-111.

Feltes, J.W., Fernandes, B.S., and Keung, P.K. (2011). Case Studoies of Wind Park Modeling. *IEEE Power and Energy Society General Meeting*, Detroit, MI, USA, 1-7

Fiedler, B. H., and Bukovsky, M. S. (2011). The Effect of a Giant Wind Farm on Precipitation in a Regional Climate Model. *Environmental Research Letters*, *6*(4), 045101.

Frandsen, S. (1992). On the Wind Speed Reduction in the Center of Large Clusters of Wind Turbines. *Journal of Wind Engineering and Industrial Aerodynamics*, 39(1–3), 251–265.

Fuglsang, P., Christian, B., Mac, G., and Antoniou, I. (2004). Design and Verification of the Risø-B1 Airfoil Family for Wind Turbines. *Journal of Solar Energy Engineering*, 126(4), 1002–1010.

Gad-el-Hak, M. (2007). Flow Control: Passive, Active, and Reactive Flow Management. *Cambridge University Press.*

Ghaisas, N. S., Ghate, A. S., and Lele, S. K. (2020). Effect of Tip Spacing, Thrust Coefficient and Turbine Spacing in Multi-Rotor Wind Turbines and Farms. *Wind Energy Science*, 5(1), 51–72.

Giguere, P., and Selig, M. S. (1997). Low Reynolds Number Airfoils for Small Horizontal Axis Wind Turbines. *Wind Engineering*, 21(6), 367–380.

Giguere, P., and Selig, M. S. (1998). New Airfoils for Small Horizontal Axis Wind Turbines. *Wind Engineering*, 120(2), 108–114.

Göltenbott, U., Ohya, Y., Yoshida, S., and Jamieson, P. (2017). Aerodynamic Interaction of Diffuser Augmented Wind Turbines in Multi-Rotor Systems. *Renewable Energy*, 112.

González-Longatt, F., Wall, P. P., and Terzija, V. (2012). Wake Effect in Wind Farm Performance: Steady-State and Dynamic Behavior. *Renewable Energy*, 39(1), 329–338.

Grant, I., and Parkin., P. (2000). A DPIV Study of the Trailing Vortex Elements from the Blades of a Horizontal Axis Wind Turbine in Yaw. *Experiments in Fluids*, *28*, 368–376.

Green, J. E. (2008). Laminar Flow Control - Back to the Future? AIAA *38th Fluid Dynamics Conference and Exhibit*, Seattle,Washington.

Gupta, R. K., Warudkar, V., Purohit, R., and Rajpurohit, R. S. (2017). Modelling and Aerodynamic Analysis of Small-Scale, Mixed Airfoil Horizontal Axis Wind Turbine Blade. *Materials Today: Proceedings*, 4, 5370-5384.

Guo, T., Guo, X., Gao, Z., Li, S., Zheng, X., Gao, X., Li, R., Wang, T., Li, Y., and Li, D. (2021). Nacelle and Tower Effect on a Stand-alone Wind Turbine Energy Output- A Discussion on Field Measurements of a Small Wind Turbine. *Applied Energy*, 303, 117590.

Hancock, P. E., and Pascheke, F. (2014). Wind-Tunnel Simulation of the Wake of a Large Wind Turbine in a Stable Boundary Layer. Part 2: The Wake Flow. *Boundary-Layer Meteorology*, 151, 23–37.

Hancock, P. E., Zhang, S., Pascheke, F., and Hayden, P. (2014). Wind Tunnel Simulation of a Wind Turbine Wake in Neutral, Stable and Unstable Wind Flow. *Journal of Physics: Conference Series*, 555(1).

Hasan, M., El-Shahat, A., and Rahman, M., 2017. Performance Investigation of three Combined Airfoils Bladed Small-Scale Horizontal Axis Wind Turbine by BEM and CFD Analysis. *Journal of Power and Energy Engineering*, 5(5), 14-27.

Hau, E. (2013). Wind Turbines (3rd ed.). Springer Berlin, Heidelberg.

Hezaveh, S. H., and Bou-Zeid, E. (2018). Increasing the Power Production of Vertical-Axis Wind Turbine Farms using Synergistic Clustering. *Boundary-Layer Meteorology*, 169(2), 275–296.

Hirahara, H., Hossain, M. Z., and Nonomura, Y. (2005). Testing Basic Performance of a Very Small Wind Turbine Designed for Multi-Purposes. *Renewable Energy*, 30(8), 1279–97.

Houck, D.R. (2021). Review of Wake Management Techniques for Wind Turbines. *Wind Energy*, 25(2), 195-220

Howell, R., Qin, N., Edwards, J., and Durrani, N. (2010). Wind Tunnel and Numerical Study of a Small Vertical-axis Wind Turbine. *Renewable Energy*, 35(2), 412-422.

Hu, H., Yang, Z., and Sarkar, P. (2012). Dynamic Wind Loads and Wake Characteristics of a Wind Turbine Model in an Atmospheric Boundary Layer Wind. *Experiments in Fluids*, 52(5), 1277–1294.

IEA, 2024. World Energy Outlook 2024. IEA, Paris

IRENA & ILO, 2024. Renewable energy and jobs: Annual review 2024.

Jackson, R. S., and Amano, R. S. (2017). Experimental Study and Simulation of a Small-Scale Horizontal-Axis Wind Turbine. *ASME Journal of Energy Resources Technology*, 139(5), 051207.

Jain, S., and Saha, U. K. (2019). The State-of-the-Art Technology of H-Type Darrieus Wind Turbine Rotors. *ASME Journal of Energy Resources Technology*, 142(3), 030801.

Jameson, P., & Branney, M. (2012). Multi-Rotors; a Solution to 20 MW and Beyond? *Energy Procedia*, 24, 52–59.

Jaszczur, M., Borowski, M., Halibart, J., Zwolińska-Glądys, K., and Marczak, P. (2024). Optimization of the Small Wind Turbine Design-Performance Analysis. *Computation*, 12(11), 215.

Jureczko, M., Pawlak, M., and Mężyk, A. (2005). Optimisation of Wind Turbine Blades. *Journal of Materials Processing Technology*, 167, 463–471.

Kale, S. A., and Sapali, S. . (2013). A Review of Multi-Rotor Wind Turbine Systems. *Journal of Sustainable Manufacturing and Renewable Energy*, *2*, 60-68.

Karthikeyan, N., Murugavel, K., Kumar, S. A., and Rajakumar, S. (2015). Review of Aerodynamic Developments on Small Horizontal Axis Wind Turbine Blade. *Renewable Sustainable Energy Reviews*, 42, 801–822.

Kassa, B.T., Baheta, A.T., and Beyene, A. (2024). Aerodynamic performance characteristics of Low Re Airfoils: A Parametric and Multi Criteria Study. *Results in Engineering*, 24, 103174.

Keisar, D., De Troyer, T., and Greenblatt, D. (2020). Concept and Operation of a Wind Turbine Driven by Dynamic Stall. *AIAA Journal*, 58(6), 2370–2376.

Khan, M., Odemark, Y., and Fransson, J. H. M. (2017). Effects of Inflow Conditions on Wind Turbine Performance and near Wake Structure. *Open Journal of Fluid Dynamics*, *07*(01), 105–129.

Kishore, R. A., and Priya, S. (2013). Design and Experimental Verification of a High Efficiency Small Wind Energy Portable Turbine (SWEPT). *Journal of Wind Engineering and Industrial Aerodynamics*, 118, 12–19.

Kosasih, B., and Tondelli, H. (2016). Influence of Inflow Turbulence Intensity on the Performance of Bare and Diffuser-Augmented Micro Wind Turbine Model. *Renewable Energy*, 87, 154–167.

Krogstad, P. –Å., and Lund, J. A., 2012. An Experimental and Numerical Study of the Performance of a Model Turbine. *Wind Energy*, 15(3), 443-457.

Kuo, J. Y. J., Romero, D. A., and Amon, C. H. (2015). A Mechanistic Semi-Empirical Wake Interaction Model for Wind Farm Layout Optimization. *Energy*, *93*, 2157–2165.

Lanzafame, R., and Messina, M., 2010. Power Curve Control in Micro Wind Turbine Design. Energy, 35(2), 556–561.

Ledoux, J., Riffo, S., Salomon, J. (2020). Analysis of the Blade Element Momentum Theory. SIAM *Journal on Applied Mathematics*, 81(6), 2596–2621.

Lee, H., and Lee D. (2020). Low Reynolds Number Effects on Aerodynamic Loads of a Small Scale Wind Turbine. *Renewable Energy*, 154, 1283-1293.

Li, B., Zhou, D.L., Wang, Y.,Shuai, Y., Liu, Q.Z., and Cai, W.H. (2020). The DEsign of a Small Lab-Scale Wind Turbine Model with High Performance Similarity to Its Utility-Scale Prototype. *Renewable Energy*, 149, 435–444.

Li, L., Tan, W., Zhang, J., Han, G., & Zhang, Y. (2022). Unsteady Effects of Wake on Downstream Rotor at Low Reynolds Numbers. *Energies*, *15*(18), 6692.

Li, Q., Murata, J., Endo, M., Maeda, T., and Kamada, Y. (2016). Experimental and Numerical Investigation of the Effect of Turbulent Inflow on a Horizontal Axis Wind Turbine (part II: Wake Characteristics). *Energy*, 113, 1304–1315.

Lignarolo, L. E. M., Ragni, D., Krishnaswami, C., Chen, Q., Simão Ferreira, C. J., and van Bussel, G. J. W. (2014). Experimental Analysis of the Wake of a Horizontal-Axis Wind-Turbine Model. *Renewable Energy*, 70, 31–46.

Lignarolo, L. E. M., Ragni, D., Scarano, F., Simão Ferreira, C. J., & van Bussel, G. J. W. (2015). Tip-vortex instability and turbulent mixing in wind-turbine wakes. *Journal of Fluid Mechanics*, *781*, 467–493.

Lipian, M., Dobrev, I., Karczewski, M., Massouh, F., and Jozwik, K. (2016). Small Wind Turbine Augmentation: Experimental Investigation of Shrouded and Twin-rotor Wind Turbine Systems. *Energy*, 186, 115855.

Lissaman, P. B. S. (1979). Energy Effectiveness of Arbitrary Arrays of Wind Turbines. *Journal of Energy*, 3(6), 323–328.

Liu, J., Lin, H., and Zhang, J. (2019). Review on the Technical Perspectives and Commercial Viability of Vertical Axis Wind Turbines. *Ocean Engineering*, 182, 608–626.

Liu, J., Li, P., He, W., and Jiang, K. (2020). Numerical Study of the Effect of Surface Grooves on the Aerodynamic Performance of a NACA 4415 Airfoil for Small Wind Turbines. *Journal of Wind Engineering and Industrial Aerodynamics*, 206, 104263.

Magnusson, M., and Smedman, A.-S. (1999). Air Flow Behind Wind Turbines. *Journal of Wind Engineering and Industrial Aerodynamics*, 80(1–2), 169–189.

Malhotra, P., Sharma, P., and Tiwari, P. (2023). Aerodynamic and Noise Performance Evaluation of Small Horizontal-Axis Wind Turbines under Low Reynolds Number Flows. *Renewable Energy*, 215, 405–416.

Manwell, J. F., Mcgowan, J. G., and Rogers, A. L. (2009). Wind Energy Explained: Theory, Design, and Application. In *Wiley* (2nd ed.).

Matsumiya, H., Ito, R., Kawakami, M., Matsushita, D., Iida, M., and Arakawa, C. (2010). Field Operation and Track Tests of 1-Kw Small Wind Turbine Under High Wind Conditions. *ASME Journal of Solar Energy Engineering*, 132(1), 011002.

McTavish, S., Feszty, D., and Nitzsche, F. (2013). Evaluating Reynolds Number Effects in Small-Scale Wind Turbine Experiments. *Journal of Wind Engineering and Industrial Aerodynamics*, 120, 81–90.

Medici, D., and Alfredsson, P. H. (2006). Measurements on a Wind Turbine Wake: 3D Effects and Bluff Body Vortex Shedding. *Wind Energy*, 9(3), 219–236.

Medici, D., and Alfredsson, P. H. (2008). Measurements Behind Model Wind Turbines: Further Evidence of Wake Meandering. *Wind Energy*, 11(2), 211–217.

Milborrow, D. J. (1980). The Performance of Arrays of Wind Turbines. *Journal of Wind Engineering and Industrial Aerodynamics*, 5(3–4), 403–430.

MNRE, 2023. Annual report 2023-2024*: Ministry of New and Renewable Energy (MNRE), Government of India* (Issue 15018).

Mohammed, A. A., Sahin, A. Z., and Ouakad, H. M. (2019). Numerical Investigation of a Vertical Axis Wind Turbine Performance Characterization Using New Variable Pitch Control Scheme. *Journal of Energy Resources Technology*, 142(3).

Munters, W., and Meyers, J. (2018). Towards Practical Dynamic Induction Control of Wind Farms: Analysis of Optimally Controlled Wind-Farm Boundary Layers and Sinusoidal Induction Control of First-Row Turbines. *Wind Energy Science*, 3(1), 409–425.

Neagoe, M., Saulescu, R., Jaliu, C., and Simionescu, P. A. (2020). A Generalized Approach to the Steady-State Efficiency Analysis of Torque-Adding Transmissions used in Renewable Energy Systems. *Energies*, 13(17).

Nguyen, L., and Metzger, M. (2017). Optimization of a Vertical-axis Wind Turbine for Application in an Urban/suburban Area. *Journal of Renewable and Sustainable Energy*, 9(4), 043302.

Odemark, Y., and Fransson, J. H. M. (2013). The Stability and Development of Tip and Root Vortices Behind a Model Wind Turbine. *Experiments in Fluids*, 54(9), 1591.

Ohya, Y., Miyazaki, J., Göltenbott, U., and Watanabe, K. (2017). Power Augmentation of Shrouded Wind Turbines in a Multirotor System. *Journal of Energy Resources Technology*, 139.

Okulov, V. L., and van Kuik, G. A. M. (2012). The Betz–Joukowsky Limit: on the Contribution to Rotor Aerodynamics by the British, German and Russian scientific schools. *Wind Energy*, 15(2), 335–344.

Pope, A., and Harper, J.J. (1966). Low Speed Wind Tunnel Testing. *John Wiley and Sons, New York*.

Pourrajabian, A., Mirzaei, M., Ebrahimi, R., and Wood, D. (2014). Effect of Air Density on the Performance of a Small Wind Turbine Blade: A case study in Iran. *Journal of Wind Engineering and Industrial Aerodynamics*, 126, 1–10.

Prasad, E.N., Janakiram, S., Prabu, T., and Sivasubramaniam, S. (2014). Design and Development of Horizontal Small Wind Turbine Blade for Low Wind Speeds: A case study in Iran. *International Journal of Engineering Science and Advanced Technology*, 4, 75-84.

Rahgozar,S., Pourrajabian, A., Kazmi, S.A., and Kazmi, S.M.R. (2020). Performance Analysis of a Small Horizontal Axis Wind Turbine under Use of Linear/Nonlinear Distributions for the Chord and Twist Angle. *Energy for Sustainable Developement*, 58, 42-49.

Refan, M., and Hangan, H. (2012). Aerodynamic Performance of a Small Horizontal Axis Wind Turbine. *Journal of Solar Energy Engineering*, 134(2), 021013.

RES, 2024. Renewable Energy Statistics. *In International Renewable Energy Agency*.

Rocha, P. A. C., Araujo, J. W. C., Lima, R. J. P., Silva, M. E. V., Albiero, D., Andrade, C. F., and Carneiro, F. O. M. (2018). The Effects of Blade Pitch Angle on the Performance of Small-Scale Wind Turbine in Urban Environments. *Energy*, *148*, 169–178.

Sedaghatizadeh, N., Arjomandi, M., Kelso, R., Cazzolato, B., and Ghayesh, M. H. (2019). The Effect of the Boundary Layer on the Wake of a Horizontal Axis Wind Turbine. *Energy*, 182, 1202-1221.

Selig, M. S., and McGranahan, B. D. (2004). Wind Tunnel Aerodynamic Tests of Six Airfoils for Use on Small Wind Turbines. *ASME Journal of Solar Energy Engineering*, 126(4), 986–1001.

Shen, X., Yang, H., Chen, J., Zhu, X., and Du, Z. (2016). Aerodynamic Shape Optimization of Non-Straight Small Wind Turbine Blades. *Energy Conversion Management*, 119, 266–278.

Sheridan, L., Kazimierczul, K., Garbe, J., and Preziuso, D. (2024). *Distributed Wind 2024 Edition*.

Sherry, M., Sheridan, J., and Jacono, D. Lo. (2013). Characterisation of a Horizontal Axis Wind Turbine's Tip and Root Vortices. *Experiments in Fluids*, 54(3), 1417.

Shin, P., and Keonhoon, K. (2020). Aerodynamic Performance Prediction of SG6043 Airfoil for a Horizontal Axis Small Wind Turbine. *Journal of Physics: Conference Series*, 1452, 012018.

Shimizu, Y., and Kamada, Y. (2001). Studies on a Horizontal Axis Wind Turbine with Passive Pitch-Flap Mechanism (Performance and Flow Analysis Around Wind Turbine). ASME *Journal of Fluids Engineering*, 123(3), 516–522.

Siddall, R. G., and Davies, T. W., 1972. An Improved Response Equation for Hot-Wire Anemometry. *Internal Journal of Heat Mass Transfer*, 15, 367-368.

Sieros, G., Chaviaropoulos, P., Sorensen, J. D., Bulder, B. H., and Jamiesson, P. (2012). Upscaling Wind Turbines: Theoretical and Practical Aspects and their Impact on the Cost of Energy. *Wind Energy*, 15, 3–17.

Simpson, R. L., Heizer, K. W., and Nasburg, R. E., 1979. Performance Characteristics of a Simple Linearized Hot-Wire Anemometer. *ASME Journal of Fluids Engineering*, 101(3), 381-382.

Singh, R. K., and Ahmed, M. R. (2013). Blade Design and Performance Testing of a Small Wind Turbine Rotor for Low Wind Speed Applications. *Renewable Energy*, 50, 812–819.

Singh, R. K., Ahmed, M. R., Zullah, M. A., and Lee, Y. H. (2012). Design of a Low Reynolds Number Airfoil for Small Horizontal Axis Wind Turbines. *Renewable Energy*, 42, 66–76.

Siram, O., Kesharwani, N., Sahoo, N., and Saha, U.K. (2022). Aerodynamic Design and Wind Tunnel Tests of Small-Scale Horizontal-Axis Wind Turbines for Low Tip Speed Ratio Applications. ASME *Journal of Solar Energy Engineering*, 144(4), 041009

Siram, O., Saha, U. K., and Sahoo, N. (2022). Blade Design Considerations of Small Wind Turbines: From Classical to Emerging Bio-Inspired Profiles/Shapes. *Journal of Renewable and Sustainable Energy*, 14(4), 042701.

Siram, O., and Sahoo, N. (2019). Near Wake Regime Study on Wind Turbine Blade Tip Vortex. *Gas Turbine India Conference*.

Siram, O., and Sahoo, N. (2022). Performance Assessment of Straight and Linearly Tapered Rotors through Wind Tunnel Investigation for Off-Grid Applications. *Wind Engineering*, 46(4), 1291–1310.

Siram, O., Shinde, S. Y., Kulkarni, V., and Sahoo, N. (2023). In-Depth three-Component Assessment of Wind Turbine Wake using Stereo PIV under Low Tip Speed Ratio Conditions. *Physics of Fluids*, 35(11), 115114.

Song, Q., and Luitz, W. D. (2014). Design and Testing of a New Small Wind Turbine Blade. *ASME Journal of Solar Energy Engineering*, 136(3), 034502.

Sørensen, J. N., and Shen, W. Z. (2002). Numerical Modeling of Wind Turbine Wakes. ASME *Journal of Fluids Engineering*, 124(2), 393–399.

Steven, R. J. A. M., and Meneveau, C. (2017). Flow Structure and Turbulence in Wind Farms. *Annual Review of Fluid Mechanics*, 49, 311–339.

Sun, S., Luo, D., Huang, D., and Wu, G. (2012). Numerical Investigation of Numerical Study on Coupling Effects Among Multiple Savonius Turbines. *Journal of Renewable and Sustainable Energy*, 4, 053107.

Talavera, M., and Shu, F. (2017). Experimental Study of Turbulence Intensity Influence on Wind Turbine Performance and Wake Recovery in a Low-Speed Wind Tunnel. *Renewable Energy*, 109, 363-371.

Tangler, W., and Rooij, R. V. (2003). Summary of the Delft University Wind Turbine Dedicated Airfoils. *ASME Journal of Solar Energy Engineering*, 125(4), 488–496.

Taylor, J., Eastwick, C., Lawrence, C., and Wilson, R. (2013). Noise Levels and Noise Perception from Small and Micro Wind Turbines. *Renewable Energy*, 55, 120–127.

Tchakoua, P., Wamkeue, R., Ouhrouche, M., Slaoui-Hasnaoui, F., Tameghe, T. A., and Ekemb, G. (2014). Wind Turbine Condition Monitoring: State-of-the-art Review, New Trends, and Future Challenges. *Energies*, 7(4), 2595–2630.

Tian, W., Ozbay, A., Wang, X. D., and Hu, H. (2017). Experimental Investigation on the Wake Interference among Wind Turbines Sited in Atmospheric Boundary Layer Winds. *Acta Mechanica Sinica*, 33, 742–753.

Tieleman, H. W. (1992). Wind Characteristics in the Surface Layer over Heterogeneous Terrain. *Journal of Wind Engineering and Industrial Aerodynamics*, 41–44, 329–340.

Treuren, K. W. V. (2015). Small-Scale Wind Turbine Testing in Wind Tunnels Under Low Reynolds Number Conditions. *ASME Journal of Energy Resources Technology*, 137(5), 051208.

Tummala, A., Velamati, R. K., Sinha, D. K., Indraja, V., and Krishna, V. H. (2016). A Review on Small Scale Wind Turbines. *Renewable and Sustainable Energy Reviews*, 56, 1351–1371.

Uemura, Y., Tanabe, Y., Mamori, H., Fukushima, N., and Yamamoto, M. (2017). Wake Deflection in Long Distance from a Yawed Wind Turbine. ASME *Journal of Energy Resources Technology*, 139(5), 051212.

van der Laan, M. P., Andersen, S. J., García, N. R., Angelou, N., Pirrung, G. R., Ott, S., Sjöholm, M., Sørensen, K. H., Neto, J. X. V., Kelly, M., Mikkelsen, T. K., and Larsen, G. C. (2019). Power Curve and Wake Analyses of the Vestas Multi-Rotor Demonstrator. *Wind Energy Science*, 4(2), 251–271.

Van Treuren, K. W. (2015). Small-scale Wind Turbine Testing in Wind Tunnels under Low Leynolds Number Conditions. *Journal of Energy Resources Technology, Transactions of the ASME*, 137(5), 051208.

Vermeer, L. J., Sørensen, J. N., and Crespo, A. (2003). Wind Turbine Wake Aerodynamics. *Progress in Aerospace Sciences*, 39(6–7), 467–510.

Vermeulen, P. E. J. (1980). An Experimental Analysis of Wind Turbine Wakes. *3rd International Symposium on Wind Energy Systems*, 431–450.

Villeneuve, T., and Dumas, G. (2021). Impact of Some Design Considerations on The Wake Recovery of Verticle- Axis Turbines. *Renewable Energy*, 180, 1419-1438.

Wang, C., and Prinn, R. G. (2010). Potential Climatic Impacts and Reliability of Very Large-Scale Wind Farms. *Atmospheric Chemistry and Physics*, 10(4), 2053–2061.

Wata, J., Faizal, M., Talu, B., Vanawalu, L., Sotia, P., and Ahmed, M.R. (2011). Studies on a Low Reynolds Number Airfoil for Small Wind Turbine Applications. *Science China Technoly Science*, 54, 1684-1688.

Wei, N. J., El Makdah, A., Hu, J., Kaiser, F., Rival, D. E., & Dabiri, J. O. (2024). Wake Dynamics of Wind Turbines in Unsteady Streamwise Flow Conditions. *Journal of Fluid Mechanics*, 1000, A66.

Werle, M. J. (2010). Wind Turbine Wall-Blockage Performance Corrections. *Journal of Propulsion and Power*, 26(6), 1317–1321.

Wiklak, P., Kulak, M., Lipian, M., and Obidowski, D. (2022). Experimental Investigation of the Cooperation of Wind Turbines. *Energies*, 15(11), 3906.

Wood, D. (2011). Small Wind Turbines: Analysis, Design, and Application. (1st ed.). Springer London.

Wu, B., Song, M., Chen, K., He, Z., and Zhang, X. (2014). Wind Power Prediction System for Wind Farm Based on Auto Regressive Statistical Model and Physical Model. *Journal of Renewable and Sustainable Energy*, 6(1), 013101.

Xiong, X.-L., Laima, S., and Li, H. (2022). Asymmetries and Similarities of Yawed Rotor Wakes. *Physics of Fluids*, 34, 1051101

Xisto, C. M., Páscoa, J. C., and Trancossi, M. (2016). Geometrical Parameters Influencing the Aerodynamic Efficiency of a Small-Scale Self-Pitch High-Solidity VAWT. ASME *Journal of Solar Energy Engineering*, 138(3), 031006.

Zhang, W., Markfort, C. D., and Porté-Agel, F. (2012). Near-wake flow structure downwind of a wind turbine in a turbulent boundary layer. *Experiments in Fluids*, 52(5), 1219–1235.

Zhao, Z., Su, D., Wang, T., Xu, B., Wu, H., and Zheng, Y. (2019). A Blade Pitching Approach for Vertical-axis Wind Turbines Based on the Free Vortex Method. *Journal of Renewable and Sustainable Energy*, 11, 053301.

Zhong, W., Shen, W. Z., and Wang, T. (2020). A Tip Loss Correction Model for Wind Turbine Aerodynamic Performance Prediction. *Renewable Energy*, 147(1), 223–238.

List of Publications

Journals

1. **Kumar, R.**, Saha, U. K., and Sahoo, N., (2025), Wake recovery assessment of a dual-rotor horizontal-axis wind turbine operating at low tip speed ratio condition, *ASME Journal of Solar Energy Engineering*, Communicated.

2. **Kumar, R.**, Siram, O., Saha, U. K., and Sahoo, N. (2024). Wake flow characteristics of small wind turbine models with single- and double-rotor arrangements: A wind tunnel study. *Journal of Renewable and Sustainable Energy*, 16(4), p. 043304.

3. Siram, O., **Kumar, R.**, Saha, U. K., and Sahoo, N., (2022), Wind tunnel probe into an array of small-scale horizontal-axis wind turbines operating at low tip speed ratio conditions. *ASME Journal of Energy Resources Technology*, 144(9), p. 091303.

4. Siram, O., **Kumar, R.**, Saha, U. K., and Sahoo, N., (2022), A comprehensive review on analytical formulations of wind turbine wake models and future scope in the development of wind farms of assorted configurations. *ASME Journal of Energy Resources Technology*, 144(11), p. 110801.

Conferences

5. **Kumar, R.**, Siram, O., Talukdar, P. K., Saha, U.K., and Sahoo, N., (2026), Wake flow analysis of a small wind turbine system with double-rotor arrangement, *7th National Conference on Wind Tunnel Testing*, February 18-20, BIT Mesra, Ranchi, India, Communicated.
6. **Kumar, R.**, Siram, O., Saha, U. K., and Sahoo, N., (2023), Wind tunnel assisted analysis on the effect of span-wise separation of small wind turbines: A near wake region study, Paper no. GTIndia2023-118499. *ASME 2023 Gas Turbine India Conference,* December 7–8, Bangalore, India.

7. **Kumar, R.**, Siram, O., Sahoo, N., and Saha, U. K., (2021), Characterizing the transitional behaviour of wind turbine wake from near to far wake regimes, Paper no. Power2021-65959. *ASME 2021 Power Conference,* July 20-22, (Virtual).